Synthesis and Characterization of Lanthanide-Based Nanocrystals for Novel Quantum Information and Bio-Imaging Applications

by

Adriaan Louis Frencken
M.Sc., Utrecht University - Utrecht, 2016
B.Sc., Utrecht University - Utrecht, 2014

A Dissertation Submitted in Partial Fulfillment
of the Requirements for the Degree of

DOCTOR OF PHILOSOPHY

in the Department of Chemistry

© Adriaan Louis Frencken, 2023
University of Victoria

All rights reserved. This dissertation may not be reproduced in whole or in part, by photocopy or other means, without the permission of the author.

Supervisory Committee

Synthesis and Characterization of Lanthanide-Based Nanocrystals for Novel Quantum Information and Bio-Imaging Applications

by

Adriaan Louis Frencken
M.Sc., Utrecht University - Utrecht, 2016
B.Sc., Utrecht University - Utrecht, 2014

Supervisory Committee

Dr. ir. Franciscus C. J. M. van Veggel (Department of Chemistry)
Supervisor

Dr. Arthur M. Blackburn (Department of Physics and Astronomy)
Co-Supervisor

Dr. Dennis K. Hore (Department of Chemistry)
Departmental Member

Dr. Rustom B. Bhiladvala (Department of Mechanical Engineering)
Outside Member

Abstract

Supervisory Committee

Dr. ir. Franciscus C. J. M. van Veggel (Department of Chemistry)
Supervisor

Dr. Arthur M. Blackburn (Department of Physics and Astronomy)
Co-Supervisor

Dr. Dennis K. Hore (Department of Chemistry)
Departmental Member

Dr. Rustom B. Bhiladvala (Department of Mechanical Engineering)
Outside Member

Lanthanide ions show a wide variety of optical and magnetic properties due to their unique 4f-orbital occupations, allowing them use in e.g. telecommunication, ultra-strong magnets, and lasers. Incorporation of these ions into nanoparticles (NPs, materials sized 1-100 nm) further extends the range of applications by allowing use inside living tissue for optical and magnetic bio-imaging, and inside nano-optics. In this dissertation, the internal structure of select lanthanide-doped NPs is investigated, and novel applications in quantum information and bio-imaging are proposed. In chapter 3, the internal structure of up-converting (UC) NPs is investigated using high-resolution 2-dimensional elemental maps generated by energy dispersive x-ray spectroscopy. It was shown that ions involved in the up-conversion are not homogenously distributed inside the particles. Heating the NPs to annealing temperatures (590 °C) homogenizes ion distribution, but no increase in emission intensity was seen. The reduced emission intensity is attributed to internal OH^- groups, for which evidence is shown in IR spectroscopy. Chapter 4 details trapping of UCNPs and $NaYF_4$ NP doped with a single Er^{3+} ion with gold nanoapertures, and discrete emission

levels are observed, suggesting the presence of individual Er^{3+} ions. These singly doped NPs are highly promising for use as single-photon emitters. In chapter 5, a potentially scalable and automatable method to anchor permanently singly doped NPs is presented, utilizing thiol-functionalization of the NP surface followed by capping with a photo-removable group. After trapping these NPs, removal of this group by UV light absorption results in permanent anchoring inside the gold nanoapertures, as verified with electron microscopy. Chapter 6 describes a novel bio-imaging technique that involves NPs that change their magnetic resonance imaging (MRI) contrast upon x-ray interaction with the dispersion. $CaF_2:Eu^{3+}$ and $CaF_2:Fe^{2+}/Fe^{3+}$ NPs were made. Dose experiments at low energies (40 keV) suggest that $CaF_2:Eu^{3+}$ turns on as a contrast agent (CA) by reduction of Eu^{3+} to Eu^{2+} by a photo-electron. At high energies (6 MeV), $CaF_2:Fe^{2+}/Fe^{3+}$ is suggested to increase contrast by oxidation of Fe^{2+} to Fe^{3+} by oxidative species. To quantify the simultaneous use of multiple CAs in mixtures, T_1 (spin-lattice) and T_2 (spin-spin) relaxation times are shown for mixtures of a Gd-complex and iron oxide nanoparticles in chapter 7. It is demonstrated that the contrasts of the CAs cannot be linearly added due the magnetic fields of CAs affecting each others relaxivities. It is suggested that a calibration curve needs to be used to quantify MRI CAs in a mixture.

Table of Contents

List of Tables

List of Figures

List of Abbreviations

CA(s)	contrast agent(s)
CCD	charge-coupled device
CT	computed tomography
DMSO	dimethyl sulfoxide
DSPE-mPEG	1,2-distearoyl-s*n*-glycero-3-phosphoethanolamine-*N*-[methoxy(polyethylene glycol)-2000]
DSPE-PEG-SH	1,2-distearoyl-s*n*-glycero-3-phosphoethanolamine-*N*-[(polyethylene glycol)-thiol-2000]
Dy-DTPA-azide	dysprosium dodecane tetraacetic acid azide
EDS	energy-dispersive X-ray spectroscopy
ESA	excited state absorption up-conversion
ETU	energy transfer up-conversion
FA	flip angle
FT-IR	Fourier transform-infrared
FTTD	finite difference time domain
FOV	field of view
Gd-BOPTA	gadobenic acid
Gd-DTPA	gadolinium-diethylenetriaminepentacetate
HWP	half-wave plate
ICP-MS	inductively coupled plasma mass spectroscopy

IR	infra-red
JCPDS	Joint Committee on Powder Diffraction Standards
LDOS	local density of states
LP	linear polarizer
MOSFET	metal-oxide semi-conductor field effect transistor
MRI	magnetic resonance imaging
MWCO	molecular weight cut-off
NIR	near infra-red
NP(s)	nanoparticles(s)
NMR	nuclear magnetic resonance
NV	nitrogen-vacancy
ODE	1-octadecene
PBS	phosphate buffer saline
PEG	poly(ethylene glycol)
PG	photo-removable group
QY	quantum yield
RF	radiofrequency
SEM	scanning electron microscopy
TE	time to echo
TEM	transmission electron microscopy
TDG	thiol-detection group
TLD	thermoluminescent detector
TR	time to repetition

UCNP(s)	upconverting nanoparticle(s)
UCQY	up-conversion quantum yield
UV	ultraviolet
XRD	x-ray diffraction
3D	three-dimensional

Acknowledgments

The following pages describe a body of research that was made possible by a large number of people, whose efforts I would like to acknowledge in this small section.

First and foremost, I would like to thank my supervisor and advisor, Dr. ir. Frank van Veggel. Frank made it possible for me to pursue my PhD in Victoria, and engage in a wide variety of stimulating projects. I learned a tremendous amount through our weekly discussions, and none of this work would have been possible without him.

Later during my PhD, Dr. Arthur Blackburn joined the team as my co-supervisor. His expertise regarding electron microscopy proved invaluable for the completion of my work on elemental mapping. Thanks for taking the time to help me with data analysis, and teaching me the basics of Matlab and Python.

Besides having two supervisors, I had the privilege of working with a large number of academic collaborators. On the trapping experiments, we worked together with the group of Dr. Reuven Gordon (UVic). Together with his students, we were able to demonstrate exciting work towards fabricating single-photon emitters.

I would like to thank Dr. Magdalena Bazalova-Carter (UVic) for collaborating with us on dosimetry experiments, and Devon Richtsmeier (UVic) for his readiness to help with our dose delivery experiments. I am also thankful for the opportunity to make a contribution to Dr. Chelsea Dunning's (UVic) photon counting work. Dr. Wayne Beckham

(BC Cancer) is also acknowledged for his advice on the interaction of x-rays with matter, and Drs. Jackie and Charles Johnson (UTSI) for their contributions with Mössbauer spectroscopy.

My gratitude to Dr. Boguslaw Tomanek and Dr. Barbara Blasiak (UCalgary) for their MRI expertise. Thank you for sharing your knowledge and advice through many meetings and making the MRI experiments possible. Andrzej Orlef, Agnieszka Skorupa, Maria Sokół (MSCNRIO) are thanked for performing the high x-ray energy experiments.

Furthermore, thanks to Chris Barr (UVic) for help with relaxivity measurements, and Jody Spence (UVic) for performing ICP-MS.

Besides our academic collaborators, I would like to thank my family for always supporting me here, from all the way back in the Netherlands. My thanks also to all the wonderful people I met during my time in Victoria, for making my time here unforgettable.

Chapter 1: Introduction

The lanthanides are the elements that are like lanthanum, and get their name from the Greek λανθανειν (lanthanein) which means "to lie hidden". Together with scandium, yttrium, and lanthanum, the lanthanides are commonly referred to as the rare earth elements. These monikers raise the expectation that these elements might be hard to come by or to find in our day-to-day life, but the opposite is actually true, with the lanthanides being highly abundant in the earths crust and used widely in common technologies.[1] The rare earths were originally discovered in a mineral in Ytterby in 1787, by Johan Gadolin, who found a mineral now known as Gadolinite. The element gadolinium owes its name to this discoverer, and the elements yttrium, erbium, and ytterbium owe their name to the city near which they were discovered. Some other lanthanides have notable namesakes as well, with dysprosium named after the Greek δυσπρόσιτος (dysprositos), meaning "hard to get to", holmium after Stockholm, and europium after the continent of Europe.[2]

Due to their unique optical and magnetic properties, the lanthanides have become ubiquitous in the technology we use every day. All of the stable lanthanide ions find use in technology such as smartphones, computers, televisions, lasers, and light bulbs. Extending beyond this, the lanthanides are broadly used in industrial applications as catalytic converters. The wide-scale application of the rare earth metals in new technologies has led the US Department of Energy to dub them the "technology metals".[3-4]

The lanthanides find such a wide range of applications due to their distinctive optical and magnetic properties. As f-block elements, each of the lanthanides has a unique electronic occupation of their respective f-orbitals.[2] The f-orbital configuration determines the optical and magnetic properties of the lanthanides, with some of these elements being highly paramagnetic due to a high number of unpaired electrons, notably neodymium, gadolinium, dysprosium, and holmium. These magnetic properties are highly desirable for use in ultrastrong (electro-)magnets and magnetic resonance imaging (MRI) contrast agents.[5-8] Unique optical properties in the lanthanides are derived from the many possible transitions between f-orbital occupation states. Each lanthanide can access distinct occupations of their f-orbitals resulting in a wide range of possible absorption and emission photon energies. Notable lanthanides where these optical properties are used are neodymium, europium, erbium, and ytterbium. These find use in lighting, telecommunication, and lasers.[9-11]

The range of possible applications has led to a widespread scientific interest in the lanthanides, with development and implementation of lanthanide-based materials taking place in a wide variety of scientific fields. The recent advent of nanotechnology further pushes the range of lanthanide applications, allowing lanthanide-based materials to be used at size-scales that were inaccessible before. Nanotechnology is the scientific field concerned with developing and using materials at the nanoscale, with nanomaterials generally classified as having a size of 1-100 nm. These materials often have vastly different properties than their bulk counterparts.[12-13]

There are a variety of ways in which the scaling down of a material can influence its properties. Reducing the size of a material increases the ratio of surface to volume, offering great advantage to applications were mostly the surface of a material is of importance. As a frame of reference, comparing a spherical material with a micrometer diameter to one with a nanometer diameter, the surface-to-volume ratio scales up a thousand times. This phenomenon is heavily exploited in heterogeneous catalysis, where catalysis takes place on the surface of a solid material. When the catalyst material is scaled down, the number of catalysis sites greatly increases as a result of the relative increase of surface area, enhancing the efficiency of the catalyst.[14]

Another way in which a nanoscale material can have different properties from its bulk counterpart is by changing the energy of the electronic states in the material. Delocalization of an exciton (an electron together with a positively charged electron hole) in a smaller volume leads to an increase in the energy of its excited states. This effect is known as quantum confinement and forms the basis of the quantum dots, semiconductor nanomaterials that due to their small size increase the energy of their excited states. The result of this is that the color of absorbed and emitted light can be tuned from low to high energies by reducing the size of the material. Applications for quantum dots include telecommunication, lighting and displays, as well as photovoltaic cells.[15-18]

A final way in which nanomaterials can find advantage over bulk materials is the small size itself, allowing the materials to be used in places where a larger material simply cannot fit. An important example is the use of nanomaterials in medical imaging. A material with

interesting optical or magnetic properties for medical imaging can be decreased in size so that it could fit inside living tissue. Such materials include luminescent biological labels, where a luminescent nanomaterial is used in conjunction with antibodies to label tissue of interest, a notable example being tumors.[19-21]

Bio-imaging refers to the visualization of living tissue. Modern medicine relies in a large part on our ability to look inside the body, and a variety of techniques have been developed to help us do so. These techniques often utilize a chemical species that enhances contrast at a tissue of interest, allowing us to view it. Two ways that are described in this work are paramagnetic contrast agents for magnetic resonance imaging (MRI) and up-converting nanoparticles (UCNPs) for luminescent imaging. MRI derives its contrast from the relaxation time of nuclear spins (often water protons) in an external magnetic field after radiofrequency excitation. The presence of a magnetic species enhances the relaxation rate of nearby nuclei, thus increasing the contrast in MRI images locally.[6-8] Contrast agents based on gadolinium- and dysprosium-rich nanoparticles have been demonstrated to have an especially large effect on the local contrast.[22-23]

Up-converting nanoparticles are promising for bio-imaging using their luminescent properties. UCNPs can absorb light in the near infra-red (NIR) and emit light in the visible region.[24-26] This has a massive advantage in luminescent bio-imaging as the emitters can be pumped at wavelengths that aren’t absorbed by the body. High intensity NIR pump power can now be used to excite the UCNPs resulting in emission that can be seen by eye.

In this dissertation, a project is described that expands on the established contrast agents for bio-imaging by developing a contrast agent that is sensitive to radiation dose. The field of therapeutic radiation to treat tumors relies heavily on accurate prediction of the delivered dose, where a dose that is too low may not treat the tumor adequately, and a dose that is too high may have damaging effects on the patient. Here, the strategy is to measure this radiation *in vivo* using an MRI contrast agent that turns on upon radiation interaction with the NP dispersion.

Besides bio-imaging, utilizing lanthanide-based materials on the nanoscale opens up the availability of nano-photonic structures to enhance their optical properties. Gold-based nanostructures have been shown to be able to enhance the electric field locally. Interaction with the gold surface plasmon can lead to greatly enhanced radiative rates in emitting species. In this dissertation this effect is utilized to demonstrate the presence of a single emitting ion in very dilutely doped nanoparticles. This results in a material that is highly promising for development of single photon emitters, which can be used for quantum information processing.

For each of the aforementioned applications of lanthanide-based nanomaterials, an intimate understanding of their internal structure is of high importance. While great progress has been made in the characterization of nanoparticles in recent years, some questions remain unanswered. Luckily, recent advancements in high-resolution electron microscopy allow us to look inside these materials. In this thesis, advanced electron microscopy techniques are used to probe the internal structure of lanthanide-based

nanoparticles, in order to better understand their properties and strategize for improved material development in the future.

This dissertation is constructed as follows: first, a discussion of the scientific background to the projects is given in chapter 2. Chapter 3 describes the mapping of the elements inside up-converting nanoparticles and the effect of heating on their distribution. In chapter 4, a method to isolate nanoparticles doped with a single ion is demonstrated. Following up on this, chapter 5 details a strategy to immobilize single nanoparticles with the goal of isolating nanoparticles with a single ion, in order to upscale a method to access single photons on demand. In chapter 6, a new method to measure radiation dose inside living tissue is presented. In chapter 7, a method is presented to combine two types of MRI, based on individually longitudinal and transverse relaxation of water protons, into a singular technique. Finally, chapter 8 summarizes the experimental chapters and offers an outlook for future experiments.

References

1. Cox, P. A., *The Elements. Their Origin, Abundance, and Distribution*. 1989.
2. Holden, N. E. *History of the Origin of the Chemical Elements and Their Discoverers*; Brookhaven National Lab.(BNL), Upton, NY (United States): 2019.
3. Rohrig, B., Smartphones: Smart Chemistry. *ChemMatters* **2015**.
4. Aspinall, H. C., *Chemistry of the F-Block Elements*. Taylor & Francis: 2001.
5. Cullity, B. D.; Graham, C. D., *Introduction to Magnetic Materials*. John Wiley & Sons: 2011.
6. Wahsner, J.; Gale, E. M.; Rodríguez-Rodríguez, A.; Caravan, P., Chemistry of MRI Contrast Agents: Current Challenges and New Frontiers. *Chem. Rev.* **2018,** *119*, 957-1057.
7. Xiao, Y.-D.; Paudel, R.; Liu, J.; Ma, C.; Zhang, Z.-S.; Zhou, S.-K., MRI Contrast Agents: Classification and Application. *Int. J. Mol. Med.* **2016,** *38*, 1319-1326.
8. Hyon, B.; Na, B.; Song, I. C.; Hyeon, T., Inorganic Nanoparticles for MRI Contrast Agents. *Adv. Mater.* **2009,** *744*, 2133-2148.
9. Werts, M. H., Making Sense of Lanthanide Luminescence. *Sci. Prog.* **2005,** *88*, 101-131.
10. Polman, A.; van Veggel, F. C. J. M., Broadband Sensitizers for Erbium-Doped Planar Optical Amplifiers: Review. *J. Opt. Soc. Am. B* **2004,** *21*, 871-892.
11. Giles, C. R.; Desurvire, E., Propagation of Signal and Noise in Concatenated Erbium-Doped Fiber Optical Amplifiers. *J. Lightwave Technol.* **1991,** *9*, 147-154.
12. Buzea, C.; Pacheco, I. I.; Robbie, K., Nanomaterials and Nanoparticles: Sources and Toxicity. *Biointerphases* **2007,** *2*, MR17-MR71.

13. de Mello Donegá, C., *Nanoparticles: Workhorses of Nanoscience*. Springer: 2014.

14. Voiry, D.; Shin, H. S.; Loh, K. P.; Chhowalla, M., Low-Dimensional Catalysts for Hydrogen Evolution and Co_2 Reduction. *Nat. Rev. Chem.* **2018,** *2*, 1-17.

15. Arakawa, Y.; Holmes, M. J., Progress in Quantum-Dot Single Photon Sources for Quantum Information Technologies: A Broad Spectrum Overview. *Appl. Phys. Rev.* **2020,** *7*, 021309.

16. De Greve, K.; Yu, L.; McMahon, P. L.; Pelc, J. S.; Natarajan, C. M.; Kim, N. Y.; Abe, E.; Maier, S.; Schneider, C.; Kamp, M., Quantum-Dot Spin–Photon Entanglement Via Frequency Downconversion to Telecom Wavelength. *Nature* **2012,** *491*, 421-425.

17. Bera, D.; Qian, L.; Tseng, T.-K.; Holloway, P. H., Quantum Dots and Their Multimodal Applications: A Review. *Materials* **2010,** *3*, 2260-2345.

18. Nozik, A. J., Quantum Dot Solar Cells. *Phys. E: Low-Dimens. Syst. Nanostructures* **2002,** *14*, 115-120.

19. Wang, X.; Chang, H.; Xie, J.; Zhao, B.; Liu, B.; Xu, S.; Pei, W.; Ren, N.; Huang, L.; Huang, W., Recent Developments in Lanthanide-Based Luminescent Probes. *Coord. Chem. Rev.* **2014,** *273*, 201-212.

20. Bünzli, J.-C. G.; Eliseeva, S. V., Lanthanide NIR Luminescence for Telecommunications, Bioanalyses and Solar Energy Conversion. *J. Rare Earths* **2010,** *28*, 824-842.

21. Yang, D.; Hou, Z.; Cheng, Z.; Li, C.; Lin, J., Current Advances in Lanthanide Ion Ln^{3+}-Based Upconversion Nanomaterials for Drug Delivery. *Chem. Soc. Rev.* **2015,** *44*, 1416-1448.

22. Das, G. K.; Johnson, N. J.; Cramen, J.; Blasiak, B.; Latta, P.; Tomanek, B.; van Veggel, F. C. J. M., $NaDyF_4$ Nanoparticles as T_2 Contrast Agents for Ultrahigh Field Magnetic Resonance Imaging. *J. Phys. Chem. Lett.* **2012,** *3*, 524-529.

23. Johnson, N. J.; Oakden, W.; Stanisz, G. J.; Scott Prosser, R.; van Veggel, F. C. J. M., Size-Tunable, Ultrasmall $NaGdF_4$ Nanoparticles: Insights into Their T_1 MRI Contrast Enhancement. *Chem. Mater.* **2011,** *23*, 3714-3722.

24. Wen, S.; Zhou, J.; Zheng, K.; Bednarkiewicz, A.; Liu, X.; Jin, D., Advances in Highly Doped Upconversion Nanoparticles. *Nat. Commun.* **2018,** *9*, 1-12.

25. Haase, M.; Schäfer, H., Upconverting Nanoparticles. *Angew. Chem. Int. Ed.* **2011,** *50*, 5808-5829.

26. Liu, Q.; Sun, Y.; Yang, T.; Feng, W.; Li, C.; Li, F., Sub-10 nm Hexagonal Lanthanide-Doped $NaLuF_4$ Upconversion Nanocrystals for Sensitive Bioimaging in Vivo. *J. Am. Chem. Soc.* **2011,** *133*, 17122-17125.

Chapter 2: Theory and Background

In this chapter, the scientific background of a variety of concepts fundamental to this dissertation will be explained. In the first section, select interesting properties of lanthanide ions will be discussed. Building on that, the concept of up-conversion of light using lanthanide ions will be covered. The working of the diagnostic tool magnetic resonance imaging will be explained, as well as the use of magnetic contrast agents. Finally, the analytical techniques electron microscopy and energy dispersive x-ray spectroscopy are presented.

2.1 Lanthanide ions

Lanthanide ions find widespread application due to their diverse electronic properties.[1] As the first row of the elements in the f-block in the periodic table, each subsequent lanthanide ion has an extra electron in the 4f orbital, ranging from Cerium, with the electronic configuration of [Xe] $4f^1$ $5d^1$ $6s^2$ to lutetium, with the electronic configuration of [Xe] $4f^{14}$ $5d^1$ $6s^2$. By far the most common oxidation state for the lanthanide ions is 3+. These trivalent lanthanide ions have the electronic configuration [Xe] $4f^n$ with n = 1, 2, …, 14. Due to their unique electronic occupation of the f-orbitals, each lanthanide ion has its own unique magnetic and optical properties.

2.2 Optical properties

The optical properties of the lanthanide ions are largely determined by the intra-orbital f-f transitions.[2] These transitions are parity forbidden according to the Laporte selection rule, which results in long excited state relaxation times (on the microsecond to millisecond

scale). The fact that each lanthanide with exception of lutetium has only partially filled 4f orbitals means that a multitude of 4f orbital electron occupations is possible. This results in a variety of energy levels that are accessible from the energetic ground states of these lanthanides. The excited states are mapped out in Figure 2.1 in a Jablonski diagram that was published by Dieke and Crosswhite. Here, the f-orbital occupations are denoted with term symbols, and are shown at their energy levels relative to the ground state occupation. The black dots at the bottom of select energy levels denote that emission has been measured from this state.[3]

The term symbols are descriptors of the angular momentum quantum numbers of the ions. They take the form of $^{2S+1}L_J$, where S is the spin quantum number, L is the orbital quantum number, and J is the total angular momentum quantum number. L is denoted with a letter corresponding to the orbital quantum number, using the notation S, P, D, F, G, … = 0, 1, 2, 3, 4, … etc. The ground state term symbol is determined using Hund's rules.

As we can see, the accessible energy levels can be quite simple: for Ce^{3+} and Yb^{3+} there is only a single excited state, corresponding to a change in the J-value. As a result, their absorption and emission spectra are very simple as well. For others, like Eu^{3+} and Er^{3+} the amount of accessible excited states is high, leading to a multitude of peaks in their emission spectra that are unique for each of these lanthanides.

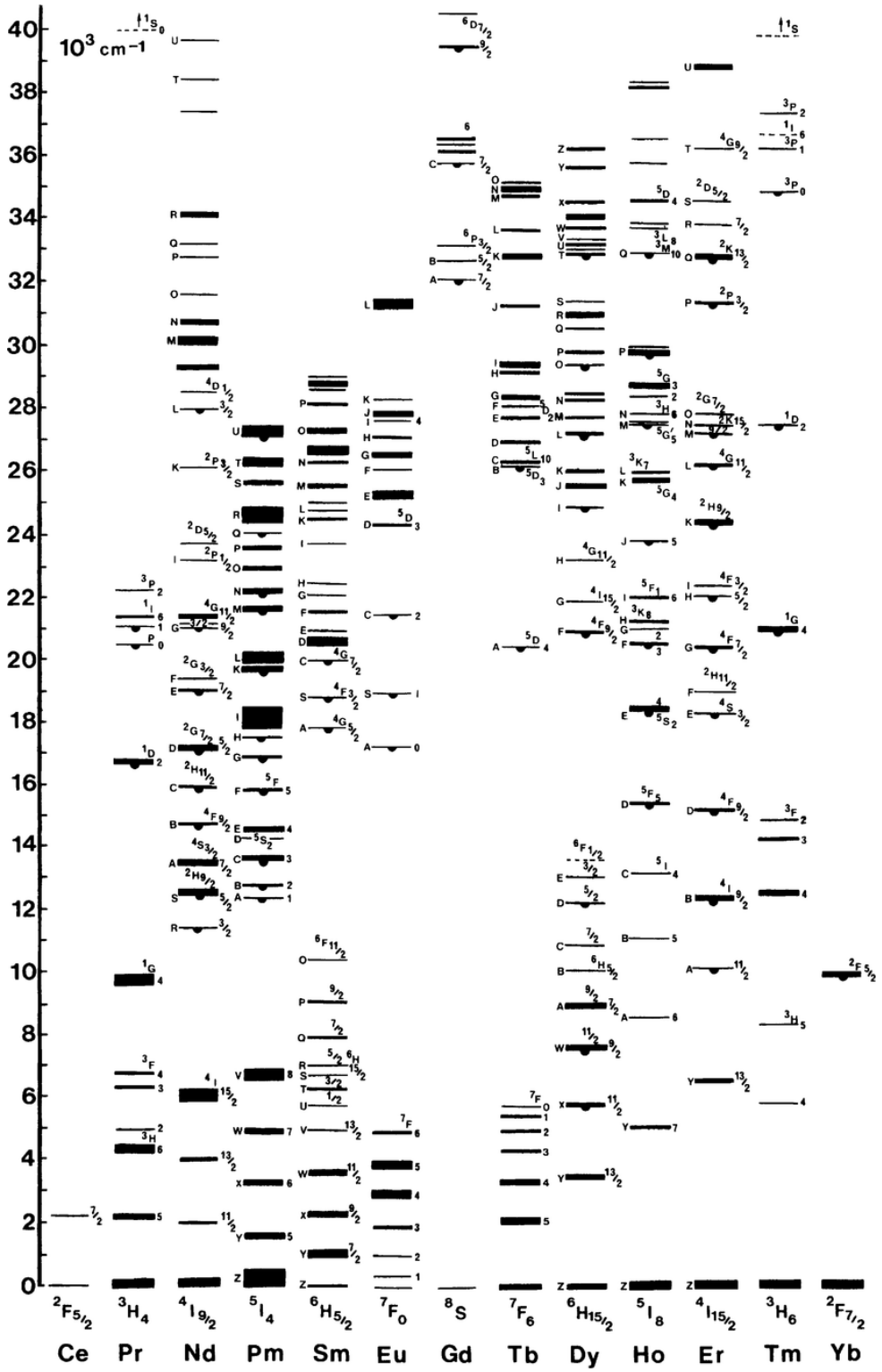

Figure 2.1: Energy levels of the trivalent lanthanide ions as depicted by Dieke et al. The black dots indicate light was measured from this state. Image adapted from reference.[3]

2.3 Magnetic properties

Besides the optical properties, the magnetic properties of the different lanthanide ions vary with the 4f occupation as well. The observed magnetic moments of the different trivalent lanthanide ions are shown in Table 2.1, alongside their 4f configuration, electronic ground state, number of unpaired electrons, and the calculated magnetic moment using the Landé formula, see equation (1). In this equation, the magnetic moment is calculated from the total angular momentum quantum number J (= S + L), and the Landé g-factor g_J, given by equation (2), where S is the spin quantum number and L is the orbital quantum number. It can be observed that the total angular momentum quantum number J has a large influence on the observed magnetic moment. This has the effect that Dy^{3+} and Ho^{3+} in their ground state have the highest magnetic moments, even though the number of unpaired electrons is lower than in Gd^{3+} and Tb^{3+}.[4]

As seen in Table 2.1, calculated magnetic moments of trivalent lanthanide ions correspond well with the observed values. A notable exception is Eu^{3+}. The discrepancy in Eu^{3+} is explained by occupation of its low-lying excited states by thermal excitation. The result of this is that while Eu^{3+} is calculated to not have a magnetic moment, due to the ground state J being 0. However, at room temperature, energy levels with J > 0 are occupied and thus a small magnetic moment is observed.

$$\frac{\mu_{eff}}{\mu_B} = g_J\sqrt{J(J+1)} \tag{1}$$

$$g_J = \frac{3}{2} + \frac{S(S+1)-L(L+1)}{2J(J+1)} \tag{2}$$

Table 2.1: Lanthanide ions and their magnetic moments.

Ln	**config. Ln^{3+}**	**Ground State**	**No. of unpaired e^-**	$g_J\sqrt{J(J+1)}$	**Observed μ_{eff}/μ_B**
La	$4f^0$	$^1S_0$	0	0	0
Ce	$4f^1$	$^2F_{5/2}$	1	2.54	2.3 - 2.5
Pr	$4f^2$	$^3H_4$	2	3.58	3.4 - 3.6
Nd	$4f^3$	$^4I_{9/2}$	3	3.62	3.5 - 3.6
Pm	$4f^4$	$^5I_4$	4	2.68	-
Sm	$4f^5$	$^6H_{5/2}$	5	0.85	1.4 - 1.7
Eu	$4f^6$	$^7F_0$	6	0	3.3 - 3.5
Gd	$4f^7$	$^8S_{7/2}$	7	7.94	7.9 - 8.0
Tb	$4f^8$	$^7F_6$	6	9.72	9.5 - 9.8
Dy	$4f^9$	$^6H_{15/2}$	5	10.65	10.4 - 10.6
Ho	$4f^{10}$	$^5I_8$	4	10.6	10.4 - 10.7
Er	$4f^{11}$	$^4I_{15/2}$	3	9.58	9.4 - 9.6
Tm	$4f^{12}$	$^3H_6$	2	7.56	7.1 - 7.6
Yb	$4f^{13}$	$^2F_{7/2}$	1	4.54	4.3 - 4.9
Lu	$4f^{14}$	$^1S_0$	0	0	0

2.4 4f Shielding

The 4f orbitals of the lanthanide ions are well shielded from their environment, as a result of the occupied 5s and 5p orbitals extending further beyond the nucleus and the 4f orbitals hardly being involved in the chemical bonding. This leads to the interesting effect that the lanthanide ions can be incorporated in a variety of different host materials, occupying e.g., a lattice site in an ionogenic crystal, with minimal effect on the lanthanides optical and magnetic properties. This is in contrast to, for example, the d-orbitals in the transition metals. Here, the absorption and emission energies are heavily dependent on the coordinating environment, leading to splitting of the orbitals in different energy levels.

Furthermore, the number of unpaired electrons of d-block elements can be influenced by crystal field splitting as well, resulting in an effect on the magnetic properties.[5]

2.5 Photon up-conversion

Photon up-conversion refers to the conversion of low-energy light to high-energy light via the sequential absorption of one or more photons. This results in strong shift in the emitted light towards higher wavelengths. Other methods to achieve high-energy emission upon low-energy excitation, like multi-photon absorption and anti-Stokes shifted emission. The ability to modulate light this way using doped materials has been investigated since 1959, when Nicolaas Bloembergen proposed the use of rare earth ions to count photons in the infrared.[6] Since then, up-converting materials have seen research for wide range of materials, and a variety of up-conversion schemes have been proposed.[7]

Up-conversion manifests itself as a multistep process. A distinction is made between excited state absorption up-conversion (ESA) and energy transfer up-conversion (ETU). In ESA, an electron is excited by an absorbed photon, followed by another excitation by photon-absorption, after which decay to the ground state results in light emitted of a higher energy then the light that was absorbed. ETU involves absorption of light, resulting in excited state electrons, followed by energy transfer to an excited state electron, leading to excitation to higher energies. Finally, this high-energy electron can relax to its ground state upon emission of a photon with higher energy than the absorbed light. The process is schematically depicted in Figure 2.2.

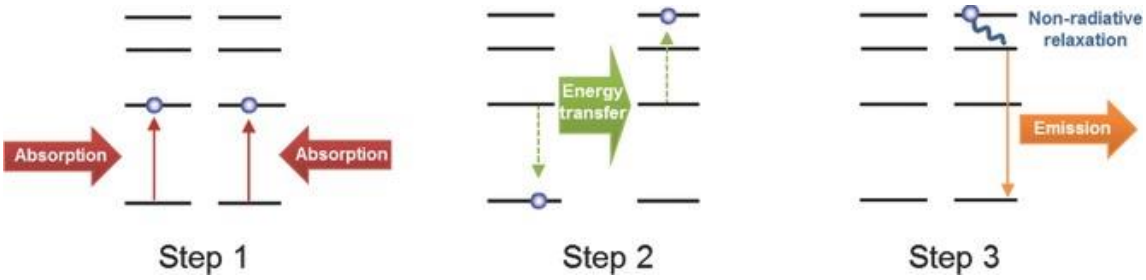

Figure 2.2: Schematic depiction of energy transfer up-conversion in three steps: absorption, energy transfer, and emission. Image reproduced from reference.[8] Red arrows indicate resonant absorption, green arrows the energy transfer, and the orange arrow the radiative decay.

A material that has received particular attention is $NaYF_4$ doped with the Yb^{3+} and Er^{3+} lanthanide ions. In this up-conversion scheme, Yb^{3+} acts as a sensitizer, allowing absorption of 980 nm light. Yb^{3+} acts as an excellent sensitizer ion due to its absorption cross-section, which is large for a parity forbidden transition. Er^{3+} can also absorb light at this wavelength at a smaller absorption cross-section, and emit light across a broad spectrum in the visible and infra-red regions. $NaYF_4$ is an excellent host material due to its low vibrational energy, minimizing the possibility of energy losses by lattice phonons.[7]

After light-absorption, Yb^{3+} ions can transfer their energy to an Er^{3+} ion, resulting in high-energy electrons, which can relax to the ground state upon emission of up-converted light. Figure 2.3 shows a proposed mechanism for the up-conversion of light by the Er^{3+}/Yb^{3+} pair. We can see that the possible transitions in Er^{3+} are quite complex, and excitation of an Er^{3+} electron can lead to a variety of different outcomes. The solid red and blue arrows indicate energy transfer between excited state electrons. Emission of light is shown by the dashed arrows, with the black dashed arrows indicating infrared emission, the red arrows the red emission, and the green and blue arrows emission of their respective

colors. The dotted arrows indicate a cross-relaxation process whereby a ground-state electron is excited by relaxation of an electron to the $^4I_{13/2}$ state. Finally, the undulating arrows in the higher energy states indicate non-radiative relaxation.

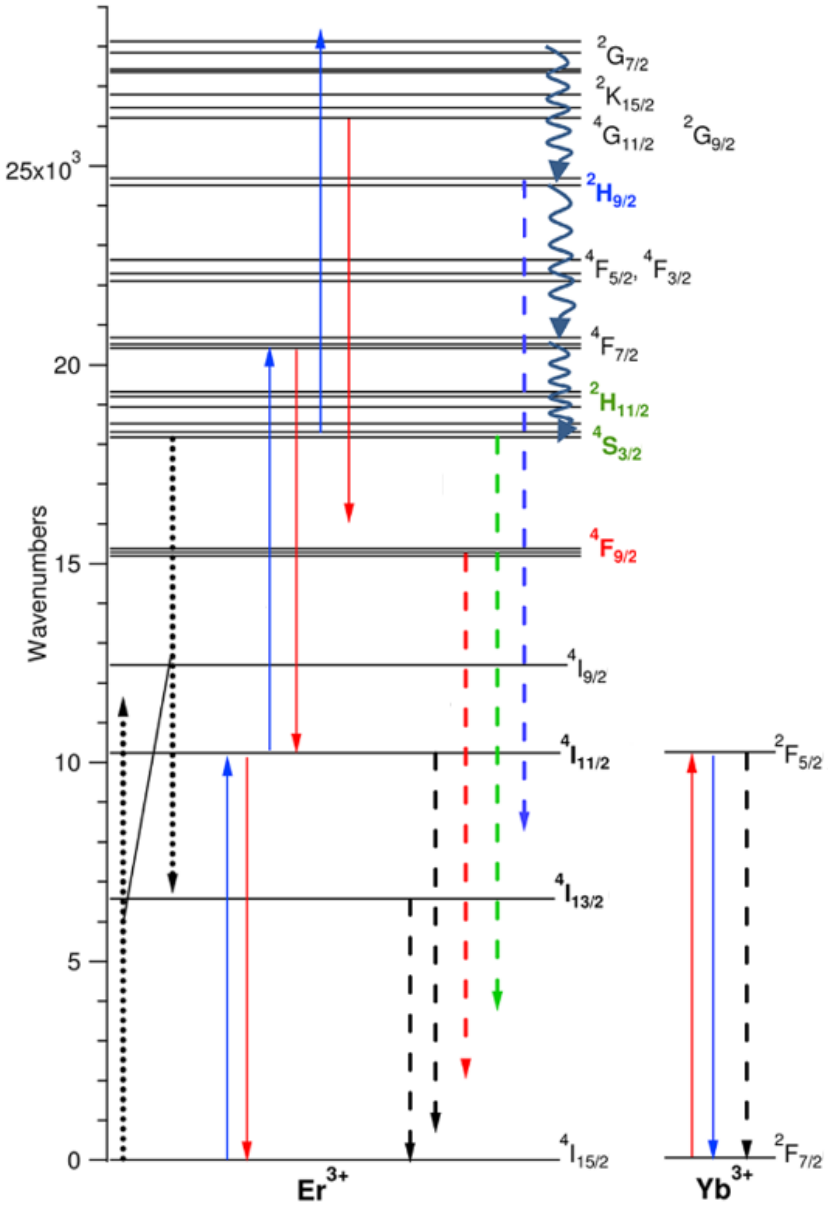

Figure 2.3: Up-conversion scheme proposed for the Yb^{3+}/Er^{3+} pair. Image reproduced from reference.[9] Here, arrow length is not shown to scale of energy in the transition for the higher energy emissions.

2.6 Single photon emitters

The ability to access a single photon on demand has been long sought after for applications in telecommunication and quantum computing. Quantum computation schemes have been proposed that use single photons to perform computational algorithms not possible using classical schemes. Furthermore, single photon information transfer can be used for a novel type of quantum cryptography, where information is protected by the unique nature of the single photons used in the communication.[10]

Crucial to the working of a single photon source for the desired applications is the anti-bunching of photons emitted by the source.[11] Anti-bunching refers to the property that photons are emitted discretely, as opposed to random photon sources. These random photon sources can be tuned to emit an average of one photon at a time, but the number of emitted photons will still follow Poisson statistics, with the result that only ~30% of the time a single photon is truly emitted. The formula for Poisson statistics is given in equation (3). Here, the function gives the probability of an event occurring a number *k* times, given an average expected number of occurrences λ.[12]

$$f(k,\lambda) = \frac{\lambda^{k} e^{-\lambda}}{k!} \tag{3}$$

An excellent system to emit a single photon at a time without bunching is a simple two energy level electronic configuration. With only a single excited state, pumping at its resonant energy will only result in a single photon emitted at a time. Achieving such a state

has been realized using color centers in crystals via vacancies or single dopant ions,[13] using single molecules,[14] or single atoms.[15]

2.7 MRI

Magnetic resonance imaging or MRI is an imaging technique based on the relaxation of proton spins in an external magnetic field. Since its inception, magnetic resonance imaging (MRI) has seen widespread use as a medical imaging technique. Advantages of MRI are a high spatial contrast and potentially limitless depth of penetration, all while being non-invasive to the body.[16]

During an MRI scan, nuclear spins align parallel or anti-parallel to the externally applied magnetic field, precessing along an axis in the direction of the field. This is shown in the schematic depiction in Figure 2.4 (a). Spins aligned anti-parallel to the field are higher in energy than those aligned parallel, where the energy difference scales with the magnetic field strength. At room temperature, a large number of spins will align anti-parallel as a result of thermal excitation.

A radiofrequency (RF) pulse is applied to the body, resulting in excitation of parallel spins to anti-parallel, leading to a decrease in magnetic moment in the direction of the applied field (directed along the z-axis). Furthermore, spins precess in phase during the RF pulse, resulting in a net magnetic moment perpendicular to the applied field (in the x, y plane). These effects are shown in the first step of Figure 2.4 (b). In the time following the RF pulse, spins will relax back to their ground state resulting in a recovery of the magnetic moment in the z direction. The spin phase will decohere as well resulting in a decrease in

the magnetic moment in the x, y plane. These steps are shown in the second and thirds step of Figure 2.4 (b).

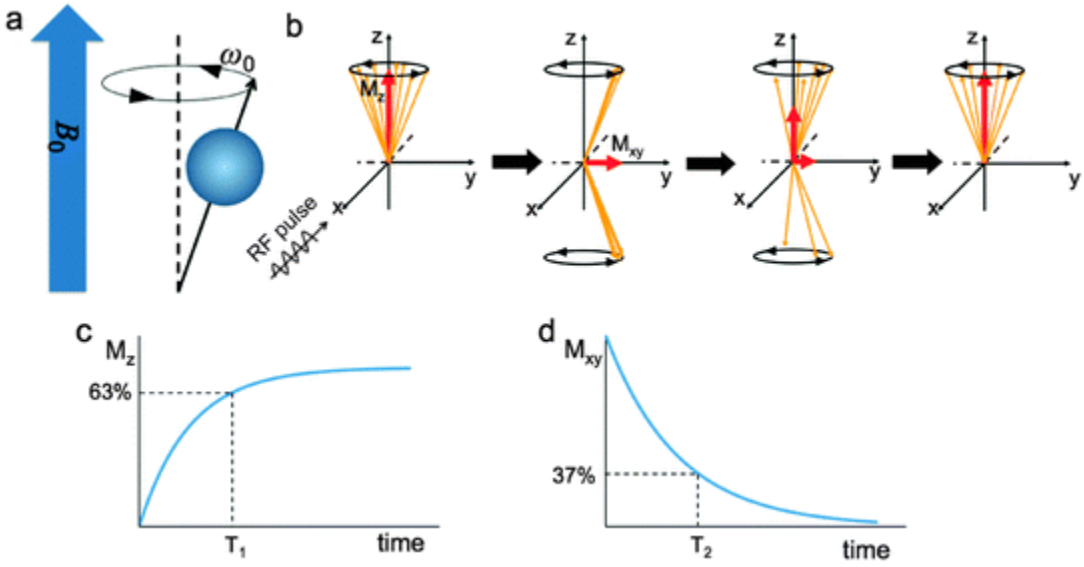

Figure 2.4: Spin effects in T_1 and T_2 MRI. Image adapted from reference.[17]

The time it takes for RF excited spins to relax back into the z-direction is referred to as T_1, and T_1 is used as the contrast in type I (T_1) MRI. The relaxation time back in the x, y plane is denoted as T_2 and is used as the contrast in type II (T_2) MRI. The magnetic field recovery over time is shown in Figure 2.4 (c) for the z-axis, and in Figure 2.4 (d) for the x, y plane. To determine the relaxation times, the change in magnetic moment in the z- and x, y directions is measured during a series of RF pulses at varying time intervals, and respective relaxation times are determined by fitting to an exponential decay function. The functions to determine T_1 and T_2 are shown in formula (4) and (5), respectively. Here M denotes the measured magnetic field, in the z direction and the x, y plane, and t denotes the time after RF pulse excitation. From these functions it can be calculated that T_1 is the point

in time where ca. 63% of the magnetic field M_z has recovered, and T_2 the time that ca. 37% of the magnetic field $M_{x,y}$ has recovered.

$$M_z(t) = M_{z,eq}(1 - e^{-\frac{t}{T_1}}) \quad (4)$$

$$M_{x,y}(t) = M_{x,y}(0)e^{-\frac{t}{T_2}} \quad (5)$$

In the external magnetic field, nuclear spins precess at the Larmor frequency, given in equation (6). Here, ω_0 is the angular frequency of the nuclear spin, B_0 the strength of the magnetic field, and γ is the gyromagnetic ratio, related to the nuclear spin mass. Tuning the instrument coils to the frequency at which the nuclei precess allows read-out of the magnetic resonance signal.

$$\omega_0 = \gamma B_0 \quad (6)$$

To encode an image of nuclear signals spatially, a magnetic field gradient is used. The magnetic gradient ensures that spins precess at different frequencies in the direction of the gradient. The frequency readout can then be used to allow spatial encoding of the signal.

Clinical MRI is primarily concerned with magnetic resonance of ^{1}H nuclear spins. While different nuclear spins might be utilized, such as ^{13}C ,^{19}F, and ^{31}P, ^{1}H has the advantage of being far more abundant in living tissue.

2.8 MRI contrast agents

A disadvantage of MRI compared to other medical imaging techniques is its low sensitivity. As an example, a typical MRI scanner operating at an applied magnetic field of 1.5 T only probes 5 out of a million molecules in the body. Increasing the sensitivity of MRI has been an outstanding challenge in the field.

A method to increase the MRI contrast *in vivo*, is the introduction of (para-)magnetic contrast agents. These are chemical agents that increase the contrast by locally affecting the T_1 and/or T_2 relaxation times. Paramagnetic contrast agents that have seen clinical use include gadolinium complexes to enhance T_1 contrast,[18-19] and iron oxide nanoparticles that enhance T_2 contrast.[20-21]

These contrast agents can be functionalized by attaching antibodies to their surface, allowing them to target specific parts of the body expressing the corresponding antigens. An example of this use is the functionalization of paramagnetic contrast agents with antibodies that target antigens expressed by tumors, in order to label these tumors and highlight them in the MRI scan.[22]

2.9 Nanomaterial synthesis and characterization

The variety of topics presented in this background chapter find applications in the field of nanomaterials, materials with dimensions sized between 1 and 100 nm. There is a variety of ways in which nanomaterials can be fabricated. The fabrication strategies can be generally classified in two approaches: the top-down approach, and the bottom-up approach.[23]

The top-down approach takes the starting point of a bulk material, and uses methods to bring the size of any number of dimensions down to the nanoscale. A simple example can be the grinding down of a bulk crystal into a small powder of nanocrystals. More sophisticated examples include lithography, where a laser beam or ion beam is used to cut away small parts of a material to generate nanoscopic features.[24] The bottom-up approach is from the opposite direction, where nano-sized materials are grown from molecular or atomic substituents. An example is the sputter deposition of a material, forming a nanometer-scale thin film.[25]

The nanomaterials presented in this dissertation are made via a bottom-up approach, growing crystals by precipitation of ionogenic crystals from solution.[23] This approach is referred to as a colloidal synthesis, a chemical synthesis resulting in a colloidal system, where one phase is finely dispersed in another. Advantages of the colloidal synthesis approach are the ease of preparation at variety of scales. Often only simple laboratory equipment is needed to make a small batch of nanocrystals (on the mmol scale), while different methods may be used to fabricate nanomaterials in large batches on an industrial scale for mass production, where aspects such as mass diffusion and heat transfer play a larger role.[26]

Colloidal synthesis of nanomaterials generally involves two steps: nucleation of the material in a supersaturated solution, resulting in small seed crystals, followed by growth, whereby material is deposited on the seeds. For seed particles to form, a minimum level of supersaturation needs to be achieved. The free energy change associated with the formation

of crystals in solution is given in equation (7). In this equation the change in free energy ΔG is calculated from the interfacial energy determined by radius r and interfacial tension γ, and the energy of a spherical crystal with radius r and crystal free energy ΔG_v. The expression for ΔG_v is given in (8), where k_B is the Boltzmann constant, T is the absolute temperature, S is the entropy, and v is the molar volume.

$$\Delta G = \pi r^2 \gamma + \frac{4}{3} \pi r^3 \Delta G_v \tag{7}$$

$$\Delta G_v = \frac{-k_B T ln(S)}{v} \tag{8}$$

The surface and volume contributions to the change in free energy as a function of the crystal radius are plotted in Figure 2.5. Addition of the two shows a rise at low radii, followed by a drop at higher radii. The point at dG/dr = 0 is known as the critical radius r_c. This is the minimal radius a nucleus needs to achieve before crystal growth is energetically favorable. The expression for the critical radius can be derived by differentiating the expression for ΔG (7) with respect to r and equating it to 0, yielding equation (9). Combining this equation with equation (8) then yields the total expression for the critical radius shown in equation (10).[27]

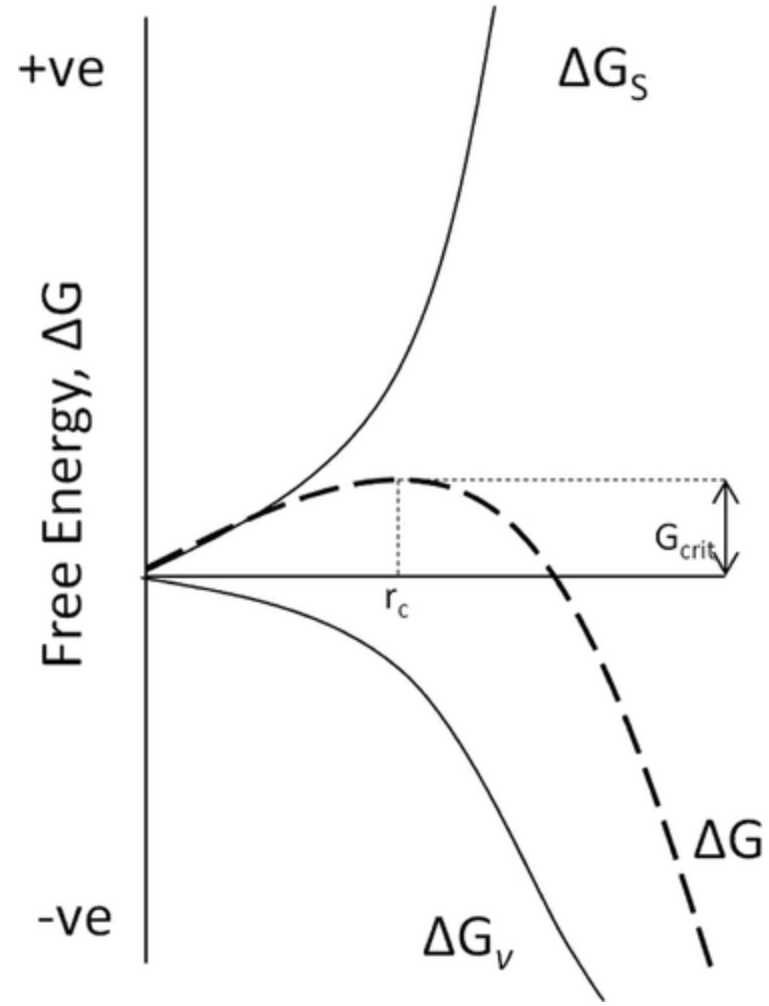

Figure 2.5: Surface and volume contributions to the change in free energy as a function of crystal radius. Image reproduced from reference.[27]

$$r_{crit} = \frac{-2\gamma}{\Delta G_v} \tag{9}$$

$$r_{crit} = \frac{-2\gamma v}{k_B T ln(S)} \tag{10}$$

Following the nucleation event, growth of the nanocrystal can proceed. Dependent on the material and the synthesis conditions, a variety of possible mechanisms can be

appropriate to describe the nanocrystal nucleation and growth. A straightforward nucleation mechanism is given by LaMer.[28] Here, the nucleation and growth steps are fully separated. It is assumed that all nuclei form simultaneously at the start of the reaction, followed by homogeneous growth as the reaction progresses. Three stages of LaMer growth are shown in Figure 2.6. Stage I is the rise of reactant concentration, II is the nucleation step achieved by reaching a critical concentration C_{crit} that triggers the burst of nucleation, III is the step where concentration is too high for nucleation. At this stage growth can occur.

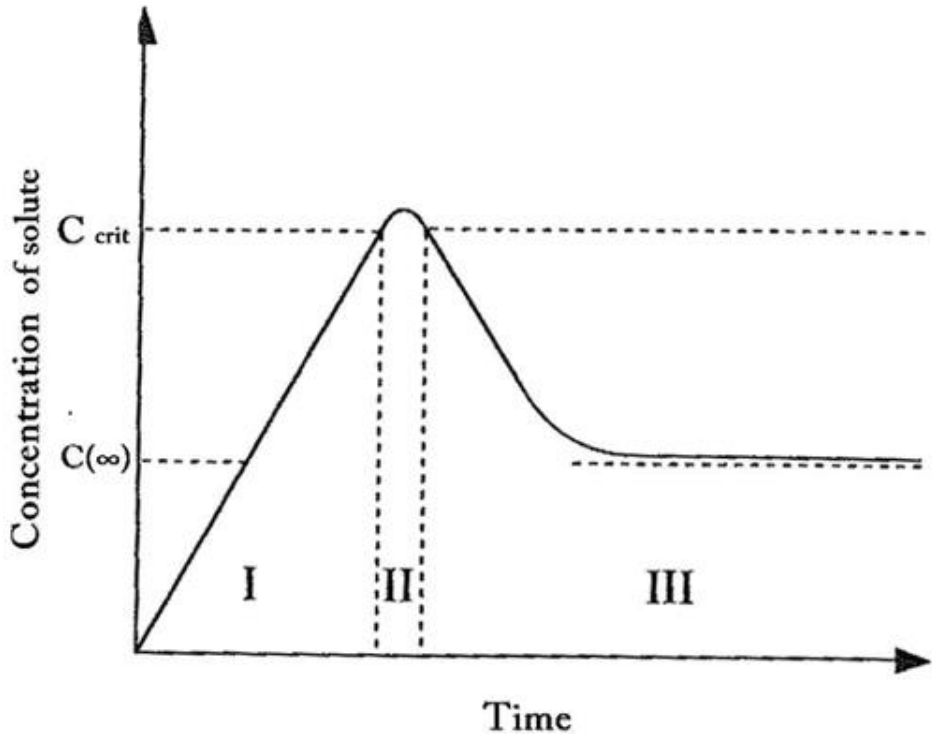

Figure 2.6: Three stages of LaMer nucleation. Reproduced from reference.[28]

The growth mechanism that has been argued to be most appropriate for the ionogenic lanthanide-based nanocrystals described in this dissertation is Ostwald ripening.[29-30] In

Ostwald ripening, material is deposited on nuclei by dissolution of other nanoparticles.[31] Specifically, smaller nanoparticles re-dissolve at higher rates than the larger ones due to their increased surface energy. The solute formed from this dissolution can then deposit on the larger nanoparticles in the solution. The result of this is that the particles grow as single domain crystals, as no coalescence of nanoparticles occurs during the ripening. The process of Ostwald ripening following nucleation is shown schematically in Figure 2.7.

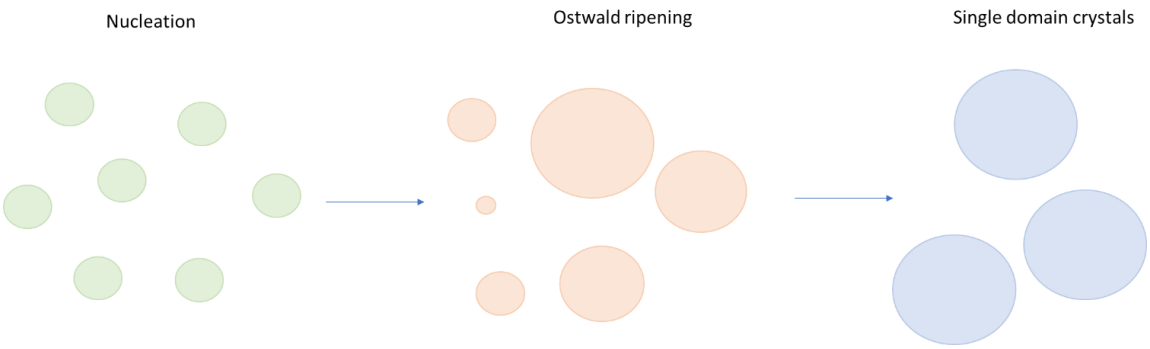

Figure 2.7: Steps in single crystal nanoparticle growth.

2.10 Electron microscopy

In the broad sense, microscopy refers to the visual analysis of anything small. Classically, visible-light microscopy has been used to study surfaces of materials and small forms of life. The limitation for how small the objects we can study is given by the Rayleigh criterion, which relates the smallest possible length scale we may resolve to the wavelength of light.[32] The smaller the wavelength of light refracted, the smaller the length scale. The theoretical highest possible resolution achievable with visible light is ca. 200 nm. If we wish to study nanomaterials, which we have previously defined as having dimensions between 1 and 100 nm, a larger resolution is required.

To achieve these high resolutions, the smaller wavelengths of high-energy electrons may be used. By tuning the wavelength of the electrons used in this probe resolutions of below a single Ångström can theoretically be achieved.[32]

Electron microscopy can be used in a variety of different modes, where both the nature of the electron beam can be varied as well as the observed effect of interaction of the beam with the species of interest. Of particular interest in this work are transmission electron microscopy (TEM), and energy dispersive x-ray spectroscopy (EDS).

In TEM, an electron beam is focussed on a sample of interest, followed by detection of electrons that are transmitted through the sample. The contrast in the image is generated by attenuation of the electron beam by the sample material, where high Z-number atoms are generally more likely to attenuate the incident electrons. The beam attenuation scales with the thickness of the sample, resulting in a higher contrast the thicker the sample is.

A schematic depiction of a TEM is shown in Figure 2.8. A core element in every electron microscope is an electron source from which the probe electron beam is emitted. Common electron sources are filaments and field emission guns. For filaments, tungsten and lanthanum borate are commonly used. The filaments are raised to a voltage to raise the temperature leading to thermionic emission of electrons. Field emission guns utilize a potential gradient resulting in field electron emission. The advantage of field emission guns over electron filaments is their high current density as well as low energy spread, resulting in a beam that can be focussed into a smaller disk.

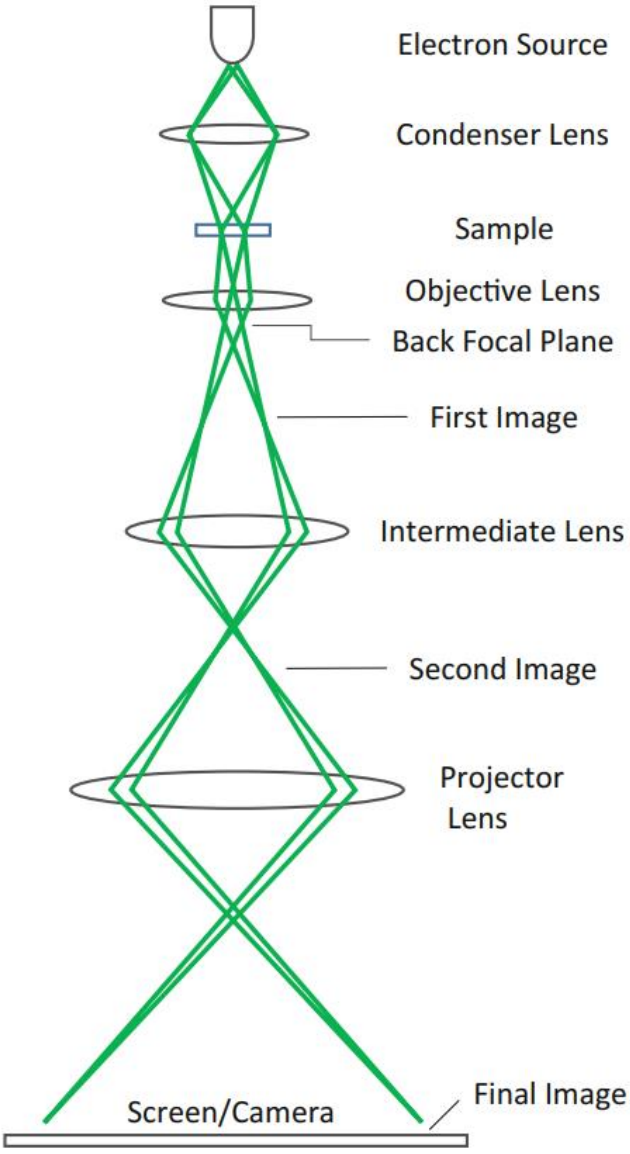

Figure 2.8: Schematic representation of a TEM, reproduced from reference.[33]

After electron emission, the beam can be focused using magnetic fields. The lenses inside an EM comprise magnetic field coils. Interaction of the electron beam with these magnetic fields causes a shift in direction. The magnetic field strength in the lenses can then be used

to focus the electron beam, where a stronger magnetic field coincides with a smaller electron scatter angle.

The electron beam is focused on the sample using a condenser lens. After passing through the sample of interest, the beam is focused using an objective lens, forming an image. The electron beam can then be focused further, and widened using the projector lens that expands the beam onto the imaging screen, which is typically a phosphor screen or charge-coupled device (CCD).

EDS is an elemental analysis technique related to electron microscopy. Similar to TEM, in EDS an electron beam is focused on a sample of interest. The incident electrons can knock out core electrons of atoms in the sample, which results in an electron hole vacancy. An electron from a higher energy orbital can fill this vacancy, and in doing so can emit an x-ray with energy equal to the difference in energy between the orbitals. The energies of the x-rays emitted are specific to the electron shells of specific elements, and measuring these x-ray spectra can be used to quantify elements in the sample.[34]

2.11 References

1. Reisfeld, R., Optical Properties of Lanthanides in Condensed Phase, Theory and Applications. *AIMS Mater. Sci.* **2015,** *2*, 37-60.
2. Bünzli, J.-C. G.; Eliseeva, S. V., Basics of Lanthanide Photophysics. *Lanthanide luminescence* **2010**, 1-45.
3. Dieke, G. H.; Crosswhite, H., The Spectra of the Doubly and Triply Ionized Rare Earths. *Applied optics* **1963,** *2*, 675-686.
4. Carlin, R. L., *Magnetochemistry*. Springer Science & Business Media: 2012.
5. Cotton, S., *Lanthanide and Actinide Chemistry* John Wiley & Sons: 2006.
6. Bloembergen, N., Solid State Infrared Quantum Counters. *Phys. Rev. Lett.* **1959,** *2*, 84.
7. Haase, M.; Schäfer, H., Upconverting Nanoparticles. *Angew. Chem. Int. Ed.* **2011,** *50*, 5808-5829.
8. Goldschmidt, J. C.; Fischer, S., Upconversion for Photovoltaics–a Review of Materials, Devices and Concepts for Performance Enhancement. *Adv. Opt. Mater.* **2015,** *3*, 510-535.
9. Anderson, R. B.; Smith, S. J.; May, P. S.; Berry, M. T., Revisiting the NIR-to-Visible Upconversion Mechanism in B-$NaYF_4$:Yb^{3+},Er^{3+}. *J. Phys. Chem. Lett.* **2014,** *5*, 36-42.
10. Eisaman, M. D.; Fan, J.; Migdall, A.; Polyakov, S. V., Invited Review Article: Single-Photon Sources and Detectors. *Rev. Sci. Instrum.* **2011,** *82*, 071101.
11. Paul, H., Photon Antibunching. *Rev. Mod. Phys.* **1982,** *54*, 1061.
12. Haight, F. A. *Handbook of the Poisson Distribution*; 1967.

13. Neumann, P.; Kolesov, R.; Jacques, V.; Beck, J.; Tisler, J.; Batalov, A.; Rogers, L.; Manson, N.; Balasubramanian, G.; Jelezko, F., Excited-State Spectroscopy of Single NV Defects in Diamond Using Optically Detected Magnetic Resonance. *New J. Phys.* **2009,** *11*, 013017.

14. Nothaft, M.; Höhla, S.; Jelezko, F.; Frühauf, N.; Pflaum, J.; Wrachtrup, J., Electrically Driven Photon Antibunching from a Single Molecule at Room Temperature. *Nat. Commun.* **2012,** *3*, 1-6.

15. Dibos, A.; Raha, M.; Phenicie, C.; Thompson, J. D., Atomic Source of Single Photons in the Telecom Band. *Phys. Rev. Lett.* **2018,** *120*, 243601.

16. Moore, E. A.; Graves, M. J.; Prince, M. R.; McRobbie, D. W., *MRI from Picture to Proton*. Cambridge University Press: 2006.

17. Hyon, B.; Na, B.; Song, I. C.; Hyeon, T., Inorganic Nanoparticles for MRI Contrast Agents. *Adv. Mater.* **2009,** *744*, 2133-2148.

18. Johnson, N. J. J.; Oakden, W.; Stanisz, G. J.; Prosser, R. S.; van Veggel, F. C. J. M., Size-Tunable, Ultrasmall $NaGdF_4$ Nanoparticles: Insights into Their T_1 MRI Contrast Enhancement. *Chem. Mater.* **2011,** *23*, 3714-3722.

19. Koenig, S. H., From the Relaxivity of Gd $(DTPA)^{2-}$ to Everything Else. *Magn. Reson. Med.* **1991,** *22*, 183-190.

20. Marriott, A.; Bowen, C.; Rioux, J.; Brewer, K., Simultaneous Quantification of SPIO and Gadolinium Contrast Agents Using MR Fingerprinting. *Magn. Reson. Imaging* **2021,** *79*, 121-129.

21. Korchinski, D. J.; Taha, M.; Yang, R.; Nathoo, N.; Dunn, J. F., Iron Oxide as an MRI Contrast Agent for Cell Tracking: Supplementary Issue. *Magn. Reson. Insights* **2015,** *8*, MRI. S23557.

22. Dash, A.; Blasiak, B.; Tomanek, B.; Latta, P.; van Veggel, F. C. J. M., Target-Specific Magnetic Resonance Imaging of Human Prostate Adenocarcinoma Using $NaDyF_4$–$NaGdF_4$ Core–Shell Nanoparticles. *ACS Appl. Mater. Interfaces* **2021,** *13*, 24345-24355.

23. de Mello Donegá, C., *Nanoparticles: Workhorses of Nanoscience*. Springer: 2014.

24. Thompson, L. F., *An Introduction to Lithography*. ACS Publications: 1983.

25. Wasa, K.; Hayakawa, S., Handbook of Sputter Deposition Technology. **1992**.

26. Bird, R. B., Transport Phenomena. *Appl. Mech. Rev.* **2002,** *55*, R1-R4.

27. Thanh, N. T.; Maclean, N.; Mahiddine, S., Mechanisms of Nucleation and Growth of Nanoparticles in Solution. *Chem. Rev.* **2014,** *114*, 7610-7630.

28. LaMer, V. K.; Dinegar, R. H., Theory, Production and Mechanism of Formation of Monodispersed Hydrosols. *J. Am. Chem. Soc.* **1950,** *72*, 4847-4854.

29. Johnson, N. J.; Korinek, A.; Dong, C.; van Veggel, F. C. J. M., Self-Focusing by Ostwald Ripening: A Strategy for Layer-by-Layer Epitaxial Growth on Upconverting Nanocrystals. *J. Am. Chem. Soc.* **2012,** *134*, 11068-11071.

30. Shan, J.; Ju, Y., Controlled Synthesis of Lanthanide-Doped $NaYF_4$ Upconversion Nanocrystals Via Ligand Induced Crystal Phase Transition and Silica Coating. *Appl. Phys. Lett.* **2007,** *91*, 123103.

31. Kabalnov, A., Ostwald Ripening and Related Phenomena. *J. Dispersion Sci. Technol.* **2001,** *22*, 1-12.

32. Williams, D. B.; Carter, C. B., The Transmission Electron Microscope. In *Transmission Electron Microscopy*, Springer: 1996; pp 3-17.

33. Zuo, J. M.; Spence, J. C., *Advanced Transmission Electron Microscopy*. Springer: 2017.

34. Goldstein, J. I.; Newbury, D. E.; Michael, J. R.; Ritchie, N. W.; Scott, J. H. J.; Joy, D. C., *Scanning Electron Microscopy and X-Ray Microanalysis*. Springer: 2017.

Chapter 3: The Internal Structure of Lanthanide-Doped Nanoparticles and the Effect of High Temperature Annealing on Their Luminescent Properties

Based on:

Frencken, A. L.; Blackburn, A. M.; van Veggel, F. C. J. M., The Internal Structure of Lanthanide-Doped Nanoparticles and the Effect of High-Temperature Annealing on Their Luminescent Properties. *J. Phys. Chem. C* 2022, *126*, 16341–16348.

Abstract

Up-converting nanoparticles are widely studied for a wide range of applications based on their unique optical properties, with $NaYF_4$ nanoparticles doped with Yb^{3+} and Er^{3+} receiving particular attention. While developing this material in nanoparticle form extends their potential applications, the resulting nanoparticles have proven less efficient up-converters than their bulk counter part. Reported up-conversion quantum yields are significantly lower, even when very thick shells were grown to eliminate quenching by surface defects and surface-bound molecules. This raises the question whether the internal structure of these particles contributes to the lower quantum yield. In this chapter, the internal structure of $NaYF_4$:Yb^{3+}, Er^{3+} NPs is investigated using high-resolution scanning energy dispersive x-ray spectroscopy, generating 2-dimensional elemental maps. It was deduced that the ions are not distributed homogenously in the nanoparticles as made via a colloidal synthesis route. Heating the nanoparticles to temperatures used to anneal bulk crystals resulted in a homogeneous distribution, but an increase in emission intensity under similar measurement conditions was not observed. Vibrational spectroscopy showed the presence of OH^- in dried nanoparticles, which might act as an internal quencher.

3.1 Introduction

Lanthanide-doped nanoparticles have captured the imagination of researchers worldwide due to their wide range of potential applications.[1-4] A lanthanide-doped nanoparticle system that has received particular attention is the up-converting nanoparticle (UCNP). UCNPs are materials that convert light from low energies to high energies. UCNPs have seen wide-spread investigation over the past decades as they have promising applications in bio-imaging,[1-2] telecommunication, temperature sensing,[5-6] and photovoltaics.[7-8] The UCNP system that has received the most scientific interest is colloidal $NaLnF_4$ co-doped with Er and Yb. In this system, up-conversion (UC) is achieved by a multistep energy transfer from optically excited Yb to Er, resulting in emission of green, red, and blue light upon near-infrared excitation.[3] While these UCNPs have been the subject of wide-spread investigation over the past decades, our understanding of their internal structure and excited state dynamics is still incomplete.[9]

For the luminescence-based UCNP applications, a high up-conversion (UC) efficiency is desired. Unfortunately, the up-conversion efficiency of UCNPs lags behind that of bulk or microcrystalline UC crystals by a large amount, with up-conversion quantum yields (UCQYs) measured a 100 to 10,000 times lower for the nano-crystalline materials under similar measurement conditions.[10-12] This discrepancy has largely been attributed to quenching of the excited state by surface defects, and significant advances in up-conversion efficiency have been made by growing a passivating shell around a UCNP core, with typical UCQYs of 0.3% and 3% when extremely thick shells were grown.[10, 13-14] Despite these advances, UCQYs are still significantly smaller than in bulk, strongly suggesting that

there are other factors that play a role in the quenching of the excited state that need further investigation.

Besides quenching by surface defects, factors that decrease UC efficiency include quenching by internal crystallographic defects, concentration quenching by cross-relaxation of the excited state and inefficient energy transfer of sensitizer ions to emitter ions possibly as a result of inhomogeneous distribution of the dopant ions. These latter effects would be the result of an inhomogeneous internal structure of the UCNPs, which could lead to deleterious optical effects.

It is hypothesized that there is a significant difference in the internal structure of UCNPs compared to the bulk, as a result of a drastic difference in the conditions used to prepare these differently sized materials. UCNPs are commonly made using colloidal synthesis techniques, growing crystals around 300 °C for 1-1.5 hours, whereas bulk UC crystals are prepared using temperatures of 600 °C and up,[15-16] with heating for several hours. The result of this difference may be an inhomogeneous dopant distribution, and the presence of internal defects in the UCNPs.

In this chapter, to investigate the dopant ion distribution in UCNPs and the influence of their preparation conditions on it, high-resolution energy dispersive x-ray spectroscopy (EDS) was employed on individual UCNPs to map out the presence of lanthanide and dopant ions in two dimensions. The effect of high temperature annealing was then investigated by mapping the ions after heating at 590 °C for two hours.

3.2 Results and discussion

UCNPs were synthesized according to previously reported procedures.[17] Briefly, lanthanide precursor salts were heated in the presence of oleic acid and 1-octadecene to form oleates. To this mixture, a solution of sodium hydroxide and ammonium fluoride dissolved in methanol was added. After evaporation of methanol, this mixture was heated to 300 ^{o}C for 90 minutes before cooling to room temperature. Particles were precipitated with absolute ethanol and collected by centrifugation and then redispersion in hexanes. Figure. 3.1 (left) shows a transmission electron microscope (TEM) image of UCNPs. The particles are seen to have a hexagonal shape. The intensity of the particle contrast varies as a result of the angling of the crystallographic planes with respect to the electron beam. The average diameter was measured to be 32.3 ± 1.4 nm, the size distribution is shown in Figure 1 (right). Figure 3.2 shows a powder XRD diffractogram, where the characteristic lines corresponding with the hexagonal β-$NaYF_4$ phase are seen overlapping with the measured peaks. The XRD pattern doesn't show evidence of other phases or impurities. These results are typical for a colloidal synthesis of $NaYF_4$ doped with 18% Yb and 2% Er.[5, 17-18]

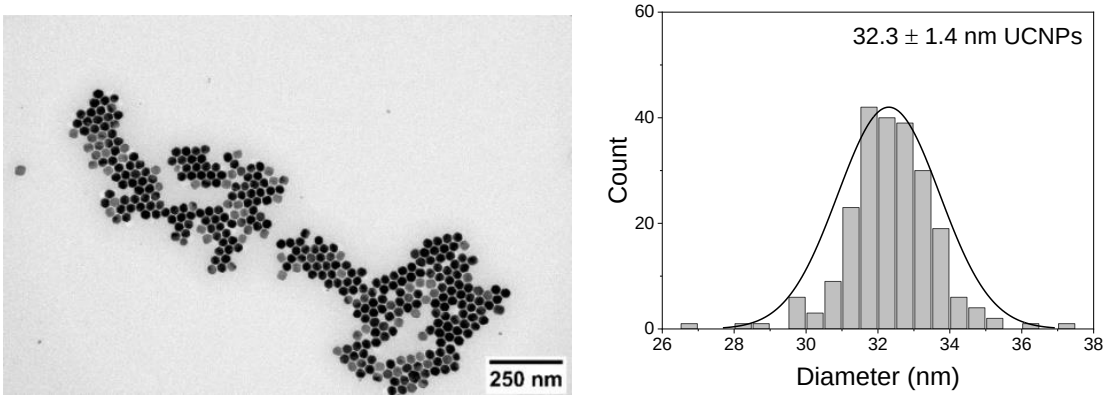

Figure 3.1: Bright field TEM (operated at 80 kV) image of UCNPs (left), and their size distribution (right).

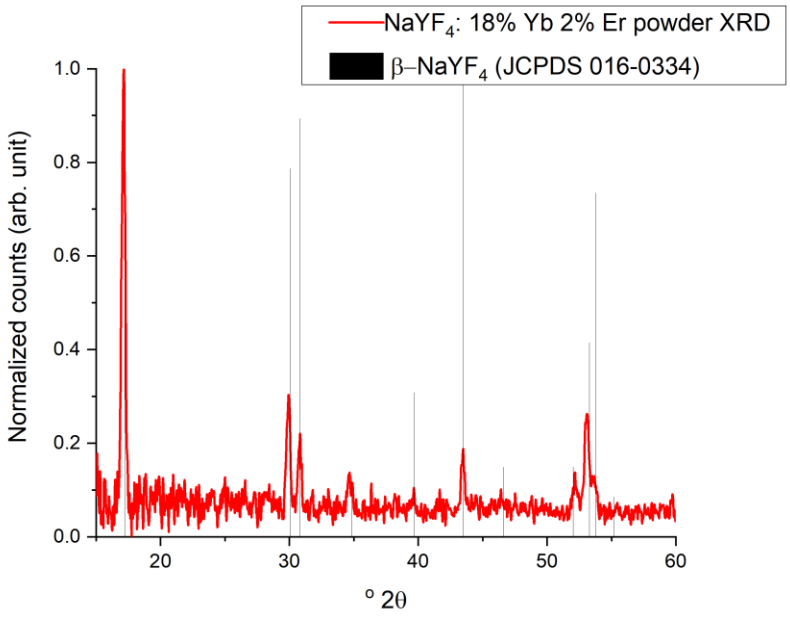

Figure 3.2: Powder XRD pattern of UCNPs with hexagonal $NaYF_4$ reference pattern.

The focus of this chapter is on mapping out the distribution of the ions in UCNPs. In this chapter, the primary tool to do this is high-resolution EDS, collecting EDS spectra in two dimensions on individual nanoparticles. A problem that was encountered while performing these measurements on carbon-coated copper EM grids was that carbon would build up in the electron beam, reducing the ability to focus on the nanoparticles. Besides this, the EM grids would give a background signal of the elements present in the grid. To minimize these effects, a holey Si EM grid was used as a substrate for the particles. Another advantage of the Si EM grid was that it was possible to clean the grids in a UV zone cleaner, removing oleates and any solvent molecules after drying. Figure 3.3 shows a TEM image of two UCNPs residing on the edge of a hole in the Si grid.

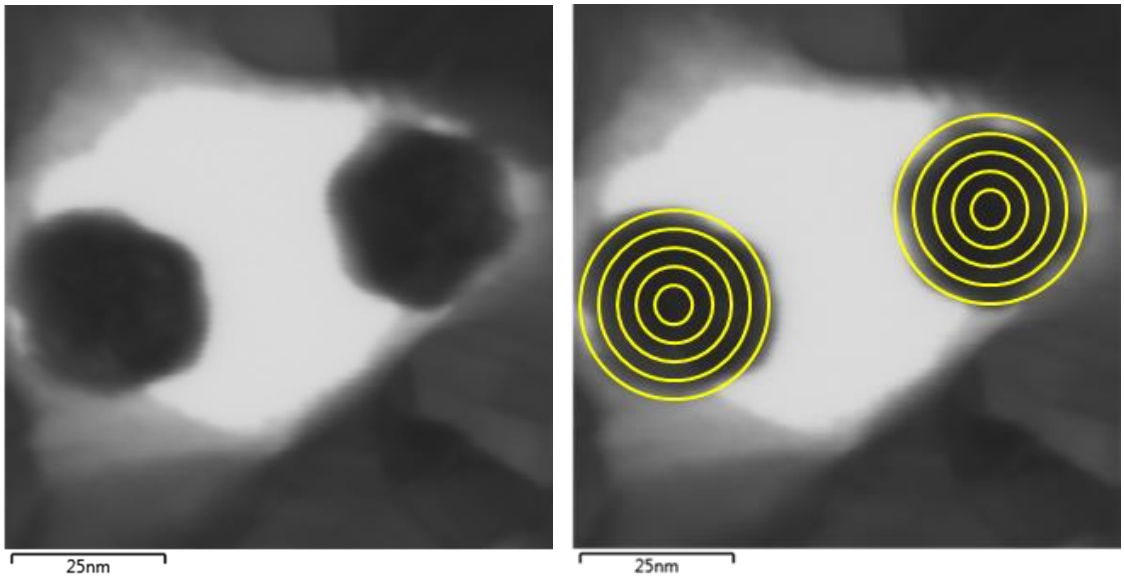

Figure 3.3: Bright field STEM (operated at 20 kV) image of UCNPs in Si hole. (left) Integrated regions used for comparison are outlined in yellow. (right)

To compare the distribution of the lanthanide ions and yttrium over the particles, peaks corresponding with the characteristic x-rays emitted by Y, Yb and Er were fitted. Figure 3.4 shows EDS maps of Y, Yb, and Er, where the number of counts corresponding with the characteristic x-rays of the elements in EDS are shown as a false-color map. In these false-color maps it can already be seen that distribution of the ions is not the same for each lanthanide. An elemental map of all three elements in a UCNP was generated by overlaying a red map of Y, a green map of Yb, and a blue map of Er, this is shown in Figure 3.5 (a) and (b). Here it is seen that the red-labeled Y is more localized on the edges, while the green-labeled Yb and blue-labeled Er can be seen in higher concentration towards the NP center.

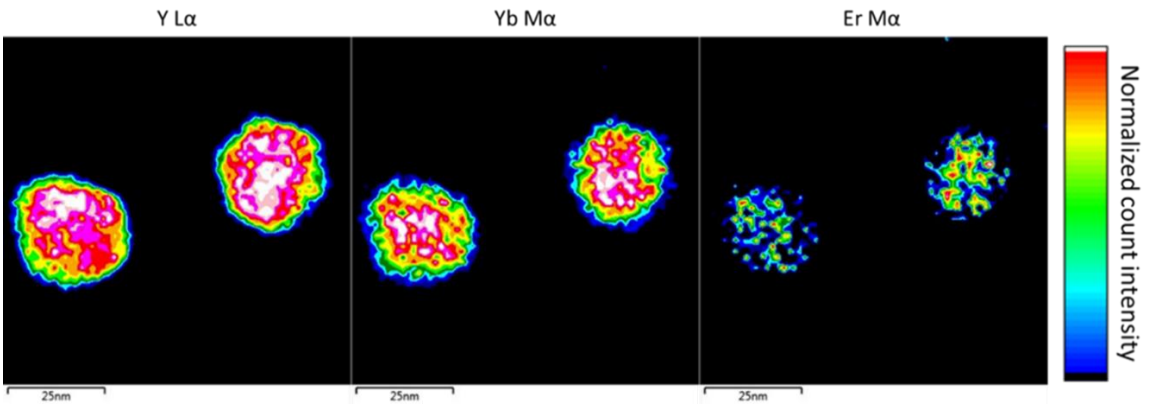

Figure 3.4: EDS maps of UCNPs. Spatial distribution of Y $L\alpha_1$ (left), Yb Mα (middle) and Er Mα (right) are shown, where the color indicates the number of counts normalized to the highest peak in the image as indicated in the color bar to the right.

The elemental distribution of the lanthanide ions in the particles was shown quantitatively by choosing and comparing different areas in the particle, and integrating the EDS peaks for each lanthanide in that area. Figure 3.3 (right) shows schematically which areas were chosen and compared: the method involved drawing a series of non-cumulative rings around the nanoparticle, emanating outward from a circle in the NP center. The second method involved drawing rings in a line from one side of the particle to the opposite side, this yielded similar results and is shown in Appendix I. The integrated peaks in each area were then plotted and graphically compared.

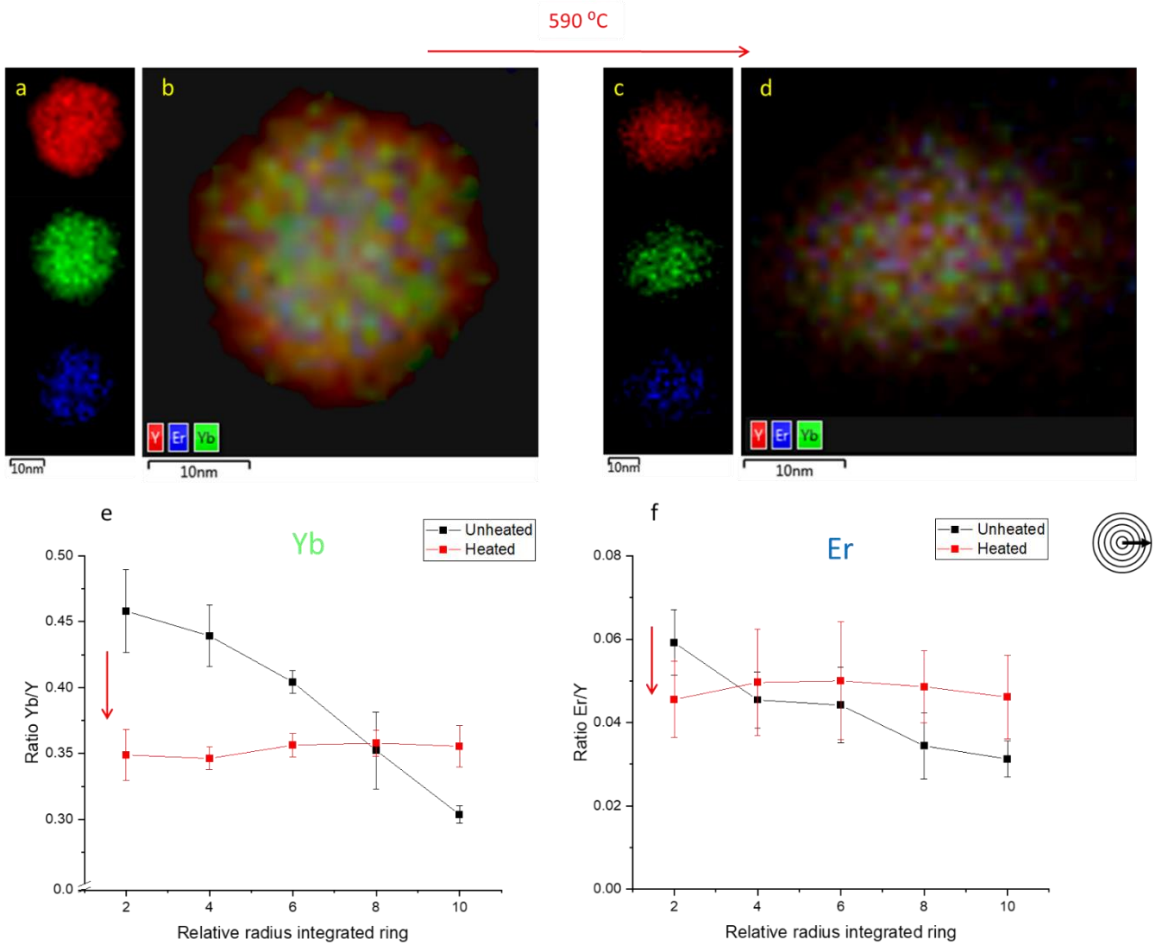

Figure 3.5: Color coded elemental maps of Y, Er, and Yb (a) in a UCNP before heating, overlaid in one image (b). (c) and (d) show the modalities after heating at 590 °C. (e) and (f) respectively show the ratio of Yb/Y and Er/Y in non-cumulative rings emanating from UCNP center, averaged over 5 nanoparticles before heating at 590 °C (black) and averaged over 6 nanoparticles after heating at 590 °C (red).

Relative abundance of Y, Yb and Er in the particles was visualized by plotting the ratio between the characteristic x-ray emission intensities. The advantage of comparing the change in ratio with respect to yttrium is that there is no need to quantify exactly the presence of the dopants to demonstrate their relative distribution. Figure 3.5 (e) and (f)

show the average ratio Yb/Y and the ratio Er/Y plotted for a series of integrated rings emanating outward from the center of the respective nanoparticles in black. The general trend that is observed is that Yb and Er are concentrated in a higher amount in the nanoparticle center with respect to Y, and a clear gradient from the center to the edge is seen.

Er and Yb both appear to be more highly localized in the nanoparticle core with respect to the Y ions. The result of this localization on the emission efficiency could be deleterious as the likelihood of concentration quenching increases when the emitter concentration exceeds the optimized percentage.

To verify the effect of high temperature annealing on the dopant distribution, the particles analyzed with EDS were annealed on the holey Si grid at 590 °C for two hours. EDS analysis was performed in the same manner as the un-annealed sample, with the comparison shown in Figure 3.5. Particles are still seen to be distinct after heating from scanning electron images, see Figure 3.6. Furthermore, the particles are of similar size, showing no loss of material.

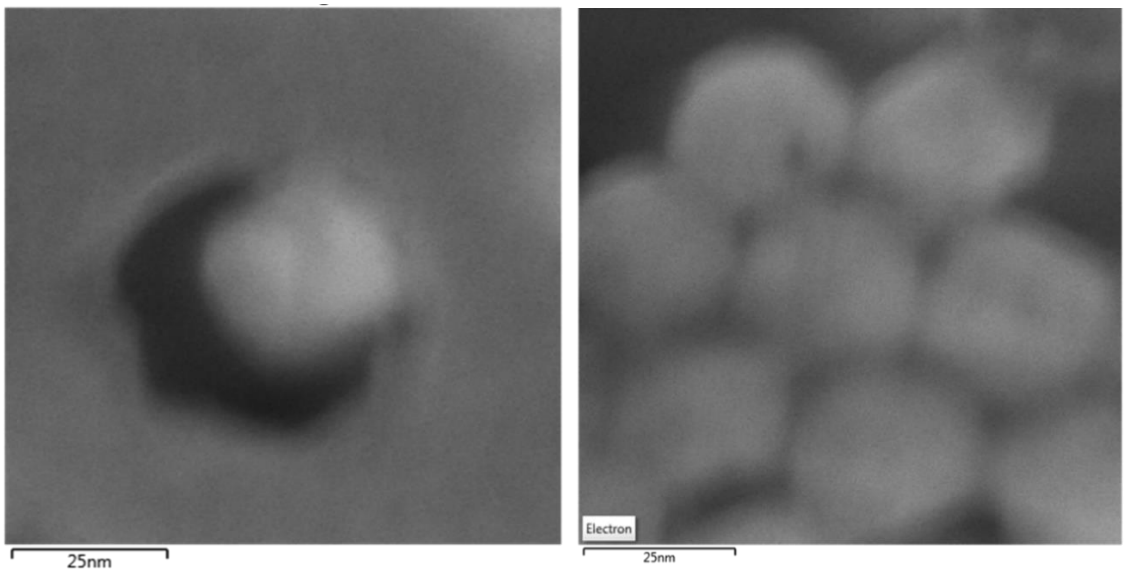

Figure 3.6: Secondary electron (filament operated at 20 kV) images of UCNPs after heating.

Figure 3.7 shows the Y, Yb, and Er EDS maps collected of particles after high temperature annealing and Figure 3.5 (c) shows elemental maps of all three elements in a NP, overlaid in Figure 3.5 (d). Relative abundances of the lanthanide ions in circular regions were again calculated and plotted as seen in Figure 3.5 (e) and (f). Here, it is clearly seen that after heating, the ratios Yb/Y and Er/Y are more homogeneous over the particle. Comparing the redistribution of Yb/Y to Er/Y, a crossing point between the data pre-heating and post-heating is observed at a different average distance to the particle center.

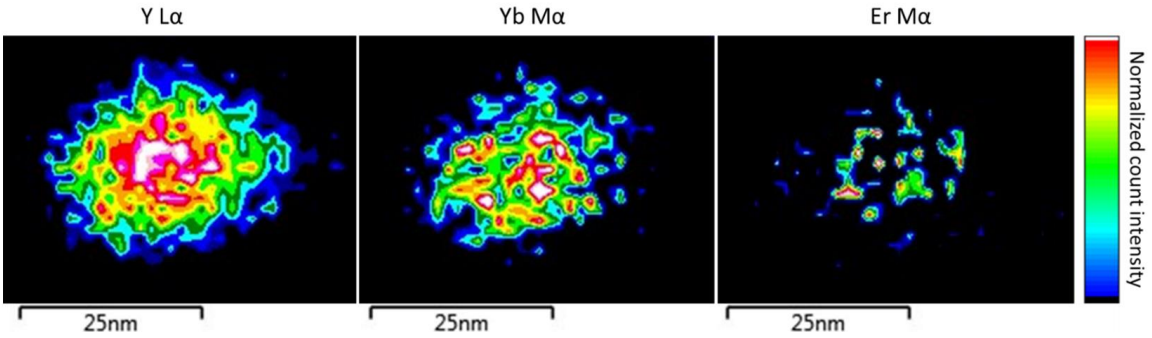

Figure 3.7: EDS maps of UCNPs after heating at 590 °C. Spatial distribution of Y $L\alpha_1$ (left), Yb Mα (middle) and Er Mα (right) are shown, where the color indicates the number of counts normalized to the highest peak in the image as indicated in the color bar to the right.

When interpreting the data in 3.5 (e) and (f), it should be noted that volumes of the material in each of the rings are not equal to each other. Besides the fact that the 2-dimensional area of the rings increases with its respective radius, the thickness of material in each of the rings varies as well, and this cannot be accounted for. Furthermore, the number of x-ray counts does not linearly scale with the quantity of the element of interest, due to dependence on sample thickness and composition. Because of this, the area under the curves is not expected to stay constant, and material loss is not necessarily implied by the observed changes. Because of this, an absolute quantification of the elements is not possible, but the curves provide a useful way of visualizing qualitative trends in the elemental maps, which were based on a relatively small number of x-ray photon counts.

A homogeneous distribution of the ions was hypothesized to have a positive impact on the up-conversion quantum yield. To see whether heating the nanoparticles had any effect on the up-conversion efficiency, emission intensities in the visible region upon 980 nm

excitation before and after heating at 590 °C were measured, as shown in Figure 3.8. When the emission spectra are compared, both emission intensities seem very similar.

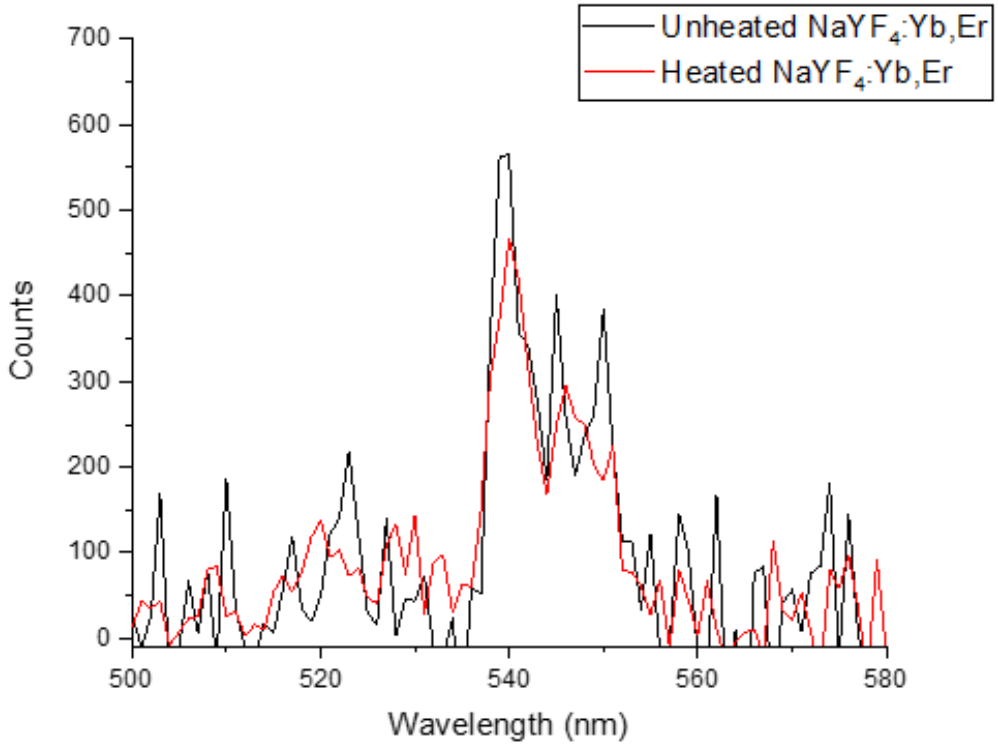

Figure 3.8: Emission measured upon excitation at 980 before heating at 590 °C (black), and after (red).

A variety of groups have reported different dopant concentrations for optimal quantum yield in bulk up-conversion crystals of $NaYF_4$ doped with Yb and Er. Kano et al. report 39% Yb and 4% Er,[19] Zeng *et al.* report 20% Yb and 1% Er,[15] and Krämer et al. report 18% Yb and 2% Er.[16] From their results, the groups report a strong dependence of the optimal QY on the doping concentration used, where it is argued that if the doping levels are too high, cross-relaxation between excited state Er^{3+} ions may take place, resulting in a decrease of emission intensity. Zeng et al. in particular noted a strong (~5 fold) decrease

in emission intensity going up from 1% to 1.5% Er concentration.[15] Similarly, a change in two times the concentration of Er from the center to the edge that is observed in the nanoparticles was expected to influence the emission intensity significantly.

The observation that ions were distributed equally after heating while the emission intensity under the same conditions stays the same suggests that inhomogeneous ion distribution is not the main cause for the reduced QY in nano-sized UC crystals. While energy transfer from sensitizer Yb ions to emitting Er ions may have been made more efficient, energy may still be transferred to defect states at the nanoparticle surface, quenching their luminescence. This effect has been argued to be largely mitigated in previous work by growing up to 10 nm thick homogeneous shells around UCNPs.[13]

Besides cross-relaxation effects from an increased average Er-Er distance and energy transfer to surface defects, internal defects inside the UCNP crystals may quench emission of the exited state. Possible candidates for internal defects are OH^- point defects. OH^- is present in the nanoparticle synthesis from the NaOH used. Coupling to the O-H stretching vibration leads to quenching of the 10,000 cm^{-1} excited state of ytterbium. A simple vibrational spectroscopy experiment was performed, showing a vibrational peak at 3,600 cm^{-1}, see Figure 3.9. The peak can be attributed to an O-H stretch vibration in the absence of hydrogen bonding, peaks at this energy have been observed for OH^- ions in halide crystals.[20] This may indicate the presence of OH^- inside the NPs. The sample was washed with D_2O to remove any potential OH groups on the nanoparticle surface, which led to a decrease of the vibrational peak, suggesting they predominantly reside at the nanoparticle

surface. No clear O-D stretch vibration was observed in the region around 2500 cm^{-1}, see SI. This may be due to overlap with the tail end of the very large C-H vibrational peak combined with the lower signal expected for the O-D vibration due to its lower oscillator strength, as compared to that of the O-H vibration (the latter already being a weak signal).[21] A small peak O-H vibration peak remains after washing, so the presence of OH^- groups inside the crystal cannot be ruled out. Simply heating the nanocrystals might not be sufficient to get rid of the OH^- groups, which could explain why there isn't an increase in emission intensity after treating the nanocrystals at 590 °C. Previous studies have shown that the presence of D_2O can increase the up-conversion efficiency of UCNPs by only a factor of about 2,[22] but the observation that growing protective shells that are so thick that no energy transfer to the surface is expected, is still insufficient to attain QYs shown in bulk material[8, 13] suggest that there are still internal crystallographic defects present.

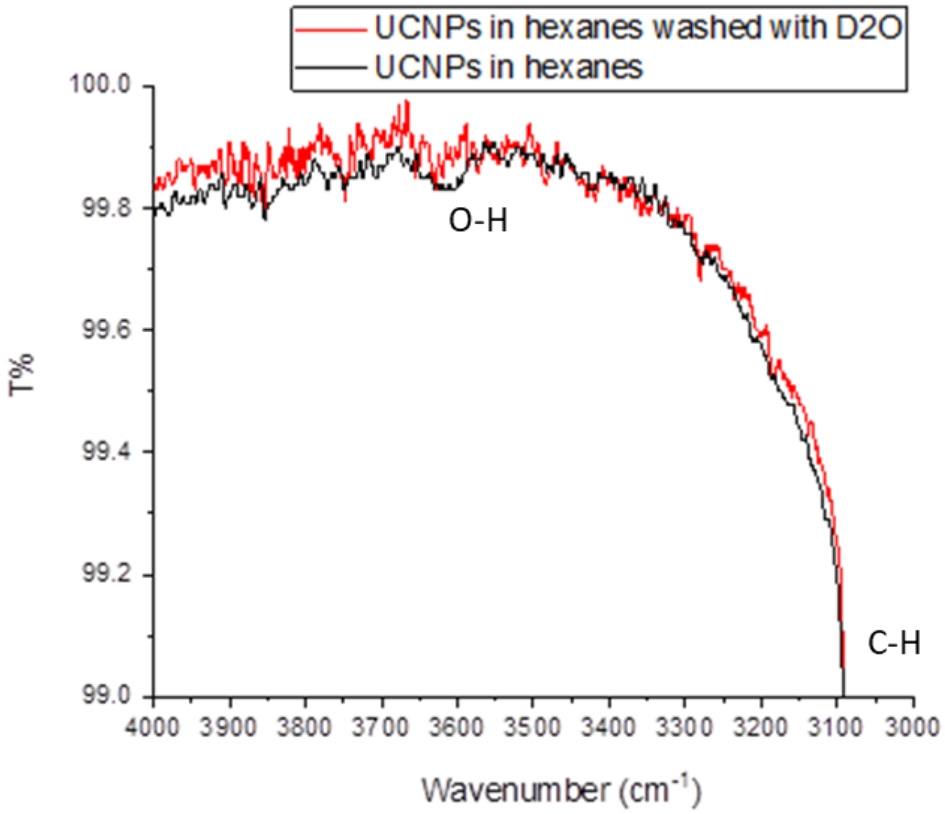

Figure 3.9: Vibrational spectroscopy performed on UCNPs before (black) and after (red) washing with D_2O, plotted between 100 and 99 T% and 4,000 and 3,000 cm^{-1} to highlight region of interest.

From the presented results it is inferred that there are internal crystallographic defects in the UCNPs post colloidal synthesis, that are still present after heating at 590 °C. A future study to verify the presence of these defects could in principle involve electron holography, which has previously been employed to demonstrate internal crystallographic defects in different materials.[23] Applying this technique to lanthanide based colloidal UCNPs comes with its own challenge, as electron holography is a high electron dose technique, and $NaLnF_4$ particles have been shown to be highly susceptible to electron beam damage.[24-25]

It is further worth noting that while annealing the nanoparticles at elevated temperatures does not appear to increase their quantum yield, the localized distribution of the sensitizer and emitter ions does have implications for other applications of lanthanide-doped nanoparticles. For example, in the development of singly doped nanoparticles for single photon emission applications, it is assumed that the ions in the particles are randomly distributed.[26] Localization of dopant ions inside the nanocrystals may have implications for the distribution of ions over the ensemble, causing a deviation from purely statistical distributions, which can in turn lead to optical losses.

Finally, the redistribution of ions to a more homogenous occupation after high temperature annealing holds implications for high temperature applications of lanthanide-doped nanoparticles. Lanthanide-doped nanoparticles have been used for high temperature luminescence-based thermometry.[5] While the redistribution of dopant ions may not be large enough to change the overall effect on thermometry, results using core/shell materials may be complicated by the redistribution of ions.[27] An implication of the observations is that ions may diffuse into the shell material, drastically changing the ion-ion distance, and thus the optical properties.

3.3 Conclusions

In this chapter, a study investigating the internal structure of Yb^{3+} and Er^{3+} co-doped nanoparticles was presented. $NaYF_4$ doped with 18% Yb^{3+} and 2% Er^{3+} was synthesized and analyzed with TEM and XRD. The ion distribution inside the nanoparticles was investigated with high-resolution EDS. It was found that the dopant ions were localized in the nanoparticle center, as a possible result of the different reactivities of the lanthanide

ions in the colloidal synthesis. Heating the nanoparticles at 590 ^{o}C resulted in a more homogenous distribution of the lanthanide ions over the nanoparticles. To verify whether the homogenous distribution increased the up-conversion properties of the nanoparticles, emission measurements were performed at 980 nm excitation. It was found that the heating barely influenced the emission intensity under the same photon flux. This implies that inhomogeneous ion distribution is not a major reason for the reduced quantum yields observed in UCNPs, as compared with their bulk counterpart. Besides surface quenching, possible quenchers could manifest as internal defects in the crystals. The possibility of OH^- being present was briefly investigated with vibrational spectroscopy, but only a weak indication of OH^- being present inside the particles was found. The results presented in this chapter hold important implications for a variety of applications for lanthanide-doped nanoparticles, including singly doped nanoparticles for single photon emitters, and luminescence thermometry.

3.4 Experimental methods

Chemicals. Yttrium(III) chloride hexahydrate (99.99%), erbium(III) chloride hexahydrate (99.995%), ytterbium(III) chloride hexahydrate (99.998%), ammonium fluoride (99.99%), tech grade oleic acid (90%), tech grade 1-octadecene (ODE, 90%), and hexanes were purchased from Sigma-Aldrich. Anhydrous ethanol from Commercial Alcohols, methanol from Caledon, and sodium hydroxide from Bio Basic Canada Inc. were used. All chemicals were used as received.

Synthesis UCNPs. 0.8 mmol YCl_3•6(H_2O), 0.18 mmol $YbCl_3$•6(H_2O), and 0.02 mmol $ErCl_3$•6(H_2O) were weighed and introduced into a 100 mL three neck round-bottom flask. 15 mL 1-Octadecene and 6 mL oleic acid were added. The mixture was stirred at a moderate pace, but low enough that the surface of the liquid remained level. This was then heated with a heating mantle to 140 °C over 30 minutes under vacuum, and kept at that temperature for 1 hour. The mixture turned clear and slightly yellow. This was cooled to 60 °C over 15 minutes and a solution of 10 mL methanol with 2.5 mmol NaOH and 4 mmol NH_4F was introduced drop-wise. The resulting mixture was heated at 70 °C until methanol had evaporated, which was after ca. 30 min. The mixture was then heated to 300 °C over 15 min. The temperature was kept at 300 °C for 90 minutes before the heating mantle was removed and the mixture was allowed to cool to room temperature. This was then added to 30 mL ethanol in a centrifugation tube and centrifuged at 3,000 g for 10 min. The resulting supernatant was discarded, and the pellet at the bottom was redispersed in 20 mL hexanes.

Nanoparticle characterization. Transmission electron microscopy images were obtained using a JEOL JEM-1400 microscope operating at 80 kV. Hexane dispersions of the NPs were drop-cast on a formvar carbon-coated grid (300 mesh Cu) and air-dried before imaging. Size analysis of NCs from the images was performed digitally by measuring the surface area of at least 1,000 particles with the program ImageJ (version 1.52p) and calculating the corresponding diameter. X-ray diffractograms with a resolution of 0.0263 °(2θ) were collected using a PANalytical Empyrean X-ray System with a Cu source (Kα radiation, λ = 1.54060 Å) operating at 45 kV and 40 mA.

EDS analysis. EDS spectra were collected on UCNPs deposited on holey Si TEM grids in two-dimensional 256 x 256 pixel rosters using a Hitachi SU9000 SEM/STEM microscope operating at 10 keV. Using Matlab, circular masks were made in specific areas of interest. The EDS spectra in each of the pixels in these areas were summed and characteristic elemental EDS peaks were fitted to these spectra using the Hyperspy Python library. The relative presence of the elements in the areas was deduced from the relative intensity of the peaks.

Fluorescence emission spectroscopy. Emission spectroscopy was performed exciting with a JDS Uniphase 980 nm pump laser diode operating at 1.6 W. The diode was coupled to an optical fiber and the emission of the fiber tip collimated to ca. 3 mm^2 using a Newport F-91-C1-T multimode fiber coupler, where the resulting photon flux is estimated to be around 50 W/cm^2. The emission was measured and corrected for instrument response using a cooled Hamamatsu R928P PMT between 400 and 700 nm. Counts were integrated for 1 s at every 1 nm step using a 1 nm slit width. The detector was positioned at a 90-degree angle with respect to the excitation source. Si TEM grids were affixed at a 45-degree angle with respect to both the excitation source and the detector, position to be in the center of the laser beam. A 900 nm short-pass filter was placed between the sample and the detector.

Post-synthetic heating of NPs in oven. The Si TEM grid on which the EDS was performed was placed inside a tube oven. Argon was flowed over the tube. The temperature in the oven was ramped from room temperature to 590 °C over 0.5 hours, kept at 590 °C for 2 hours, then cooled to room temperature over 1 hour.

3.5 References

1. Park, Y. I.; Kim, H. M.; Kim, J. H.; Moon, K. C.; Yoo, B.; Lee, K. T.; Lee, N.; Choi, Y.; Park, W.; Ling, D., Theranostic Probe Based on Lanthanide-Doped Nanoparticles for Simultaneous in Vivo Dual-Modal Imaging and Photodynamic Therapy. *Adv. Mater.* **2012,** *24*, 5755-5761.
2. Prodi, L.; Rampazzo, E.; Rastrelli, F.; Speghini, A.; Zaccheroni, N., Imaging Agents Based on Lanthanide Doped Nanoparticles. *Chem. Soc. Rev.* **2015,** *44*, 4922-4952.
3. Haase, M.; Schäfer, H., Upconverting Nanoparticles. *Angew. Chem. Int. Ed.* **2011,** *50*, 5808-5829.
4. Gnach, A.; Bednarkiewicz, A., Lanthanide-Doped Up-Converting Nanoparticles: Merits and Challenges. *Nano Today* **2012,** *7*, 532-563.
5. Geitenbeek, R. G.; Prins, P. T.; Albrecht, W.; van Blaaderen, A.; Weckhuysen, B. M.; Meijerink, A., $NaYF_4$: Er^{3+}, Yb^{3+}/SiO_2 Core/Shell Upconverting Nanocrystals for Luminescence Thermometry up to 900 K. *J. Phys. Chem. C* **2017,** *121*, 3503-3510.
6. Sedlmeier, A.; Achatz, D. E.; Fischer, L. H.; Gorris, H. H.; Wolfbeis, O. S., Photon Upconverting Nanoparticles for Luminescent Sensing of Temperature. *Nanoscale* **2012,** *4*, 7090-7096.
7. Shariatdoust, M. S.; Frencken, A. L.; Khademi, A.; Alizadehkhaledi, A.; van Veggel, F. C. J. M.; Gordon, R., Harvesting Dual-Wavelength Excitation with Plasmon-Enhanced Emission from Upconverting Nanoparticles. *ACS Photonics* **2018,** *5*, 3507-3512.

8. Fischer, S.; Johnson, N. J. J.; Pichaandi, J.; Goldschmidt, J. C.; van Veggel, F. C. J. M., Upconverting Core-Shell Nanocrystals with High Quantum Yield under Low Irradiance: On the Role of Isotropic and Thick Shells. *J. Appl. Phys.* **2015,** *118*, 193105.

9. Wen, S.; Zhou, J.; Zheng, K.; Bednarkiewicz, A.; Liu, X.; Jin, D., Advances in Highly Doped Upconversion Nanoparticles. *Nat. Commun.* **2018,** *9*, 1-12.

10. Boyer, J. C.; van Veggel, F. C. J. M., Absolute Quantum Yield Measurements of Colloidal $NaYF_4$: Er^{3+}, Yb^{3+} Upconverting Nanoparticles. *Nanoscale* **2010,** *2*, 1417-1419.

11. Pokhrel, M.; Kumar, G.; Sardar, D., Highly Efficient NIR to NIR and VIS Upconversion in Er^{3+} and Yb^{3+} Doped in M_2O_2S (M= Gd, La, Y). *J. Mater. Chem. A* **2013,** *1*, 11595-11606.

12. May, P. S.; Baride, A.; Hossan, M. Y.; Berry, M., Measuring the Internal Quantum Yield of Upconversion Luminescence for Ytterbium-Sensitized Upconversion Phosphors Using the Ytterbium (III) Emission as an Internal Standard. *Nanoscale* **2018,** *10*, 17212-17226.

13. Fischer, S.; Bronstein, N. D.; Swabeck, J. K.; Chan, E. M.; Alivisatos, A. P., Precise Tuning of Surface Quenching for Luminescence Enhancement in Core–Shell Lanthanide-Doped Nanocrystals. *Nano Lett.* **2016,** *16*, 7241-7247.

14. Yi, G.-S.; Chow, G.-M., Water-Soluble $NaYF_4$: Yb, Er (Tm)/$NaYF_4$/Polymer Core/Shell/Shell Nanoparticles with Significant Enhancement of Upconversion Fluorescence. *Chem. Mater.* **2007,** *19*, 341-343.

15. Zeng, J. H.; Su, J.; Li, Z. H.; Yan, R. X.; Li, Y. D., Synthesis and Upconversion Luminescence of Hexagonal-Phase $NaYF_4$: Yb, Er^{3+} Phosphors of Controlled Size and Morphology. *Adv. Mater.* **2005,** *17*, 2119-2123.

16. Krämer, K. W.; Biner, D.; Frei, G.; Güdel, H. U.; Hehlen, M. P.; Lüthi, S. R., Hexagonal Sodium Yttrium Fluoride Based Green and Blue Emitting Upconversion Phosphors. *Chem. Mater.* **2004,** *16*, 1244-1251.

17. Li, Z.; Zhang, Y., An Efficient and User-Friendly Method for the Synthesis of Hexagonal-Phase $NaYF_4$: Yb, Er/Tm Nanocrystals with Controllable Shape and Upconversion Fluorescence. *Nanotechnology* **2008,** *19*, 345606.

18. Rabouw, F. T.; Prins, P. T.; Villanueva-Delgado, P.; Castelijns, M.; Geitenbeek, R. G.; Meijerink, A., Quenching Pathways in $NaYF_4$:Er^{3+},Yb^{3+} Upconversion Nanocrystals. *ACS nano* **2018,** *12*, 4812-4823.

19. Kano, T.; Yamamoto, H.; Otomo, Y., $NaLnF_4$: Yb^{3+}, Er^{3+}(Ln: Y, Gd, La): Efficient Green-Emitting Infrared-Excited Phosphors. *J. Electrochem. Soc.* **1972,** *119*, 1561.

20. Weddin, B.; Klein, M. V., Infrared Absorption of the Hydroxyl Ion in Alkali Halide Crystals. *Phys. Rev.* **1969,** *177*, 1274.

21. De Marco, L.; Carpenter, W.; Liu, H.; Biswas, R.; Bowman, J. M.; Tokmakoff, A., Differences in the Vibrational Dynamics of H_2O and D_2O: Observation of Symmetric and Antisymmetric Stretching Vibrations in Heavy Water. *J. Phys. Chem. Lett.* **2016,** *7*, 1769-1774.

22. Bogdan, N.; Vetrone, F.; Ozin, G. A.; Capobianco, J. A., Synthesis of Ligand-Free Colloidally Stable Water Dispersible Brightly Luminescent Lanthanide-Doped Upconverting Nanoparticles. *Nano Lett.* **2011,** *11*, 835-840.

23. Midgley, P. A.; Dunin-Borkowski, R. E., Electron Tomography and Holography in Materials Science. *Nat. Mater.* **2009,** *8*, 271-280.

24. Feng, W.; Sun, L. D.; Zhang, Y. W.; Yan, C. H., Solid-to-Hollow Single-Particle Manipulation of a Self-Assembled Luminescent $NaYF_4$: Yb, Er Nanocrystal Monolayer by Electron-Beam Lithography. *Small* **2009,** *5*, 2057-2060.

25. Sun, X.; Wang, B.; Kempson, I.; Liu, C.; Hou, Y.; Gao, M., Restructuring and Remodeling of $NaREF_4$ Nanocrystals by Electron Irradiation. *Small* **2014,** *10*, 4711-4717.

26. Sharifi, Z.; Dobinson, M.; Hajisalem, G.; Shariatdoust, M. S.; Frencken, A. L.; van Veggel, F. C. J. M.; Gordon, R., Isolating and Enhancing Single-Photon Emitters for 1550 nm Quantum Light Sources Using Double Nanohole Optical Tweezers. *J. Chem. Phys.* **2021,** *154*, 184204.

27. Kaczmarek, A. M.; Suta, M.; Rijckaert, H.; van Swieten, T. P.; Van Driessche, I.; Kaczmarek, M. K.; Meijerink, A., High Temperature (Nano) Thermometers Based on $LiLuF_4$: Er^{3+}, Yb^{3+} Nano-and Microcrystals. Confounded Results for Core–Shell Nanocrystals. *J. Mater. Chem. C* **2021,** *9*, 3589-3600.

Chapter 4: Isolating and Enhancing Single Er^{3+} Emitters for Single Photon Sources in the 1,550 nm Telecom Window

Based on:

Alizadehkhaledi, A.; Frencken, A. L.; Dezfouli, M. K.; Hughes, S.; van Veggel, F. C. J. M.; Gordon, R., Cascaded Plasmon-Enhanced Emission from a Single Upconverting Nanocrystal. *ACS Photonics* 2019, *6*, 1125-1131.

Alizadehkhaledi, A.; Frencken, A. L.; van Veggel, F. C. J. M.; Gordon, R., Isolating Nanocrystals with an Individual Erbium Emitter: A Route to a Stable Single-Photon Source at 1550 nm Wavelength. *Nano Lett.* 2020, *20*, 1018-1022.

Sharifi, Z.; Dobinson, M.; Hajisalem, G.; Shariatdoust, M. S.; Frencken, A. L.; van Veggel, F. C. J. M.; Gordon, R., Isolating and Enhancing Single-Photon Emitters for 1550 nm Quantum Light Sources Using Double Nanohole Optical Tweezers. *J. Chem. Phys.* 2021, *154*, 184204.

Trapping experiments were performed by Amirhossein Alizadehkhaledi (UVic) and Zohreh Sharifi (UVic). FDTD simulations were done by Stephen Hughes (QueensU). The experimental sections detailing the nanohole fabrication and trapping experiments were provided by Amirhossein Alizadehkhaledi (UVic) and Zohreh Sharifi (UVic).

Abstract

Stable single-photon emitters are in high demand for their use in quantum computation and secure quantum information transfer (cryptography). Recent efforts have mainly focused on emitters in the visible light range, which would be subject to heavy losses in optical fibers. In this chapter, it is demonstrated how gold plasmonic structures can be used to enhance the radiative rate of Er^{3+} ions in up-converting nanoparticles (UCNPs) and nanoparticles doped with on average single Er^{3+} ions, while also functioning as a selection mechanism to trap selectively singly doped nanoparticles. Rectangular gold nano-apertures were used to demonstrate optical trapping of single UCNPs, followed by demonstration of emission enhancements of up to 400x by local field enhancement of the gold surface plasmon. The strong emission enhancement allowed us to measure emission from particles doped with around a single Er^{3+} ion. Discrete emission levels were observed, following closely a Poisson distribution as expected from the stoichiometry in the colloidal synthesis. Double gold nano-holes were also used to demonstrate the discrete emission levels as well. Here emission enhancements of up to 2,000x times were observed. The results presented here form a strong precedent to develop stable single emitters at 1,550 nm using singly doped nanoparticles in gold nano-apertures.

4.1 Introduction

Reliable sources of single photons on demand are sought after for applications in quantum information science. Protocols have been proposed where a single photon can be used to transfer information with unconditional security. Furthermore, single photons are proposed to be utilized to perform quantum computation tasks not possible via classical computation.[1-3]

A variety of materials is being researched for their use as a single-photon source. Nitrogen-vacancy (NV) color centers in diamond are potential candidates, but this strategy primarily leads to photons emitted in the visible range, where losses in optical fibres are relatively high.[4-6] Quantum dots that generate photons in the infra-red have been proposed as well,[7-9] but they have the downside that their emission is not stable over time, due to, among others, 'blinking'.[10-12] In this chapter, single Er^{3+} ions are proposed as a source of single photons, due their stable emission at 1,550 nm, which is in the low-loss optical telecommunication window.[13-14]

The emission intensity of a single lanthanide ion is typically extremely low as a result of the forbidden nature of the intra-4f transitions.[15] To overcome this problem, local field enhancement using surface plasmon resonance can be used.[16-18] The radiative rate of emitters scales with the local density of states (LDOS) which has been shown to be enhanced by electric field enhancement in the presence of surface plasmons in the cavity of gold nano-structures.

Another challenge that accessing single Er^{3+} ions poses is that inside Er^{3+}-doped host materials, dopant ions are distributed randomly. This means that even in dilutely doped materials, a high likelihood exists of Er^{3+} ions being bunched up, and finding a single Er^{3+} ion that is well separated from other emitters can be arduous.[14] To find single Er^{3+} ions, optical tweezers may be utilized, in combination with a system of nanoparticles that mostly contain a single Er^{3+} ion. Optical tweezers have been used widely to trap single molecules or nanoparticles.[19-20] In an optical tweezer, a light-beam is tightly focused, forming a strong electric field gradient at the beam waist, which can attract and trap dielectric particles.[21-22]

Here, a strategy to access single Er^{3+} ions is presented, using optical tweezers in plasmonic gold nano-apertures. This strategy allows both for selection of nano-particles doped with a single ion, as well as for enhancement of the single emitter emission intensity, allowing for spectroscopy with conventional detectors. The strategy is first demonstrated on UCNPs (see previous chapter for details on UCNP structure), trapping them with rectangular gold nano-apertures. The emission enhancement is described in its relation to the local field enhancement.

After successful demonstration of a strong emission enhancement, the method was used on $NaYF_4$ NPs that were doped very dilutely with Er^{3+} ions. The dopant levels were chosen so that the majority of the NPs had a single Er^{3+} ion in them, assuming a Poisson distribution of the ions over the ensemble. Observation of emission of these dilutely doped NPs was followed by optimization of the gold nano-hole apertures. Instead of a rectangular hole, double-circular nano-holes were used, under the hypothesis that at the waist of the

hole, local field enhancement could be even larger than in the rectangular holes, and the emitter radiative rate would thus be higher too.[23]

In this chapter, the optical trapping of UCNPs and nanoparticles doped with around 1 Er^{3+} ion is described. The synthesis of the NPs and the predicted Er^{3+} concentrations per NP are described. Optical trapping is demonstrated in gold aperture holes of rectangular and double-circular shape are demonstrated. Er^{3+} emission is shown to be strongly enhanced by field enhancement of the gold surface plasmon and discrete emission intensities are observed in the dilutely Er^{3+} doped NPs.

4.2 Results and discussion

As a model system to investigate emission enhancement of Er^{3+} emitters, $NaYF_4$ doped with 18% Yb^{3+} and 2% Er^{3+} UCNPs were used in conjunction with gold nano-aperture optical tweezers. The synthesis of the UCNPs was highly similar to the ones described in an earlier chapter, which are based on previously reported methods.[24] Here, the synthesis involves heating lanthanide chloride precursors in the presence of oleic acid under vacuum at 160 ^{o}C, followed by introduction of NaOH and NH_4F and heating to 298 ^{o}C. The temperature was kept between 305 and 307 ^{o}C for 90 minutes, before removing the heating and allowing the mixture to cool to room temperature. TEM and XRD were performed after washing the nanoparticles with ethanol, centrifugation, and redispersion of the supernatant in hexanes.

TEM images are shown in Figure 4.1, together with a histogram showing the measured diameter distribution. The average NP diameter is 26.17 nm with a standard deviation of 2.65 nm. The XRD diffractogram is shown in the bottom right of Figure 4.1, together with a reference diffractogram of β-$NaYF_4$. The peaks align well, and no evidence for other phases or impurities is seen.

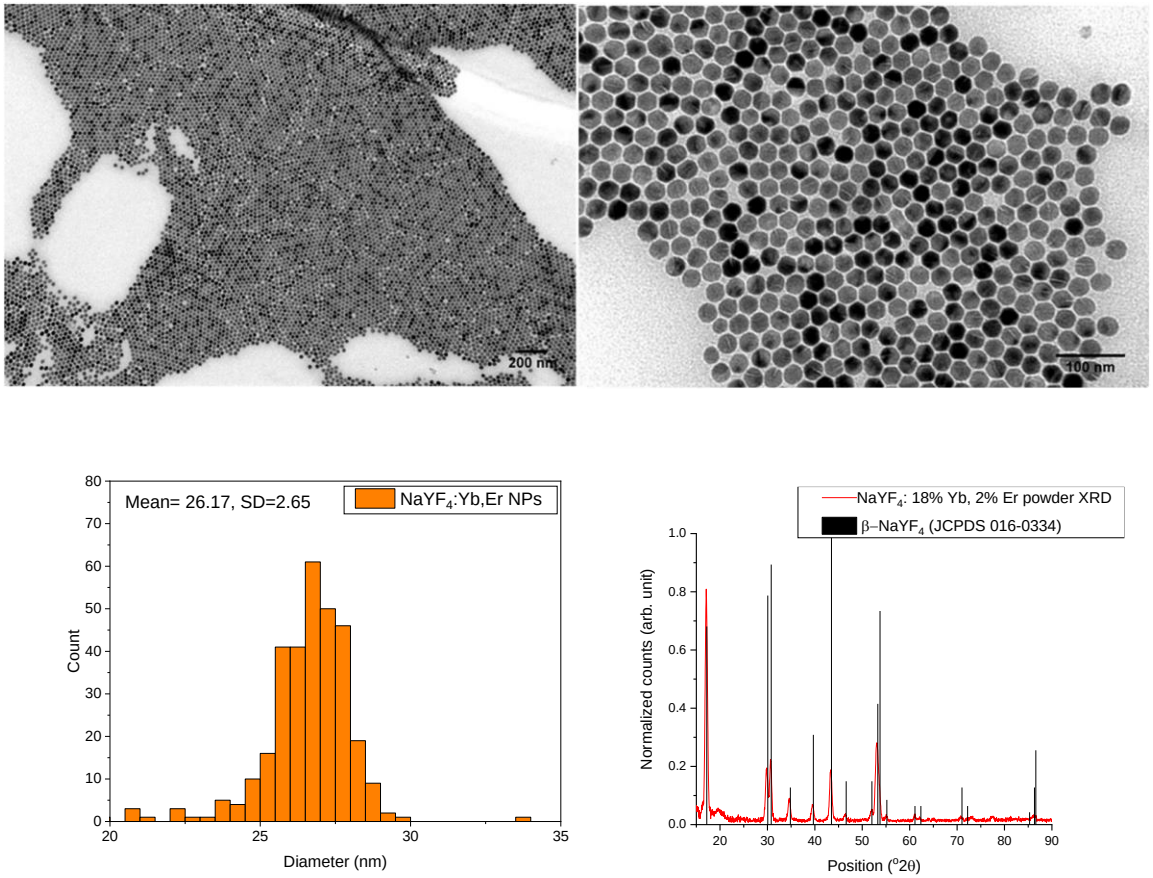

Figure 4.1: Electron microscopy images of $NaYF_4$:18%Yb,2%Er NPs at 100k magnification (left) and 250k magnification. A histogram of measured NP diameters is shown in the bottom left graph. The x-ray diffractogram of the NPs is shown in the bottom right (red) with a reference diffractogram in black.

The up-conversion of the UCNPs was demonstrated by excitation at 980 nm, and measurement of photoluminescence in the visible region. Figure 4.2 shows the emission spectrum. All the characteristic Er^{3+} emission peaks in the visible region can be observed resulting from transition back to the $^4I_{15/2}$ ground state from the $^4F_{9/2}$, (red) $^4S_{3/2}$, (green), $^2H_{9/2}$ (blue), and $^4G_{11/2}$ (around 380 nm) excited states.

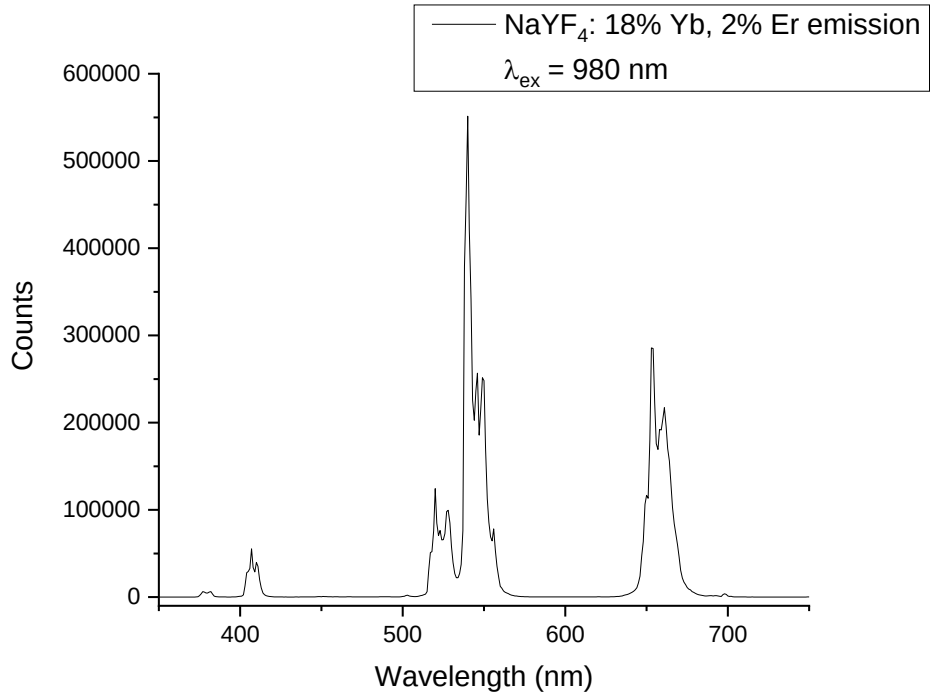

Figure 4.2: Characteristic Er^{3+} emission spectrum collected upon excitation at 980 nm.

The results are typical for a colloidal UCNP synthesis and the particles are deemed fit for trapping experiments.

The particles were trapped in rectangle shaped gold nanoholes. For the trapping, a 980 nm laser was used. A range of hole sizes in a 100 nm thick gold film was used. The aperture

width was 100 nm, and the length varied from 100 nm to 225 nm. The gold aperture nanoholes were made using a focused ion beam, milling a 100 nm thick gold film on a glass slide with a 5 nm thick Ti adhesive layer.

The intensity of the 980 nm trapping laser transmission was measured during the trapping events. Successful trapping was confirmed by a rise in intensity of transmitted light through the aperture, as well as by the observation of measurable up-conversion emission.

Up-conversion emission from the trapped UCNPs was measured in the visible region, see Figure 4.3. From comparison of the emission intensity measured at 550 nm and 650 nm in the aperture with the emission measured in the free solution, emission enhancement factors could be calculated. For each aperture width, the enhancement factor for 550 nm and 650 emission is shown in Figure 4.3 (right).

Here, the highest enhancement factors were observed in apertures with 208 nm and 212 nm aperture lengths. The much larger enhancement at these specific dimensions can be explained by an increase in the Purcell enhancement factor for 980 nm light in apertures with these dimensions, which consequently gives the increase in radiative rate. Finite difference time domain (FDTD) simulations were performed by the collaborating team to predict the electric field value in the apertures, as well as to predict the radiative enhancement as a function of aperture length, see Figure 4.4. From the calculations an enhancement of three orders of magnitude is expected at gold aperture dimensions around 100 x 200 nm, for excitation at 980 nm.[25]

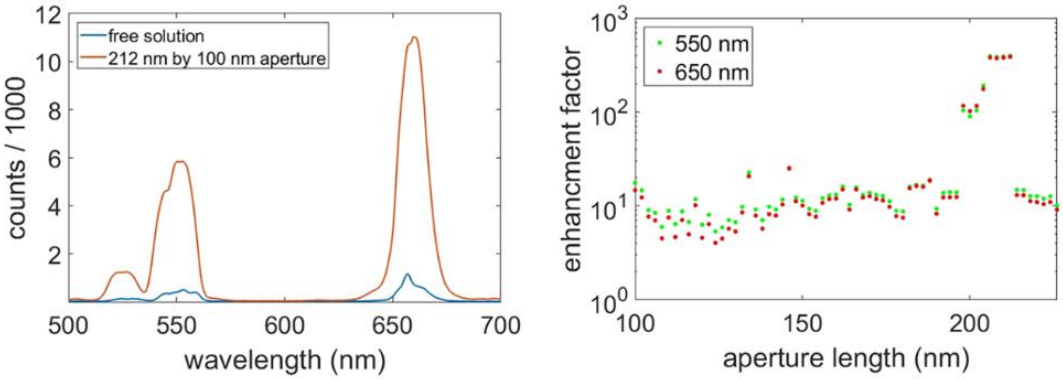

Figure 4.3: Comparison of Er^{3+} emission in solution with Er^{3+} emission in 212 nm by 100 nm gold aperture (left). Enhancement factor of the measured emission at 550 nm (green) and 650 nm (red) measured at various aperture lengths (right).

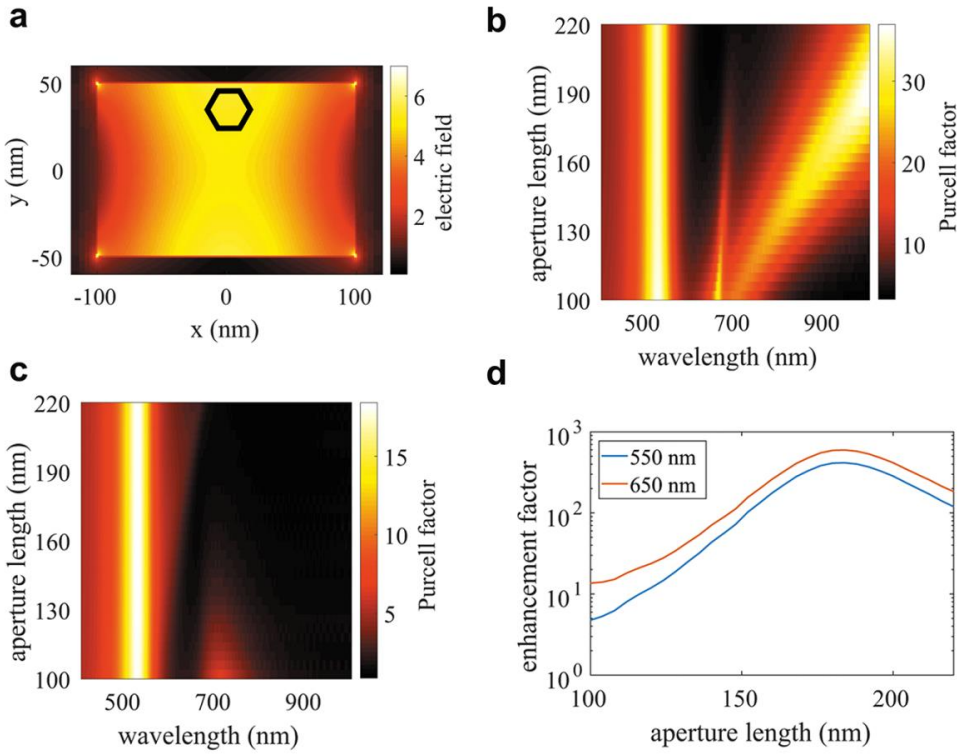

Figure 4.4: (a) FDTD simulated electric field in nanoaperture. Predicted location of UCNP is shown in black. Predicted Purcell factor enhancement at various wavelength and aperture length for light polarized along short axis (b), and long axis (c). (d) The predicted enhancement factor at corresponding aperture lengths.

After observation of these strong emission enhancements in UCNPs, $NaYF_4$ NPs doped with extremely low amounts of Er^{3+} were investigated as well. The synthesis of $NaYF_4$ NPs with small amounts of Er^{3+} was highly similar to the previously described syntheses of UCNPs. The difference is that for the lanthanide precursors, only 1 mmol YCl_3 was used together with a very small amount of Er^{3+}-oleate solution. The amount of Er^{3+} added in these syntheses was chosen so that the resulting NPs would have mostly 0 or 1 Er^{3+} inside, assuming Poisson statistics.[26]

Three batches of $NaYF_4$ NPs doped with trace Er^{3+} were made, each with a different concentration Er^{3+}. The batches were made with Er/Y ratio $1/10^7$ (TEM in Figure 4.5), Er/Y ratio $2/10^6$ (TEM in Figure 4.6), and Er/Y ratio $2/10^5$ (TEM in Figure 4.7). Next to the representative TEM images, diameter distributions are shown in histograms. The size distribution is narrow, and it can be observed that the nanoparticles form a 2-dimensional lattice on the TEM grid.

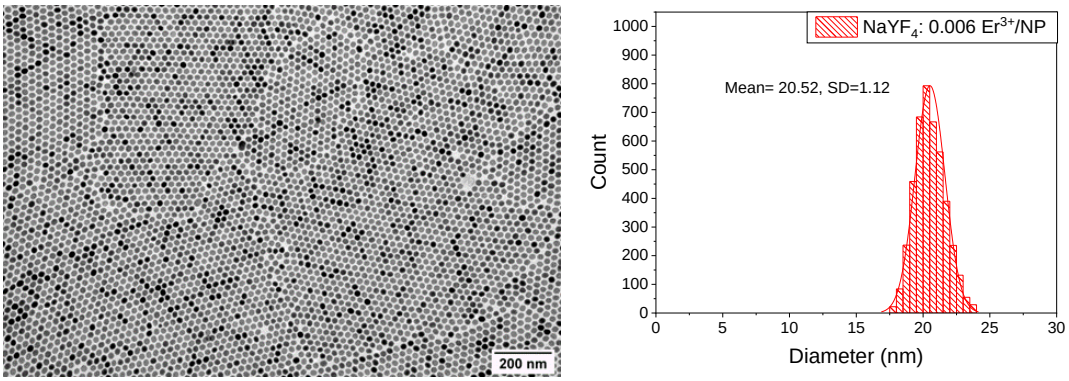

Figure 4.5: TEM and size distribution of measured $NaYF_4$:Er^{3+} NPs (~0.006 Er^{3+} / NP) with a mean diameter of 20.52 nm and standard deviation of 1.12 nm.

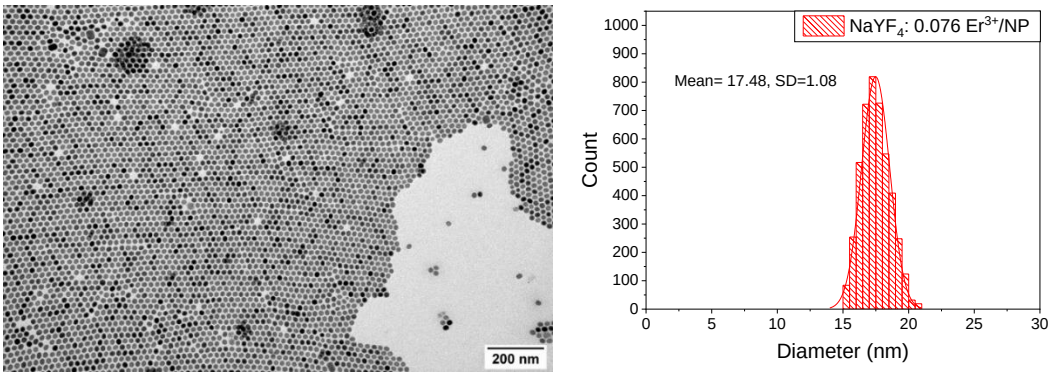

Figure 4.6: TEM and size distribution of measured $NaYF_4:Er^{3+}$ NPs (~0.076 Er / NP) with a mean diameter of 17.49 nm and standard deviation of 1.08 nm.

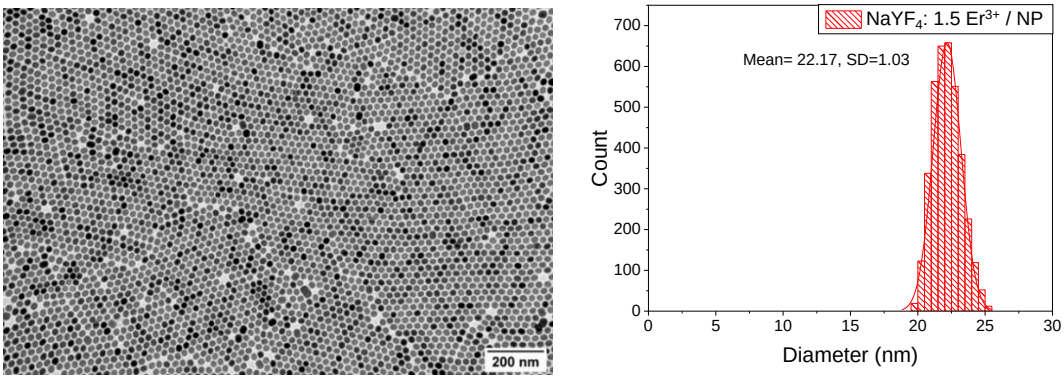

Figure 4.7: TEM and size distribution of measured $NaYF_4:Er^{3+}$ NPs (~1.5 Er^{3+} / NP) with a mean diameter of 22.17 nm and standard deviation of 1.03 nm.

Using the calculated diameters and the Er/Y ratio, the expected dopant concentration distributions in the NP ensembles could be calculated, assuming a Poisson distribution of the dopant ions in the particles, see Figure 4.8 for the predicted distributions.[26] From these calculations, the sample with $1/10^7$ Er^{3+} was predicted to have ca. 99% of the NPs undoped, ca. 1% doped with a single Er^{3+} ion, and negligible amounts of higher dopant levels. The sample with $2/10^6$ Er/Y was calculated to have ca. 93% undoped, ca. 7% doped with a single Er^{3+} ion, and negligible amounts of lower dopant levels. The sample that was doped

with $2/10^5$ was calculated to have much a much lower percentage of NPs with 0 Er^{3+}, only ca. 21%. 33% would have a single Er^{3+} ion, then 25% two Er^{3+} ions and so on.

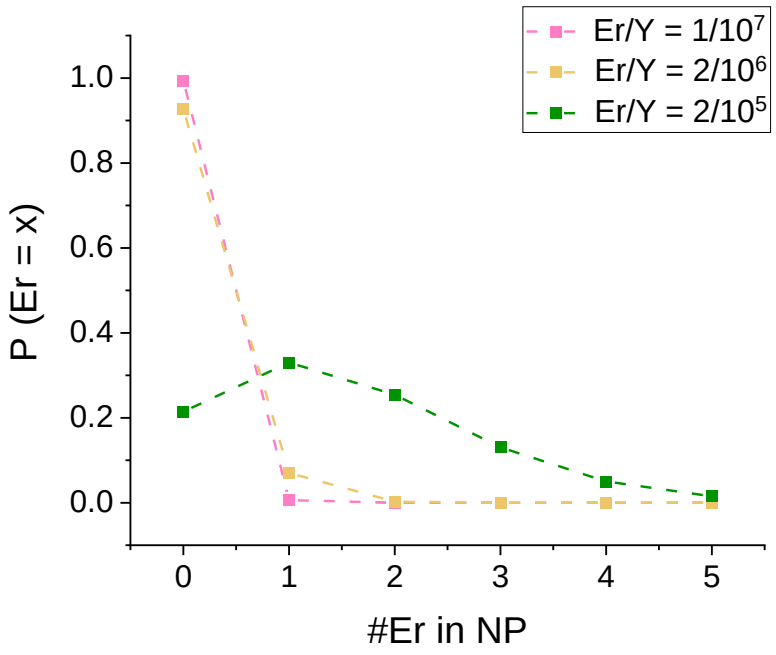

Figure 4.8: Distribution of Er^{3+} ions in the NP ensembles, based on Poisson statistics. P indicates the probability (out of 1) that the # Er^{3+} ions in a specific nanoparticle is equal to x.

To demonstrate the emission of dilutely doped NPs in gold nano-apertures, the sample doped with $2/10^5$ Er/Y, ca. 1.5 Er^{3+}/NP, was chosen. This sample shows the broadest distribution between 0-4 Er^{3+} per NP and was expected to be the best candidate to demonstrate a Poisson distribution in discrete emission intensities of measured single NPs.

Since the particles are proposed as emitters in the near infrared low-loss optical window, their emission in this region needed to be verified. Luminescence emission spectroscopy around 1,550 nm was performed on the ensemble in hexanes at 980 nm excitation, see

Figure 4.9. Emission intensity was very low due to the low emitting dopant concentration, so emission was measured and integrated for 8,000 seconds. A band of emission around 1,550 nm can be seen, which is attributed to the $^4I_{13/2} - {}^4I_{15/2}$ transition in Er^{3+}.

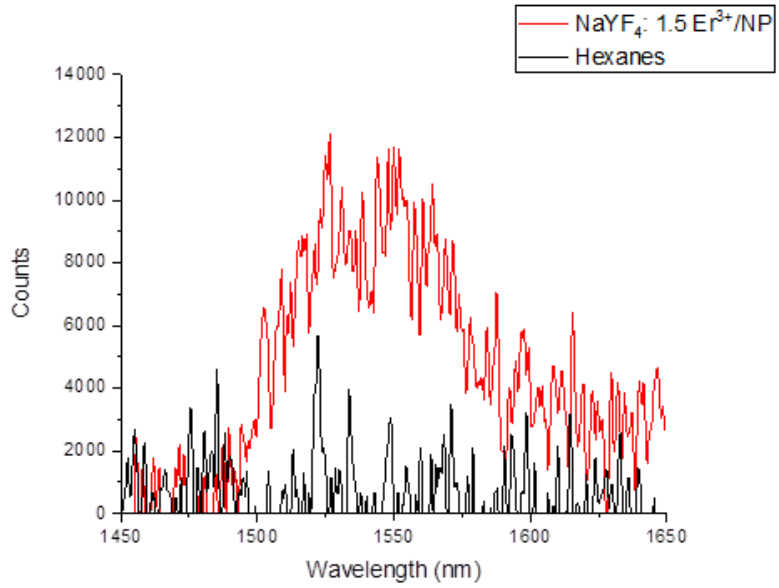

Figure 4.9: IR emission upon 980 nm laser excitation measured in $NaYF_4$ NPs in hexanes with an average of 1.5 Er^{3+} ions per NP, and on pure hexanes.

A similar trapping experiment as on the UCNPs was performed on these dilutely doped NPs. Particles were trapped in a 100 nm by 208 nm gold nano-aperture in a 100 nm thick gold film. Emission in the visible region was measured upon 980 nm excitation. Figure 4.10 (a) shows a schematic representation of dilutely doped $NaYF_4$ crystals as well as a representative scanning electron microscopy image of a rectangular hole in a gold nanofilm used for the trapping experiment. In Figure 4.10 (b), a spectrum of Er^{3+} emission at 660 nm is shown. Integration of the peak at 660 nm shows discrete emission levels that were compared to the Poisson distribution shown in the insert.

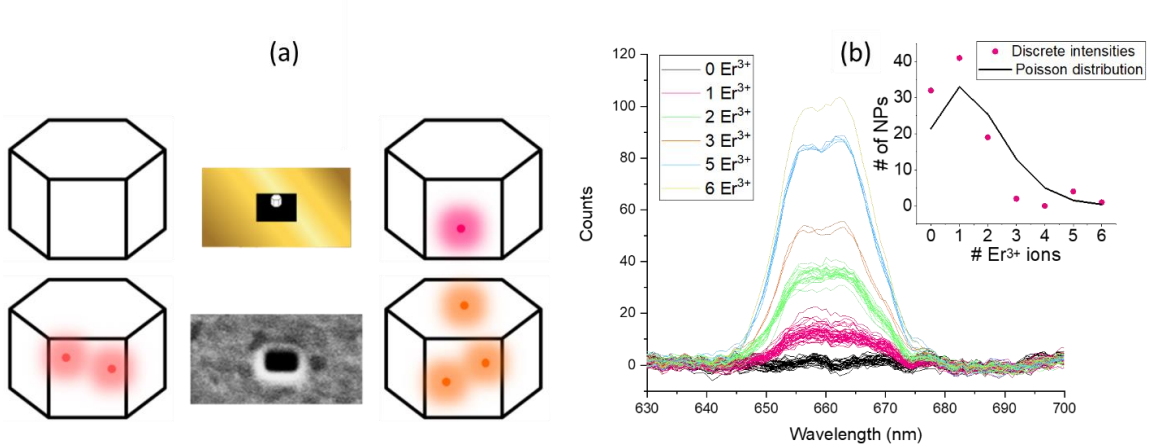

Figure 4.10: (a) Schematic representation of β-$NaYF_4$ nanoparticles with trace amounts of Er^{3+} in a rectangular gold aperture. Also shown is an SEM image of the aperture. (b) Comparison of discrete emission intensities with the predicted Poisson distribution.

The gold nano-apertures that were previously demonstrated to enhance the up-conversion emission by a factor of 400 prove strong enough to show emission of single NPs doped with an average of 1.5 emitting Er^{3+} ions. Furthermore, out of the ensemble of NPs that was individually trapped, discrete emission intensities could be observed, where the number of count intensities could be binned into (on average) 0, 15, 30, 45 etc. counts. The number of NPs in these respective groups closely followed a Poisson distribution.

Interestingly, the number of Er^{3+} ions per group seems slightly lower than predicted by the Poisson distribution. A possible explanation for this observation is that not each Er^{3+} ion inside the NPs may be emitting. An ion close to surface trap can transfer its energy non-radiatively, and its emission can thus not be measured. For a NP with diameter 22 nm, ca. 20% of the volume would lie within 1 nm of the NP surface, from which energy transfer can readily take place to a surface defect, likely leading to quenching of the Er^{3+} emitter.

A method to overcome this would be to grow thick shells around the NPs to prevent energy transfer to the surface.

The Er^{3+} emission intensity may also deviate from expected statistics by interaction of two or more Er^{3+} ions with each other inside a nanoparticle. A calculation was done to verify the expected distance between Er^{3+} ions in a very dilutely doped system. Formula (1) was used to calculate the average distance d based on lattice parameters a and c, and doping level x. The average Er^{3+}-Er^{3+} distances for NPs doped with 2, 3, 4, and 5 Er^{3+} ions are shown in Table 4.1. In all cases, the average distance between an Er^{3+} ion and its nearest neighbor is very high and energy transfer is unlikely. However, in the previous chapter we have demonstrated that dopant ions may not be statistically distributed, so behavior may vary from this prediction. If dopants are more localized, Er^{3+}-Er^{3+} interaction likelihood could be higher than predicted.

$$d = \left(\frac{a^2 \, c \sqrt{\frac{3}{2}}}{1.5 \, x} \right)^{1/3} \quad (1)$$

Table 4.1: Expected Er^{3+}-Er^{3+} distance at different dilute doping levels.

Er^{3+}/UCNC	Er^{3+}-Er^{3+} distance (nm)
2	14.05
3	12.27
4	11.16
5	10.35

While the yield of emitters was lower than expected, the optical trapping system conveniently allows for selecting those nanoparticles that do have a single emitting Er^{3+} ion. The rectangular gold nano-aperture is proven useful for simultaneous emission enhancement and selection for single emitters, using a dilutely doped Er^{3+} NP dispersion.

The encouraging results of measuring discrete emission levels from NPs doped with ca. 1 Er^{3+} ion were followed up by optimization of the gold nano-cavity. As an alternative to the rectangular apertures made in the gold films, the use of double nano-holes was explored. Double-nanohole gold apertures were made by drop-casting a dispersion of polystyrene beads unto a glass substrate. A 5 nm titanium layer was deposited as an adhesive, and a 70 nm gold layer was deposited on top of that. Polystyrene beads were then removed by sonication in toluene. Figure 4.11 (left) shows a scanning electron microscopy (SEM) image of a double nano-hole aperture in gold. The cusp length here is 32 nm and the diameter of a single hole is 222 nm. In the SEM image, an imprint of the polystyrene beads left behind after sonication can be seen as a dark circle.

Using a focused 980 laser beam, NPs could be trapped in the cusp of the double nano-hole aperture, see Figure 4.11 (right) for a schematic representation of the event. Trapping experiments were performed on both UCNPs and nanoparticles doped with trace amounts of Er^{3+}. Similar to the rectangular apertures, trapping inside the double-nanohole apertures led to a strong enhancement of emitted Er^{3+} light. Using apertures with a 32 nm cusp width, an enhancement of 50 times the highest enhancement seen in rectangular apertures was measured in the emission, attributed to even higher electric field enhancement at the cusp.[23]

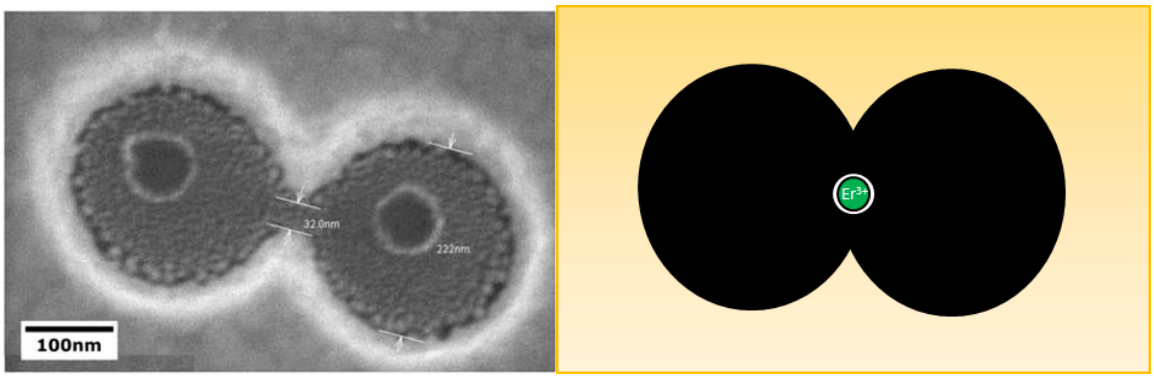

Figure 4.11: (left) SEM image of double nano-hole gold aperture. (right) schematic depiction of trapped $NaYF_4$ NP doped with single Er^{3+} ion.

An ensemble of $NaYF_4$ NPs with an average of 2.48 Er^{3+} ions per NP was investigated, made in the same fashion as the previously described $NaYF_4$ NPs with low dopant concentrations. Figure 4.12 shows emission spectra around 660 nm obtained upon 980 nm excitation. Similar to the results in the rectangular gold aperture, discrete emission levels at 660 nm could be observed. A deviation from the Poisson distribution was again observed. Fitting the observed discrete emission intensities to a Poisson distribution yields an average of 1.68 Er^{3+}.

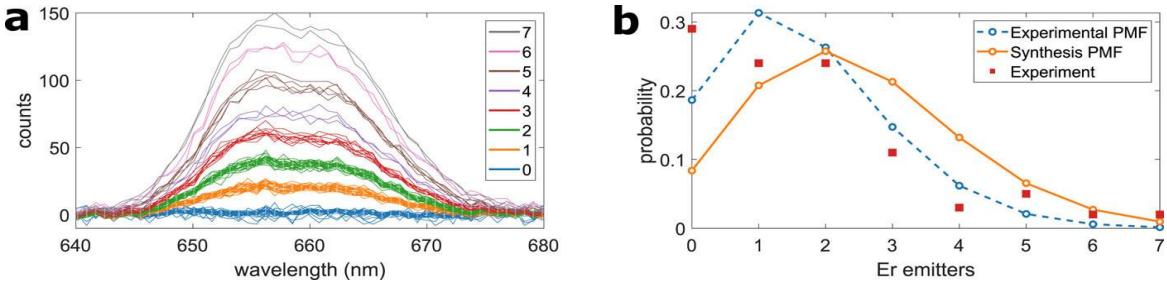

Figure 4.12: Measuring discrete emission levels from low counts of erbium emitters. (a) Emission counts from nanocrystals showing discrete levels corresponding to different amounts of active erbium emitters collected by a spectrometer with 1 s acquisition time. (b) Poisson probability mass functions (PMFs) for the experiment (λ = 1.68) and synthesis (λ = 2.48) and experimental probabilities for the number of Er^{3+} emitters.

The results in both rectangular and double nano-hole gold apertures appear highly promising to access singly doped Er^{3+} ions through trapping and selecting from a $NaYF_4$ NP ensemble doped with trace amounts of Er^{3+}. Left outstanding in these results is the true demonstration of single-photon emission from particles that were only inferred to have a single Er^{3+} ion from Poisson statistics of the discrete emission intensities. Anti-bunching of emitted photons needs to be verified using photon correlation measurements. Furthermore, in order to access single photons emitted from a device, the particles doped with a single Er^{3+} ion also need to be permanently anchored inside the apertures, so that they are still there after removal of the trapping beam and the solvent.

4.3 Conclusions

As a proposed strategy to access single Er^{3+} ions as single photon emitters on demand, dilutely doped $NaYF_4$:Er^{3+} NPs were trapped in gold nanoapertures, and their emitting ion concentration verified using photoluminescence spectroscopy. First, UCNPs doped with 18% Yb^{3+} and 2% Er^{3+} were synthesized using methods previously described. UCNPs were trapped in gold nano-apertures in 100 nm thick gold films. The aperture size was 100 nm wide and between 100 and 225 nm long. Particles were trapped in a 980 nm laser beam and trapping was verified by increase in transmitted 980 nm light, as well as the observation of Er^{3+} emission in the visible region upon 980 nm light excitation. The emission intensity was observed to be strongly enhanced compared to UCNPs in dispersion. The strongest emission enhancement was observed in nano-apertures with dimensions of ca. 100 nm x 208 nm, where the enhancement was about 400x. The strong enhancement was encouraging to measure emission of $NaYF_4$ NPs doped with on average 1 Er^{3+} ion. Three batches of dilutely doped nanoparticles were synthesized, with average Er^{3+} concentrations 0.006, 0.076, and 1.5 per nanoparticle. In the same way as the UCNPs, the dilutely doped particles were trapped optically in rectangular nano-holes with dimensions 100 nm x 208 nm. Emission was measured on a total of 100 individually trapped NPs. Discrete emission intensity levels could be observed. They were binned by intensity, and the amount of the particles per bin was compared with the discrete number of Er^{3+} ions per NP assumed by a Poisson distribution. The average number of Er^{3+} ions inferred by the discrete emission levels was lower than predicted, as a possible result of quenching the excited state by surface defects. The same demonstrations were done with a double nano-hole gold aperture, and again a close following of the Poisson distribution was observed in the

number of particles at each binned emission intensity. The results are highly promising for development of a single-photon emitter in the low-loss regime utilizing nanoparticles doped with a single Er^{3+} ion.

4.4 Experimental methods

Chemicals. Yttrium(III) chloride hexahydrate (99.99%), ytterbium(III) chloride hexahydrate (99.998%), erbium(III) chloride hexahydrate (99.995%), ammonium fluoride (99.99%), tech grade oleic acid (90%), tech grade 1-octadecene (ODE, 90%), and hexanes were purchased from Sigma-Aldrich. Anhydrous ethanol from Commercial Alcohols, methanol from Caledon, and sodium hydroxide from Bio Basic Canada inc. were used. All chemicals were used as received.

UCNP synthesis. To a 100 mL 3-neck round-bottom flask, 240.3 mg YCl_3•6(H_2O), 77.8 mg $YbCl_3$•6(H_2O) and 8.7 mg $ErCl_3$•6(H_2O) were added together with 15 mL 1-octadecene and 5 mL oleic acid. The mixture was heated to 160 °C under vacuum and kept at that temperature for 30 minutes before cooling to room temperature. Once cooled, a solution of 107 mg NaOH and 152 mg NH_4F in 10 mL MeOH was added dropwise while stirring. The mixture was heated to 65 °C 120 minutes to evaporate the MeOH. The temperature was then raised to 298 °C over 20 minutes (~12 °C/min.) Temperature was kept at 305-307 °C for 90 minutes. The mixture was then cooled, washed with 20 mL EtOH, centrifuged at 1800 g for 10 min, and washed with 30 mL EtOH again before redispersion in 20 mL hexanes. TEM and XRD were performed.

Erbium oleate synthesis. Erbium oleate was prepared by adding 1 mmol $ErCl_3$•6(H_2O) to 15 mL 1-octadecene and 6 mL oleic acid. The mixture was heated to 160 ºC under vacuum and kept at that temperature for 30 minutes before cooling to room temperature.

$NaYF_4$:Er^{3+} NPs (0.006 Er^{3+}/NP). In a 100 mL three-neck round-bottom flask, 1 mmol YCl_3•6(H_2O) and 1 mL 0.1 * 10^{-6} mM erbium oleate in 1-octadecene are added to 14 mL 1-octadecene and 6 mL oleic acid. The mixture was heated to 150 ºC under vacuum and kept at that temperature for 30 minutes before cooling to room temperature. Once cooled, a solution of 100 mg sodium hydroxide and 148 mg ammonium fluoride in 10 mL methanol was added dropwise while stirring. The mixture was heated to 70 ºC for 60 minutes to evaporate the methanol. The mixture was then put under a blanket of argon and the temperature was raised to 300 ºC over 15 minutes. The temperature was kept at 300 ºC for 60 minutes, briefly spiking to 319 ºC. The reaction mixture was then allowed to cool to room temperature, washed with 20 mL ethanol, centrifuged at 1,800 g for 10 min, and washed with 20 mL ethanol again before dispersing the particles in 20 mL hexane.

$NaYF_4$:Er^{3+} NPs (0.076 Er^{3+}/NP). In a 100 mL three-neck round-bottom flask, 1 mmol YCl_3•6(H_2O) and 20 μL 0.1 * 10^{-3} mM erbium oleate in 1-octadecene are added to 15 mL 1-octadecene and 6 mL oleic acid. The mixture was heated to 150 ºC under vacuum and kept at that temperature for 30 minutes before cooling to room temperature. Once cooled, a solution of 100 mg sodium hydroxide and 148 mg ammonium fluoride in 10 mL methanol was added dropwise while stirring. The mixture was heated to 70 ºC for 60 minutes to evaporate the methanol. The mixture was then put under a blanket of argon and the

temperature was raised to 300 ºC over 15 minutes. The temperature was kept at 300 ºC for 60 minutes. The reaction mixture was then allowed to cool to room temperature, before washing with 20 mL ethanol, centrifuging at 1,800 g for 10 min, and washing with 20 mL ethanol again before dispersing the particles in 20 mL hexane.

$NaYF_4$:Er^{3+} NPs (1.5 Er^{3+}/NP). In a 100 mL three-neck round-bottom flask, 1 mmol YCl_3•6(H_2O) and 200 μL 0.1 * 10^{-3} mM erbium oleate in 1-octadecene are added to 15 mL 1-octadecene and 6 mL oleic acid. The mixture was heated to 150 ºC under vacuum and kept at that temperature for 30 minutes before cooling to room temperature. Once cooled, a solution of 100 mg sodium hydroxide and 148 mg ammonium fluoride in 10 mL methanol was added dropwise while stirring. The mixture was heated to 70 ºC for 60 minutes to evaporate the methanol. The mixture was then put under a blanket of argon and the temperature was raised to 300 ºC over 15 minutes. The temperature was kept at 300 ºC for 60 minutes. The reaction mixture was then allowed to cool to room temperature, washed with 20 mL ethanol, centrifuged at 1,800 g for 10 min, and washed with 20 mL ethanol again before dispersing the particles in 20 mL hexane.

$NaYF_4$:Er^{3+} NPs (2.48 Er^{3+}/NP). To a 100 mL 3-neck round-bottom flask, 300 mg YCl_3•6(H_2O) and 0.3 mL 0.1 *10^{-3} mM erbium oleate were added together with 16 mL 1-octadecene and 5 mL oleic acid. The mixture was heated to 140 ºC under vacuum and kept at that temperature for 60 minutes before cooling to room temperature. Once cooled, a solution of 102 mg NaOH and 150 mg NH4F in 10 mL MeOH was added dropwise while stirring. The mixture was heated to 70 ºC 120 minutes to evaporate the MeOH. The mixture

was then put under a blanket of argon and the temperature was raised to 299 ºC. Temperature was kept at 299 ºC for 120 minutes. The mixture was then allowed to cool to room temperature, washed with 20 mL EtOH, centrifuged at 1,800 g for 10 min, and washed with 30 mL EtOH again before redispersion in 20 mL hexanes. TEM and XRD were performed.

Nanoparticle characterization. Transmission electron microscopy images were obtained using a JEOL JEM-1400 microscope operating at 80 kV. Hexane dispersions of the NPs were drop-cast on a Formvar carbon-coated grid (300 mesh Cu) and air-dried for 5 min. before imaging. Size analysis of NCs from the images was performed by measuring the surface area of at least 1,000 particles and calculating the corresponding diameter. X-ray diffractograms with a resolution of 0.0263 º2θ were collected using a PANalytical Empyrean X-ray System with a Cu source (Kα radiation, λ = 1.54060 Å) operating at 45 kV and 40 mA.

Visible light luminescence emission spectroscopy. Emission spectroscopy was performed on up-converting nanoparticles exciting with a JDS Uniphase 980 nm pump laser diode operating at 1.6 W. The diode was coupled to an optical fiber and the emission of the fiber tip collimated to 1 mm^2 using a Newport F-91-C1-T multimode fiber coupler, where the resulting photon flux is estimated to be around 150 W/cm^2. The emission was measured and corrected for instrument response using a cooled Hamamatsu R928P PMT between 350 and 750 nm. Counts were integrated for 1 s at every 1 nm step using a 1 nm slit width. A 900 nm short-pass filter was placed between the sample and the detector.

IR luminescence emission spectroscopy. Infrared emission spectroscopy was performed using a JDS uniphase 980 nm pump laser diode operating at 1.6 W on $NaYF_4$ NPs in hexanes with 1.5 Er/UCNC in a 1 × 1 × 3.5 cm quartz cuvette. The diode was coupled to an optical fiber and emission of the fiber tip collimated to 1 mm^2 using a Newport F-91-C1-T multimode fiber coupler. The photon flux is estimated to be around 150 W/cm^2. The emission was measured and corrected for instrument response using a liquid-nitrogen cooled (-80 °C) Hamamatsu R5509 NIR PMT between 1,450 nm and 1,650 nm. Counts were integrated for 0.5 s at every 0.5 nm step using a 3 nm slit width over 40 subsequent scans, for a total measuring time of 8,000 seconds. A 1025 nm long-pass filter was placed between the sample and the detector. The experiment was repeated for hexane under the same conditions.

Rectangular gold aperture fabrication. The rectangular apertures were fabricated by focused ion beam milling (Hitachi FB-2100) of a commercially available slide with a 100 nm gold layer on a glass substrate (EMF Corp.) and a 5 nm Ti adhesion layer.

Double nano-hole gold aperture fabrication. Colloidal lithography was used to fabricate double nanohole apertures. Microscope slides were cleaned using plasma for 15 min and sonicated for 10 min in an ethanol bath. 30 L of 300 nm 0.01% w/v polystyrene spheres in ethanol drop-coated on the microscope slides uniformly. While the solution dries out through evaporation, the polystyrene spheres attach to the slides. The prepared slides were plasma etched with 5-15 s difference in etching time to get different cusp separations on each sample. Using 5 nm of titanium as an adhesive layer followed by 70 nm of gold,

the samples were sputtered (MANTIS sputtering system). The sputtered samples were sonicated for 1 min in a toluene bath to remove polystyrene beads. SEM was performed.

Optical trapping in rectangular gold apertures. A continuous-wave 980 nm single-beam laser was filtered (780 nm long-pass filter), collimated, expanded, and focused onto the sample using a 100× oil immersion microscope objective (1.25 numerical aperture). This beam serves both as trapping beam and the excitation source for UCNCs. A 10× condenser microscopic objective (0.25 numerical aperture) was used to collect the transmitted signal through the rectangle aperture and was measured by a silicon-based avalanche photodetector (Thorlabs APD110A). A piezoelectric controlled three-axis sample stage was used to aligned the beam through the rectangle apertures with 20 nm positioning precision. A half-wave plate (HWP) and linear polarizer (LP) were used to orient the polarization of the pump beam with respect to the nano-aperture. Measurements were obtained after altering the HWP and LP orientation to obtain the highest transmission of laser beam through the aperture (the incident laser was made to be always linearly polarized along the short axes of the aperture). A 750 nm short-pass filter (Thorlabs FES0750) and a 500–700 nm band-pass filter were used on the spectrometer to minimize the trapping beam intensity. The luminescence spectrum was measured using a QE65000 Ocean Optics spectrometer for 30 s integration time. All 500 up-conversion measurements for three different batches were conducted using 39 mW focused on approximately 1 μm^2. The rectangular aperture gold samples were attached to coverslips with a free spacer containing 10 μL of UCNPs with a concentration of 2×10^{10} particles/cm^3 in hexane.

Optical trapping in double nano-hole gold apertures. The optical tweezer setup consists of a single 980 nm continuous-wave laser (JDS Uniphase SDLO-27-7552-160-LD), which is collimated, filtered, polarized, and expanded before being focused on the sample with a 100× oil immersion microscope objective (1.25 numerical aperture). This single beam is used for both trapping and to excite the nanocrystals. A 10× microscope objective is used to collect the light transmitted through the sample, which is measured by an avalanche photodetector (Thorlabs APD120A). The polarization of the beam is set by the half-wave plate (HWP) and the linear polarizer (LP). A three-axis sample stage with piezoelectric adjustment aligns the apertures to the beam with 20 nm precision. A 750 nm short-pass filter (Thorlabs FES0750) reduces the trapping beam intensity, and a bifurcated fiber splits the signal between two spectrometers, one for visible wavelengths (Ocean Optics QE65000) and one for near-infrared (NIR) wavelengths (BaySpec NIRS-0900-1700). The gold DNH aperture samples were attached to #0 coverslips with an adhesive spacer containing 17.6 μL of nanocrystals in hexane with concentrations of 1.3×10^{12}, 5×10^{12}, and 4×10^{12} nanoparticles/cm^3 for the 16.9, 22.7, and 26.2 nm nanocrystals.

4.5 References

1. Gisin, N., How Far Can One Send a Photon? *Front. Phys.* **2015,** *10*, 1-8.
2. Monroe, C.; Raussendorf, R.; Ruthven, A.; Brown, K.; Maunz, P.; Duan, L.-M.; Kim, J., Large-Scale Modular Quantum-Computer Architecture with Atomic Memory and Photonic Interconnects. *Phys. Rev. A* **2014,** *89*, 022317.
3. Eisaman, M. D.; Fan, J.; Migdall, A.; Polyakov, S. V., Invited Review Article: Single-Photon Sources and Detectors. *Rev. Sci. Instrum.* **2011,** *82*, 071101.
4. Balasubramanian, G.; Lazariev, A.; Arumugam, S. R.; Duan, D.-w., Nitrogen-Vacancy Color Center in Diamond—Emerging Nanoscale Applications in Bioimaging and Biosensing. *Curr. Opin. Chem. Biol.* **2014,** *20*, 69-77.
5. Neumann, P.; Kolesov, R.; Jacques, V.; Beck, J.; Tisler, J.; Batalov, A.; Rogers, L.; Manson, N.; Balasubramanian, G.; Jelezko, F., Excited-State Spectroscopy of Single NV Defects in Diamond Using Optically Detected Magnetic Resonance. *New J. Phys.* **2009,** *11*, 013017.
6. Meijer, J.; Burchard, B.; Domhan, M.; Wittmann, C.; Gaebel, T.; Popa, I.; Jelezko, F.; Wrachtrup, J., Generation of Single Color Centers by Focused Nitrogen Implantation. *Appl. Phys. Lett.* **2005,** *87*, 261909.
7. Arakawa, Y.; Holmes, M. J., Progress in Quantum-Dot Single Photon Sources for Quantum Information Technologies: A Broad Spectrum Overview. *Appl. Phys. Rev.* **2020,** *7*, 021309.
8. Zwiller, V.; Blom, H.; Jonsson, P.; Panev, N.; Jeppesen, S.; Tsegaye, T.; Goobar, E.; Pistol, M.-E.; Samuelson, L.; Björk, G., Single Quantum Dots Emit Single

Photons at a Time: Antibunching Experiments. *Appl. Phys. Lett.* **2001,** *78*, 2476-2478.

9. De Greve, K.; Yu, L.; McMahon, P. L.; Pelc, J. S.; Natarajan, C. M.; Kim, N. Y.; Abe, E.; Maier, S.; Schneider, C.; Kamp, M., Quantum-Dot Spin–Photon Entanglement Via Frequency Downconversion to Telecom Wavelength. *Nature* **2012,** *491*, 421-425.
10. Efros, A. L.; Nesbitt, D. J., Origin and Control of Blinking in Quantum Dots. *Nat. Nanotechnol.* **2016,** *11*, 661-671.
11. Mahler, B.; Spinicelli, P.; Buil, S.; Quelin, X.; Hermier, J.-P.; Dubertret, B., Towards Non-Blinking Colloidal Quantum Dots. *Nat. Mater.* **2008,** *7*, 659-664.
12. Yuan, G.; Gomez, D. E.; Kirkwood, N.; Boldt, K.; Mulvaney, P., Two Mechanisms Determine Quantum Dot Blinking. *ACS Nano* **2018,** *12*, 3397-3405.
13. Giles, C. R.; Desurvire, E., Propagation of Signal and Noise in Concatenated Erbium-Doped Fiber Optical Amplifiers. *J. Lightwave Technol.* **1991,** *9*, 147-154.
14. Dibos, A.; Raha, M.; Phenicie, C.; Thompson, J. D., Atomic Source of Single Photons in the Telecom Band. *Phys. Rev. Lett.* **2018,** *120*, 243601.
15. Reisfeld, R., Optical Properties of Lanthanides in Condensed Phase, Theory and Applications. *AIMS Mater. Sci.* **2015,** *2*, 37-60.
16. Shariatdoust, M. S.; Frencken, A. L.; Khademi, A.; Alizadehkhaledi, A.; van Veggel, F. C. J. M.; Gordon, R., Harvesting Dual-Wavelength Excitation with Plasmon-Enhanced Emission from Upconverting Nanoparticles. *ACS Photonics* **2018,** *5*, 3507-3512.

17. Rohani, S.; Quintanilla, M.; Tuccio, S.; De Angelis, F.; Cantelar, E.; Govorov, A. O.; Razzari, L.; Vetrone, F., Enhanced Luminescence, Collective Heating, and Nanothermometry in an Ensemble System Composed of Lanthanide-Doped Upconverting Nanoparticles and Gold Nanorods. *Adv. Opt. Mater.* **2015,** *3*, 1606-1613.

18. Saboktakin, M.; Ye, X.; Chettiar, U. K.; Engheta, N.; Murray, C. B.; Kagan, C. R., Plasmonic Enhancement of Nanophosphor Upconversion Luminescence in Au Nanohole Arrays. *ACS Nano* **2013,** *7*, 7186-7192.

19. Kotnala, A.; Gordon, R., Quantification of High-Efficiency Trapping of Nanoparticles in a Double Nanohole Optical Tweezer. *Nano Lett.* **2014,** *14*, 853-856.

20. Al Balushi, A. A.; Kotnala, A.; Wheaton, S.; Gelfand, R. M.; Rajashekara, Y.; Gordon, R., Label-Free Free-Solution Nanoaperture Optical Tweezers for Single Molecule Protein Studies. *Analyst* **2015,** *140*, 4760-4778.

21. Ashkin, A., Atomic-Beam Deflection by Resonance-Radiation Pressure. *Phys. Rev. Lett.* **1970,** *25*, 1321.

22. Ashkin, A.; Dziedzic, J. M.; Bjorkholm, J. E.; Chu, S., Observation of a Single-Beam Gradient Force Optical Trap for Dielectric Particles. *Opt. Lett.* **1986,** *11*, 288-290.

23. Sharifi, Z.; Dobinson, M.; Hajisalem, G.; Shariatdoust, M. S.; Frencken, A. L.; van Veggel, F. C. J. M.; Gordon, R., Isolating and Enhancing Single-Photon Emitters for 1550 nm Quantum Light Sources Using Double Nanohole Optical Tweezers. *J. Chem. Phys.* **2021,** *154*, 184204.

24. Li, Z.; Zhang, Y., An Efficient and User-Friendly Method for the Synthesis of Hexagonal-Phase $NaYF_4$: Yb, Er/Tm Nanocrystals with Controllable Shape and Upconversion Fluorescence. *Nanotechnology* **2008,** *19*, 345606.

25. Alizadehkhaledi, A.; Frencken, A. L.; Dezfouli, M. K.; Hughes, S.; van Veggel, F. C. J. M.; Gordon, R., Cascaded Plasmon-Enhanced Emission from a Single Upconverting Nanocrystal. *ACS Photonics* **2019,** *6*, 1125-1131.

26. Haight, F. A. *Handbook of the Poisson Distribution*; 1967.

Chapter 5: A Potentially Scalable Photochemical Anchoring Method to Isolate Nano-Particles Doped with a Single Er^{3+} Ion for Quantum Light Sources in the Telecom Window

Based on:

Frencken, A. L.; Dobinson, M.; Sharifi, Z; Toodeshki, E. H.; Gordon, R.; van Veggel, F. C. J. M., Photochemical Anchoring of Singly Er^{3+} Ion-Doped $NaYF_4$ Nanoparticles for Scalable Fabrication of Single-Photon Emitting Devices: Implications for Quantum Light Sources in the Telecom Window. *ACS Appl. Nano Mater.* 2023, *in press.*

Trapping and anchoring experiments were performed by Michael Dobinson (UVic). The experimental section detailing the trapping and anchoring experiments was provided by Michael Dobinson (UVic).

Abstract

Scalable methods to access single-photon sources on demand are highly sought after. As a potential strategy, the optical trapping and chemical anchoring of $NaYF_4$ nanoparticles (NPs) and $NaYF_4$ NPs doped with on average a single Er^{3+} ion is demonstrated. The anchoring method we present involves surface coating the NPs with thiol-functionalized phospholipids, where the thiol group is protected with a chemical group photo-removable at 340 nm 2-bromo-4'-hydroxyacetophenone. Functionalized NPs are trapped optically in a gold double-nanohole aperture using a 980 nm laser. A 340 nm light beam is focused on the particle, resulting in de-protection of the thiol groups and attachment of the thiols to the gold surface, permanently anchoring the nanoparticles. Electron microscopic imaging proves the successful anchoring after removal of the trapping laser, 340 nm light source, and solvent. The approach is promising for reliably fabricating a single-photon emitting material in a scalable and potentially automatable manner.

5.1 Introduction

Recent decennia have seen an explosive growth in the field of quantum-information science.[1-2] The field is involved with the encoding, computation, and transfer of information using quantum states. Research in this field is motivated by the exciting promise that computation using quantum states can vastly exceed the limits of classical computation, and information can be transferred with unconditional security.[3] An auspicious candidate to perform these tasks is the photonic qubit, where quantum information is stored and transferred in states of a single photon, and researchers of various disciplines are working to develop a scalable method to access reliably single photons on demand.[4-6]

Single Er^{3+} ions are highly promising sources of single photons, because they can emit light stably at 1,550 nm,[7] which is where the low-loss regime of optical fibers lies.[6, 8] This is in contrast to various other sources of single photons that are under investigation, such as visible light emitting quantum dots[8] and nitrogen-vacancy (NV) color centers in diamond.[9] These approaches predominantly lead to photons with wavelengths below 1,000 nm, where losses in optical fibers are much higher.[4] Research efforts have been made to tune the wavelength of single-photon sources to 1,550 nm by using non-linear crystals,[8] but by accessing 1,550 nm light directly using Er^{3+} ions, these steps can be avoided altogether.[10]

Developing a material that utilizes single Er^{3+} ions as a single-photon source deterministically and scaling it up to have several sources of a single photon on demand

comes with a variety of imposing challenges. The emission intensity of a single lanthanide ion is typically extremely low as a result of the forbidden nature of the intra-4f transitions.[7] Furthermore, to isolate a single-photon source, the Er^{3+} ion has to be separated well from any other light emitting sources, which can be difficult due to the ions inside Er^{3+} host materials being typically randomly distributed, potentially leading to more than a single Er^{3+} ion emitting in the same spot.

Other groups have explored strategies to overcome these challenges previously to access single rare-earth emitters. Most efforts relied on finding single rare-earth ions in crystals that are doped randomly at low dopant levels.[4, 11-12] In these works single emitters were found by scanning the surface of these crystals optically, demonstrating single-photon emission through anti-bunching in the second order autocorrelation function of the photoluminescence. While single emitters could be isolated and their emission measured, a scalable method to fabricate these emitters deterministically was still outstanding. A strategy to isolate single erbium ions in a deterministic way reported by Schmidt-Kaler *et al.* is controlled implementation of a single ion on a crystallographic surface, using a pulsed laser to trap Pr^{3+} ions from an ion beam.[13] While this method does look to be promising for scalability, the results reported by the authors still show a random distribution in the number of active emitters at the desired location.

Previous efforts have shown strategies to access reliably single Er^{3+} ions, utilizing a plasmonic tweezer nano-hole system to isolate nanoparticles doped with a single Er^{3+} ion.[14-15] The plasmonic nano-hole system served two important roles. Firstly, the

interaction of the surface plasmon generated in the nano-structured gold results in strong enhancement of the local electric field, yielding enhanced emission rates of the Er^{3+} ions. Emission intensity enhancements of around 10^3 times were observed.[14-16] Secondly, the tweezer system allows for trapping single nanoparticles,[17] allowing for the selection of singly doped particles. The selective trapping is important as it was found that in nanoparticles that were doped with around one single Er^{3+} ion on average, the ions showed a statistical distribution over the ensemble, closely following Poisson statistics. The result of this is that only ca. 35% of the nanoparticles contained a single Er^{3+} ion, with the other two dominant fractions being undoped and doubly doped nanoparticles.[14-15]

One of the problems left outstanding in previous demonstrations was scaling up the methods to produce several single-photon sources in a potentially automatable process. Particles were trapped and emission was measured, but would diffuse back into solution after the optical trap was removed. To scale up the process and develop a method to access single-photon emitters in the absence of an optical trap, the particles need to be anchored into the plasmonic nano-holes.

Here, a simple, scalable photochemical method to anchor trapped particles onto the gold surface of the plasmonic double nano-holes is presented. The strategy involves capping the nanoparticles with thiol-functionalized phospholipids, where the thiol was protected with a photo-removable group. These particles were then trapped using double nano-hole optical tweezers, and anchored by deprotection of the thiol group by UV light absorption, allowing the sulfur to coordinate strongly to the gold surface.[18]

5.2 Results and discussion

Pure $NaYF_4$ and $NaYF_4$ nanoparticles doped with on average 1.72 Er/NP and 2.48 Er/NP were synthesized using colloidal methods as described in previous work.[19-20] Briefly, the synthesis involves heating lanthanide chloride precursors in the presence of oleic acid under vacuum at 140 ^oC, followed by introduction of NaOH and NH_4F and heating to 300 ^oC. Successful synthesis was verified by TEM analysis, see Figure 5.1 (a) and (b). The diameter of the $NaYF_4$ NPs was 32.9 ± 1.4 nm (Figure 5.1 (c)), and that of the $NaYF_4$ doped with 1.72 Er/NP was 23.0 ± 1.2 nm (Figure 5.1 (d)). Particles in this size range have been successfully trapped in gold double-hole nano-apertures previously.[15] From the size and ratio Er/Y in the synthesis, the distribution of Er^{3+} ions in the ensemble was calculated assuming Poisson statistics,[21] see Figure 5.1 (e).

In previously reported demonstrations, it was inferred that $NaYF_4$ NPs doped with trace amounts of Er^{3+} can be potential single-photon sources at 1,550 nm, after observation of discrete intensities of the characteristic Er^{3+} emission lines in the visible region (through up-conversion).[14-15] In Appendix II, discrete emission intensities at 1,550 nm of $NaYF_4$ doped with trace amounts of Er^{3+} ions are shown. The characteristic emission of the $^4I_{13/2} - {}^4I_{15/2}$ transition is observed at six distinct emission intensity levels, with intensities consistently around 100 counts apart, indicating a discrete number of emitters. Of all particles probed, 23% showed no emission, and 34% showed an emission intensity of ca. 100 counts. The lowest discrete level of emission intensities is expected to correspond with a single emitting Er^{3+} ion, and thus, 34% of the NPs in this ensemble is predicted to be an active single-photon emitter in the low-loss wavelength regime. The number of emitting

Er^{3+} ions per NP was observed to be lower than the number predicted from the amount added during synthesis, assuming Poisson statistics. This is similar to what was previously observed measuring discrete emission levels in the visible region following up-conversion, and likely the result of emission quenching of Er^{3+} ions close the NP surface,.[14-15] Furthermore, non-statistical distributions of dopant ions in lanthanide-based nanoparticles have been reported as well, which could also contribute to deviation from a Poisson distribution of emitters.[22-23]

For the surface functionalization of the NPs with thiols, oleate-capped particles were encapsulated with DSPE-mPEG and DSPE-PEG-SH (in a 1:10 mole ratio) via a dual solvent exchange method. The successful encapsulation was inferred from the successful water transfer, because oleate-capped particles would not be dispersible in water.[24]

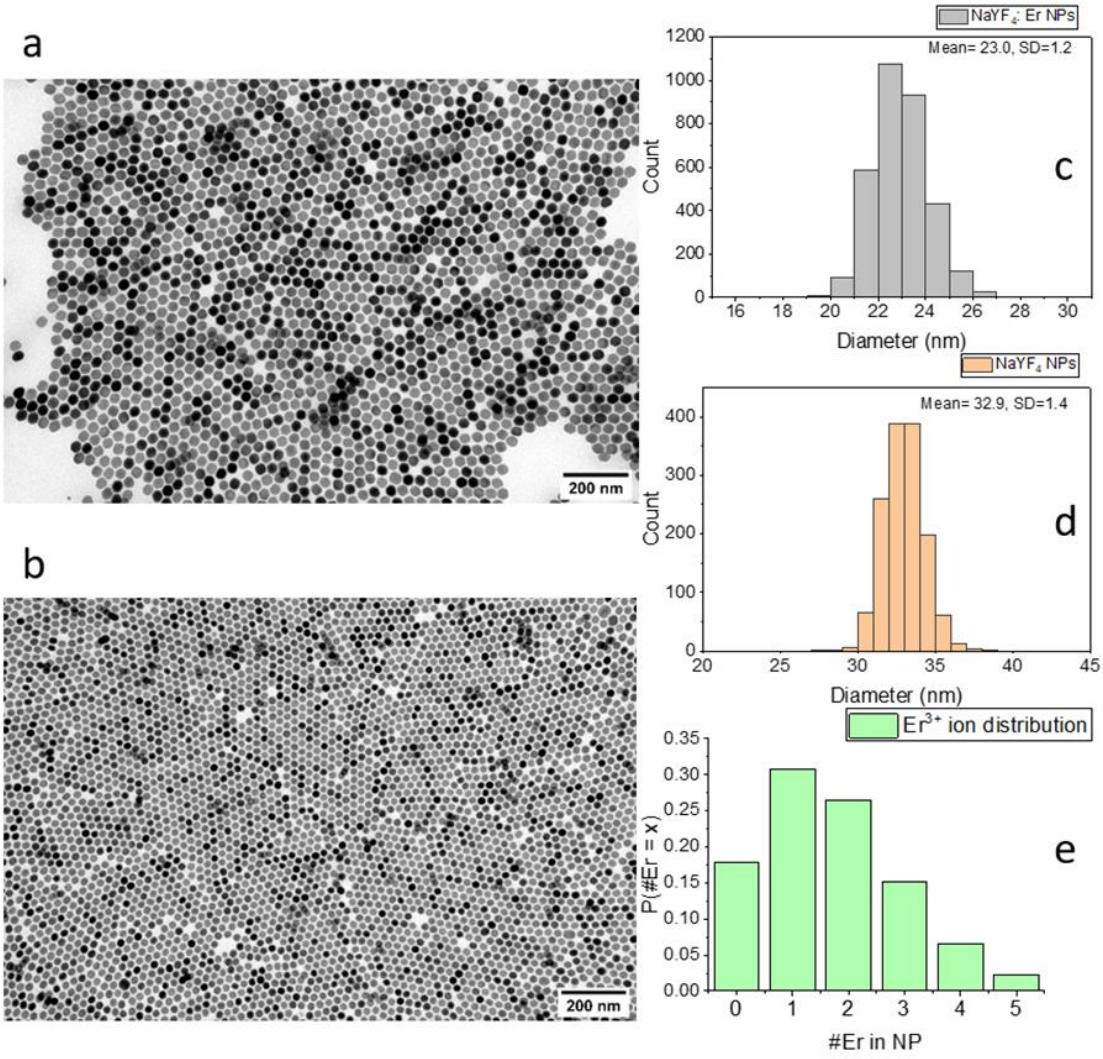

Figure 5.1: TEM image of $NaYF_4$ NPs (a) and $NaYF_4$:Er NPs (b) at 100k magnification), histograms of NP diameter are shown correspondingly in (c) and (d). (e) Shows the expected distribution of Er^{3+} ions in the doped ensemble.

After transfer to water with DSPE-mPEG and DSPE-PEG-SH, a photo-removable capping molecule was introduced into the dispersion. 2-Bromo-4'-hydroxyacetophenone was chosen as the photo-removable group, based on the successful demonstration of photo-removal by Pei *et al*.[25] The overall reaction pathway to fabricate NPs functionalized with photo-protected thiol groups is shown in Figure 5.2.

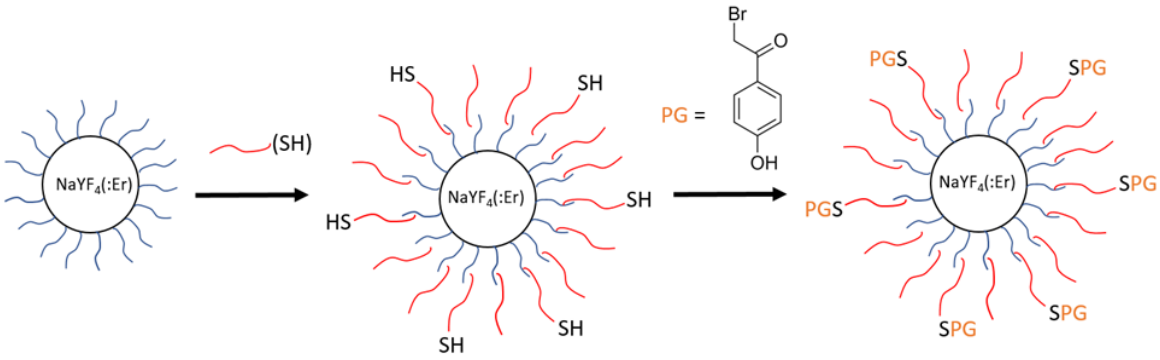

Figure 5.2: Schematic representation of capping NPs with thiol-functionalized phospholipids (in a 1:10 ratio to methoxy-functionalized phospholipids, not displayed to ratio in figure), followed by thiol protection with photo-removable group (PG) bromo-4'-hydroxyacetophenone.

An experiment to verify the efficacy of sulfur group exposure was conducted. The effect was demonstrated by introducing a thiol-detecting group from a commercial thiol-detection kit. The detection kit works by using a molecule that turns on as an emitter upon reaction with a thiol group. After reaction with a sulfur group, the molecule emits light at 520 nm upon 490 nm excitation.

The thiol-detection group (TDG) was introduced into a dispersion of $NaYF_4$ NPs functionalized with photo-protected sulfur groups. Emission upon 490 nm excitation was measured before the dispersion was exposed to 350 nm light for 15 minutes, and emission upon 490 nm excitation was measured again. Figure 5.3 (top) shows the emission spectra before and after 350 nm light exposure. A strong increase is observed upon the UV light exposure, attributed to reaction of the TDG with the exposed thiols. This demonstrates the successful use of the photo-protecting group to cap thiol groups on the NPs, and demonstrates that the group can be removed by 350 nm light exposure.

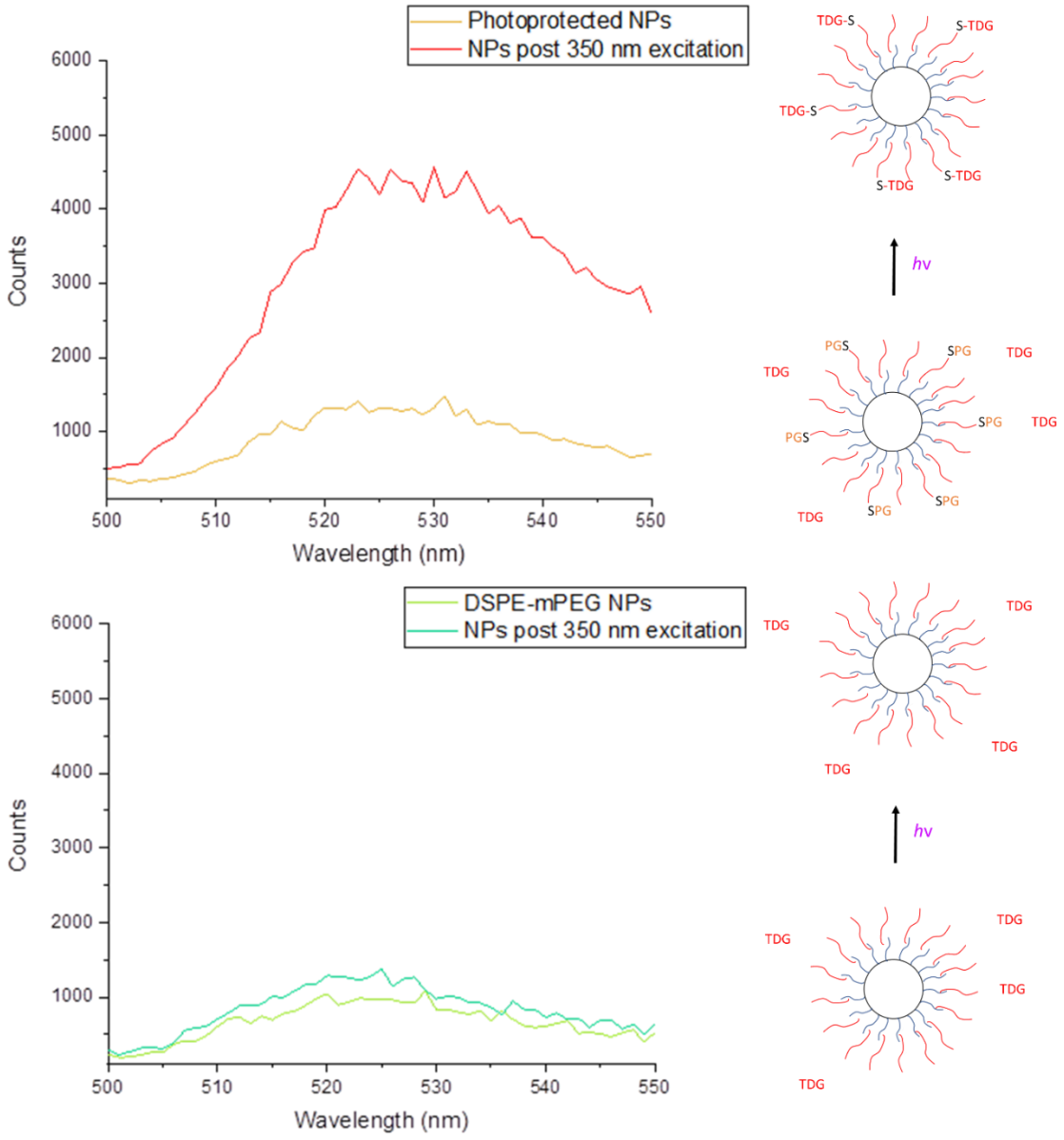

Figure 5.3: Top: Emission measured of thiol-detecting group (TDG) in the presence of thiol-functionalized NPs with photo-protecting group at 490 nm excitation, before (yellow) and after (red) 350 nm irradiation for 15 minutes. Bottom: Emission measured of thiol-detecting group (TDG) in the presence of phospholipid coated NPs at 490 nm excitation, before (yellow) and after (green) 350 nm irradiation for 15 minutes.

As a control, the same experiment was performed on $NaYF_4$ NPs capped with only DSPE-mPEG, see Figure 5.3 (bottom). Emission in the presence of the TDG was measured upon 490 nm excitation, and again after 15-minute exposure to 350 nm light. When no photo-protected sulfur groups were present, no increase in emission was observed. Some background signal remained in unbound thiol-detection groups, at 1,000 counts, as seen before 350 nm exposure in the experiment with the protected thiol groups. This effect has been seen in literature for unbound luminescent thiol probe molecules.[26] The interpretation of this background luminescence is that unbound thiol-detecting groups convert in small amounts to their luminescent form in solution, forming an equilibrium. This mechanism is shown in Appendix II. Thiol-detecting probe molecules are widely reported to be weakly luminescent before binding to a thiol group.[27]

NPs functionalized with photo-protected sulfur were trapped optically in gold double-nanohole apertures using a 980 nm laser. The transmission of the laser through the aperture was measured and used to confirm trapping by the amplitude increase when a NP was trapped. When successful trapping was verified, a 340 nm light source was used to irradiate them, exposing the sulfur groups, allowing them to coordinate the gold surface, thereby anchoring them. Successful anchoring was demonstrated using scanning electron microscopy (SEM). Figure 5.4 shows a demonstration of the anchoring process. The electron micrographs show gold double-nanohole apertures before the anchoring event, and after the anchoring event, leaving a single nanoparticle in the hole, encircled in yellow in Figure 5.4. A residue leftover from the polystyrene beads used in the nanohole fabrication is seen inside the holes. The bottom of the figure provides a schematic

representation of the anchoring event. Reproducibility of successful trapping was confirmed by repetition of the experiment, see Appendix II.

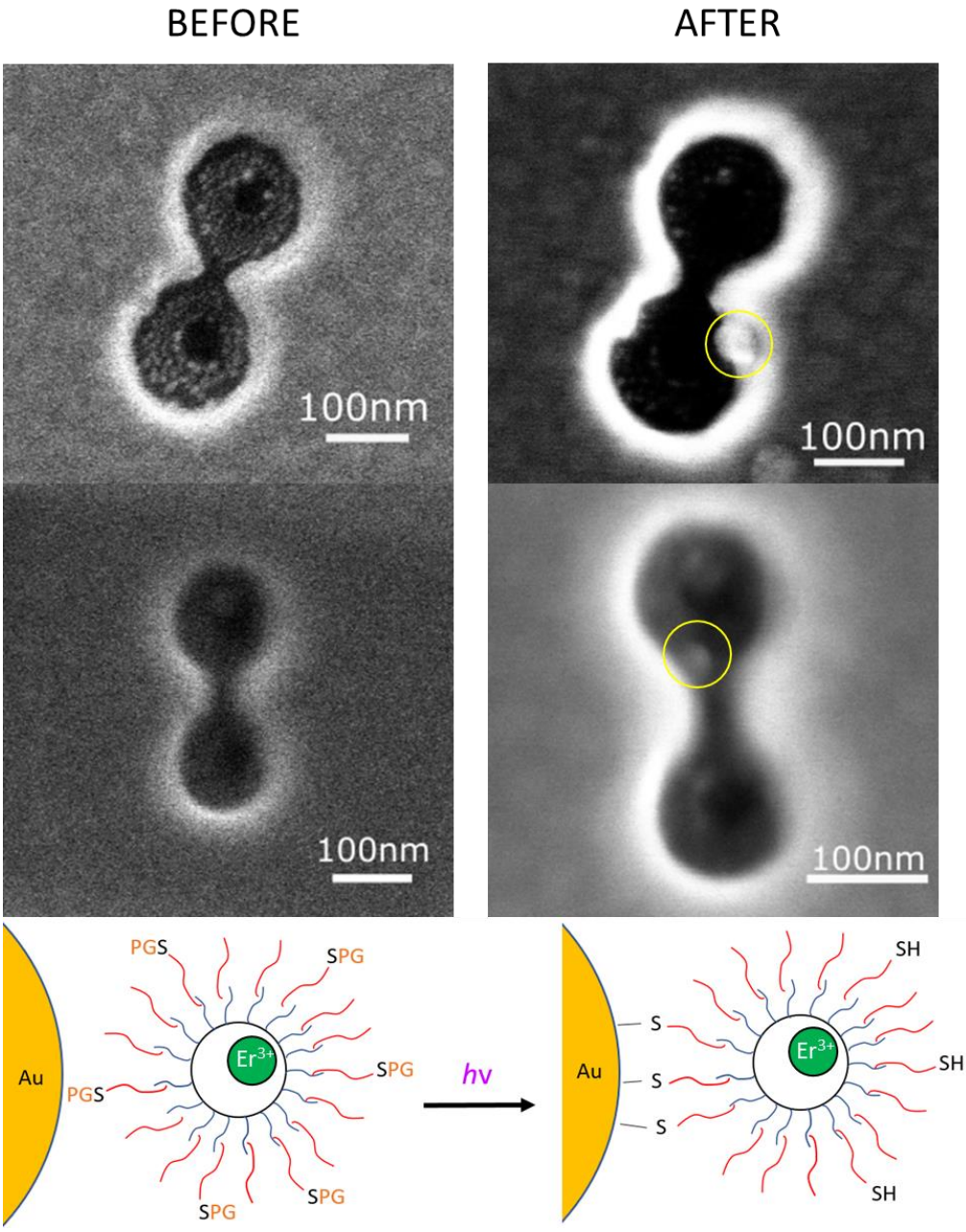

Figure 5.4: SEM images of double nano-hole (left), and SEM images of double nano-hole with particle immobilized (right). The particle is encircled in yellow. A schematic representation of the anchoring event on a singly doped NP is shown to demonstrate the process. The Er^{3+} ion is shown in green.

The successful anchoring of singular nanoparticles is highly promising for large-scale production of single-photon emitters. Furthermore, the unique anchoring method presented in this chapter can be utilised as a tool for a variety of other material fabrication needs. The surface functionalization method may be employed on any surface modified nanomaterial. The photo-triggered anchoring of nanoparticles on surfaces can be used as a coating method to coat large surfaces with functionalized nanoparticles. Selective focusing of light may be used to attach functionalized particles locally to specific areas on a surface.

For use in the anchoring of $NaYF_4$ NPs doped with a single erbium ion to access single-photon emitters, the process demonstrated in this chapter might in principle be fully automatable as well. An automated system could be designed where a nanohole aperture grid is immersed in a dispersion of NPs, and upon detection of single erbium emission in a specific nanohole, a UV light can be focused to anchor the NP. This can then be repeated for as many apertures as desired.

5.3 Conclusions

In summary, a demonstration to trap photo-chemically select (potentially single-photon emitting) nanoparticles in plasmonic apertures was presented. Pure $NaYF_4$ and $NaYF_4$ doped with trace amounts of Er^{3+} designed for single-photon emission were synthesized. The particles were coated with sulfur-functionalized phospholipids that were subsequently capped with photo-removable groups. Successful protection by the chemical group was demonstrated by introduction of a photo-luminescent thiol-detection agent. Exposure to 340 nm radiation resulted in reaction of the sulfur groups with the thiol-detection agent,

indicating successful photo-induced deprotection. A demonstration of immobilization inside double-nanohole apertures in gold was given by trapping the surface-modified particles inside the apertures optically and illumining with 340 nm light. Comparison of the nano-hole before and after the anchoring event revealed the presence of an anchored nanoparticle. The results are highly promising to fabricate gold nanoaperture enhanced single-photon emitters in a scalable manner, that is potentially automatable as well. Furthermore, the surface functionalization method presented opens up access to a variety of new materials.

5.4 Experimental methods

***Chemicals*.** Yttrium(III) chloride hexahydrate (99.99%), erbium(III) chloride hexahydrate (99.995%), ammonium fluoride (99.99%), dimethyl sulfoxide (DMSO), tech grade oleic acid (90%), tech grade 1-octadecene (ODE, 90%), hexanes, and toluene were purchased from Sigma-Aldrich. Anhydrous ethanol from Commercial Alcohols, methanol from Caledon, and sodium hydroxide from Bio Basic Canada Inc. were used. 1,2-distearoyl-*sn*-glycero-3-phosphoethanolamine-*N*-[methoxy(polyethylene glycol)-2000 (DSPE-mPEG) was bought from Avanti, and 1,2-distearoyl-*sn*-glycero-3-phosphoethanolamine-*N*-(polyethylene glycol)-thiol-2000 (DSPE-PEG-SH) from Nanosoft Polymers. 2-bromo-4'-hydroxyacetophenone and the commercial photodetection kit including phosphate buffer solution (PBS) were bought from Sigma-Aldrich. All chemicals were used as received.

Nanoparticle synthesis. For the $NaYF_4$ NP synthesis, 1 mmol YCl_3•6(H_2O) was weighed and introduced into a 100 mL three neck round-bottom flask. 15 mL 1-Octadecene and 6

mL oleic acid were added. The mixture was stirred at a moderate pace, but low enough that the surface of the liquid remained level. This was then heated with a heating mantle to 140 °C over 30 minutes under vacuum, and kept at that temperature for 1 hour. The mixture turned clear and slightly yellow. This was cooled to 60 °C over 15 minutes and a solution of 10 mL methanol with 2.5 mmol NaOH and 4 mmol NH_4F was introduced drop-wise. The resulting mixture was heated at 70 °C until methanol had evaporated, which was after ca. 30 min. The mixture was then heated to 300 °C over 15 min. The temperature was kept at 300 °C for 90 minutes before the heating mantle was removed and the mixture was allowed to cool to room temperature. This was then added to 30 mL ethanol in a centrifugation tube and centrifuged at 3,000 g for 10 min. The resulting supernatant was discarded, and the pellet at the bottom was re-dispersed in 20 mL toluene.

For the $NaYF_4$ NPs doped with trace amounts of Er^{3+}, the synthesis was identical except for the addition of an extra 0.2 mL 0.1 * 10^{-3} M Er oleate in ODE at the first step.

Nanoparticle characterization. Transmission electron microscopy images were collected using a JEOL JEM-1400 microscope operating at 80 kV. Dispersions of the NPs in hexane were drop-cast on a formvar carbon-coated grid (300 mesh Cu) and air-dried over about 1 minute before imaging. Size analysis of NCs from the images was performed digitally by measuring the surface area of at least 1,000 particles with the program ImageJ (version 1.52p) and calculating the corresponding diameter.

***Surface functionalization with (thiol-) phospholipids*.** The NPs were coated with phospholipids via a solvent exchange method. In this method, 0.3 mL 1.0 mg/mL nanoparticles in toluene was added to a solution of 10 mg DSPE-mPEG and 1 mg DSPE-PEG-SH. 4 mL DMSO was added to this mixture. This was shaken for 1 hour on a shake-plate. To remove the toluene, the mixture was put in a rotary evaporator, spinning under vacuum for 1 hour. DMSO was then exchanged for water using a 50k MWCO filtration tube, centrifuging for 30 minutes at 2,000 g, adding de-ionized (DI) water, and repeating two times. The final time, 1 mL DI water was added, resulting in a 1.1 mL dispersion of nanoparticles functionalized with 1:10 DSPE-PEG-SH:DSPE-mPEG.

The functionalization with strictly DSPE-mPEG occurred in the same fashion, except the DSPE-PEG-SH was omitted and 11 mg of DSPE-mPEG was used.

Photo-protection. The thiol groups on the functionalized NP surface were chemically protected using 2-bromo-4’-hydroxyacetophenone. In the protection step, 0.25 mL 0.1 mg/mL NP dispersion was added to 2.25 mL 2 mM 2-bromo-4’-hydroxyacetophenone solution in 1 M phosphate buffer saline (PBS) solution in a 5 mL vial. The vial was wrapped in aluminium foil to protect it from light. The mixture was shaken on a shake-plate over night.

Photo-removal demonstration. A commercial thiol-detection kit was used to demonstrate exposure of thiols after UV-light exposure. In a photo-removal experiment,

0.1 mL of the commercial thiol-detection kit in DMSO was added to 2 mL of a previously photo-protected thiol-functionalized nanoparticle sample in water in a quartz cuvette.

To measure the response of the thiol-activated fluorescence, the sample was excited at 490 nm using light from a xenon lamp passed through a monochromator. The emission was measured and corrected for instrument response using a Peltier-cooled Hamamatsu R928P PMT between 500 and 550 nm. Counts were integrated for 1 s at every 1 nm step using a 1 nm slit width. The detector was positioned at a 90-degree angle with respect to the excitation source. A 495 nm long-pass filter was placed between the sample and the detector.

To demonstrate the effect of photo-removal, the sample was excited at 350 nm for 15 minutes, and emission upon 490 nm excitation was measured again.

Trapping and anchoring. Gold double-nanohole aperture samples were attached to an adhesive spacer on a glass coverslip containing 10 µL of the NP solution. Optical trapping was performed using an inverted microscope optical tweezers setup with a 980 nm continuous-wave laser (JDS Uniphase SDLO-27-7552-160-LD) focussed on the sample with a 100× oil immersion microscope objective. The laser power used for trapping varied with the aperture used and ranged from 4-14 mW, as measured before the 100× objective. Gold double-nanohole apertures in the sample were aligned to the laser using a three-axis stage with 20 nm resolution piezo adjustment by maximizing the amplitude of the transmitted light. The light transmitted through the aperture was collected with a 10×

microscope objective and measured by an avalanche photodetector (Thorlabs APD120A). A 340 nm light source was focussed on the sample through the same 10× microscope objective and was used to trigger anchoring by illuminating the optically trapped NPs by transmission through the apertures.

5.5 References

1. Zoller, P.; Beth, T.; Binosi, D.; Blatt, R.; Briegel, H.; Bruss, D.; Calarco, T.; Cirac, J. I.; Deutsch, D.; Eisert, J., Quantum Information Processing and Communication. *EPJ D* **2005,** *36*, 203-228.
2. Bennett, C. H.; Brassard, G., A Quantum Information Science and Technology Roadmap. *Quantum Cryptography* **2004,** *2*, 12.
3. *Quantum Computing: Progress and Prospects*. National Academies of Sciences, Engineering, Medicine: 2019.
4. Dibos, A.; Raha, M.; Phenicie, C.; Thompson, J. D., Atomic Source of Single Photons in the Telecom Band. *Phys. Rev. Lett.* **2018,** *120*, 243601.
5. Eisaman, M. D.; Fan, J.; Migdall, A.; Polyakov, S. V., Invited Review Article: Single-Photon Sources and Detectors. *Rev. Sci. Instrum.* **2011,** *82*, 071101.
6. Gisin, N., How Far Can One Send a Photon? *Front. Phys.* **2015,** *10*, 1-8.
7. Reisfeld, R., Optical Properties of Lanthanides in Condensed Phase, Theory and Applications. *AIMS Mater. Sci.* **2015,** *2*, 37-60.
8. De Greve, K.; Yu, L.; McMahon, P. L.; Pelc, J. S.; Natarajan, C. M.; Kim, N. Y.; Abe, E.; Maier, S.; Schneider, C.; Kamp, M., Quantum-Dot Spin–Photon Entanglement Via Frequency Downconversion to Telecom Wavelength. *Nature* **2012,** *491*, 421-425.
9. Bernien, H.; Hensen, B.; Pfaff, W.; Koolstra, G.; Blok, M. S.; Robledo, L.; Taminiau, T. H.; Markham, M.; Twitchen, D. J.; Childress, L., Heralded Entanglement between Solid-State Qubits Separated by Three Metres. *Nature* **2013,** *497*, 86-90.

10. Giles, C. R.; Desurvire, E., Propagation of Signal and Noise in Concatenated Erbium-Doped Fiber Optical Amplifiers. *J. Lightwave Technol.* **1991,** *9*, 147-154.

11. Kolesov, R.; Xia, K.; Reuter, R.; Stöhr, R.; Zappe, A.; Meijer, J.; Hemmer, P. R.; Wrachtrup, J., Optical Detection of a Single Rare-Earth Ion in a Crystal. *Nat. Commun.* **2012,** *3*, 1029.

12. Zhong, T.; Kindem, J. M.; Bartholomew, J. G.; Rochman, J.; Craiciu, I.; Verma, V.; Nam, S. W.; Marsili, F.; Shaw, M. D.; Beyer, A. D., Optically Addressing Single Rare-Earth Ions in a Nanophotonic Cavity. *Phys. Rev. Lett.* **2018,** *121*, 183603.

13. Groot-Berning, K.; Kornher, T.; Jacob, G.; Stopp, F.; Dawkins, S. T.; Kolesov, R.; Wrachtrup, J.; Singer, K.; Schmidt-Kaler, F., Deterministic Single-Ion Implantation of Rare-Earth Ions for Nanometer-Resolution Color-Center Generation. *Phys. Rev. Lett.* **2019,** *123*, 106802.

14. Alizadehkhaledi, A.; Frencken, A. L.; van Veggel, F. C. J. M.; Gordon, R., Isolating Nanocrystals with an Individual Erbium Emitter: A Route to a Stable Single-Photon Source at 1550 nm Wavelength. *Nano Lett.* **2020,** *20*, 1018-1022.

15. Sharifi, Z.; Dobinson, M.; Hajisalem, G.; Shariatdoust, M. S.; Frencken, A. L.; van Veggel, F. C. J. M.; Gordon, R., Isolating and Enhancing Single-Photon Emitters for 1550 nm Quantum Light Sources Using Double Nanohole Optical Tweezers. *J. Chem. Phys.* **2021,** *154*, 184204.

16. Alizadehkhaledi, A.; Frencken, A. L.; Dezfouli, M. K.; Hughes, S.; van Veggel, F. C. J. M.; Gordon, R., Cascaded Plasmon-Enhanced Emission from a Single Upconverting Nanocrystal. *ACS Photonics* **2019,** *6*, 1125-1131.

17. Pang, Y.; Gordon, R., Optical Trapping of 12 nm Dielectric Spheres Using Double-Nanoholes in a Gold Film. *Nano Lett.* **2011,** *11*, 3763-3767.

18. Bürgi, T., Properties of the Gold–Sulphur Interface: From Self-Assembled Monolayers to Clusters. *Nanoscale* **2015,** *7*, 15553-15567.

19. Li, Z.; Zhang, Y., An Efficient and User-Friendly Method for the Synthesis of Hexagonal-Phase $NaYF_4$: Yb, Er/Tm Nanocrystals with Controllable Shape and Upconversion Fluorescence. *Nanotechnology* **2008,** *19*, 345606.

20. Boyer, J. C.; van Veggel, F. C. J. M., Absolute Quantum Yield Measurements of Colloidal $NaYF_4$: Er^{3+}, Yb^{3+} Upconverting Nanoparticles. *Nanoscale* **2010,** *2*, 1417-1419.

21. Haight, F. A. *Handbook of the Poisson Distribution*; 1967.

22. Frencken, A. L.; Blackburn, A. M.; van Veggel, F. C. J. M., The Internal Structure of Lanthanide-Doped Nanoparticles and the Effect of High-Temperature Annealing on Their Luminescent Properties. *J. Phys. Chem. C* **2022,** *126*, 16341–16348.

23. Dong, C.; Pichaandi, J.; Regier, T.; van Veggel, F. C. J. M., Nonstatistical Dopant Distribution of Ln^{3+}-Doped $NaGdF_4$ Nanoparticles. *J. Phys. Chem. C* **2011,** *115*, 15950-15958.

24. Tong, S.; Hou, S.; Ren, B.; Zheng, Z.; Bao, G., Self-Assembly of Phospholipid - PEG Coating on Nanoparticles through Dual Solvent Exchange. *Nano Lett.* **2011,** *11*, 3720-3726.

25. Arabacı, G.; Guo, X.; Beebe, K.; Coggeshall, K.; Pei, D., Alpha-Haloacetophenone Derivatives as Photoreversible Covalent Inhibitors of Protein Tyrosine Phosphatases. *J. Am. Chem. Soc.* **1999,** *121*, 5085–5086.

26. Chen, X.; Ko, S.-K.; Kim, M. J.; Shin, I.; Yoon, J., A Thiol-Specific Fluorescent Probe and Its Application for Bioimaging. *Chem. Commun.* **2010,** *46*, 2751-2753.

27. Wang, K.; Peng, H.; Wang, B., Recent Advances in Thiol and Sulfide Reactive Probes. *J. Cell. Biochem.* **2014,** *115*, 1007-1022.

Chapter 6: X-ray Sensitive Doped CaF_2-Based MRI Contrast Agents to Measure *in vivo* and Locally the Radiation Dose

Based on:

Frencken, A. L.; Richtsmeier, D.; Williams, A.; Johnson, C. E.; Johnson, J. A.; Blasiak, B.; Orlef, A.; Skorupa, A.; Sokol, M.; Woznica, A.; Kapek, L; Ciszek, M.; Swakon, J.; Tomanek, B.; Beckham, W.; Bazalova-Carter, M.; van Veggel, F. C. J. M., X-ray Sensitive Doped CaF_2-Based MRI Contrast Agents to Measure *in vivo* and Locally the Radiation Dose. *To be submitted.*

Mössbauer spectroscopy was performed by the group of Jacqueline Johnson (UTSI). Dose experiments at treatment energies were performed by the group of Agnieszka Skorupa (MSCNRIO). The experimental section detailing the dose experiments at treatment energies was provided by Agnieszka Skorupa (MSCNRIO).

Abstract

Ionizing radiation has become widely used in medicine, seeing application in both diagnostic techniques, such as computed tomography (CT), and therapeutic techniques, where high-energy x-rays are used to treat tumors. The x-rays used can have harmful effects, and an accurate determination of the delivered radiation dose is of utmost importance to minimize any damage done to healthy tissue. For this, medical specialists mostly rely on theoretical predictions of delivered dose or measurement of the dose externally. To extend the practical use of ionizing radiation-based medical techniques, a more precise measure of radiation dose internally is required. In this chapter, a novel approach is presented to measure precisely and *in vivo* the amount of radiation. The strategy relies on magnetic resonance imaging (MRI) contrast agents (CAs) that have a dose sensitive signal. The materials demonstrated are (citrate-capped) CaF_2 nanoparticles (NPs) doped with Eu^{3+} or Fe^{2+}/Fe^{3+} ions. Free electrons generated by ionizing radiation allow for reduction of Eu^{3+}, which only induces a very small contrast in MRI, to Eu^{2+}, which induces a strong contrast. Oxidative species generated by high-energy x-rays can be measured indirectly using Fe^{2+}, because it oxidizes to Fe^{3+}, increasing the contrast in MRI. In the results, notably a strong increase in the proton relaxation rates is observed for the Eu^{3+} doped NPs at 40 keV. At 6 MeV a significant increase in proton relaxation rates is observed using CaF_2 NPs doped with Fe^{2+}. The concept presented shows great promise for use in the clinic to measure *in vivo* and locally ionizing radiation dose.

6.1 Introduction

The use of ionizing radiation has become ubiquitous in modern day medicine. CT (computed tomography) scan-based techniques use ionizing radiation to image parts of the body, visualizing tissue for diagnosis.[1-3] In radiotherapy, high-energy x-rays are used to destabilize and shrink tumors. Owing to its high success rate, radiotherapy sees widespread use in the treatment of cancer.[4-8]

Ionizing radiation-based diagnosis and treatment techniques both rely on an accurate estimation of the delivered radiation dose at the specific target. A dose that is too low may provide insufficient signal for a reliable diagnosis, leading to poor visualization of the analyzed tissue. In radiotherapy, an underestimation of the treatment dose may lead to inadequate destabilization of the tumor, or in worse cases, to the tumor developing a resistance to the ionizing radiation used. Conversely, the x-ray dose cannot be too high in these techniques, as an excess of ionizing radiation could lead to excessive damage of healthy tissue. In the worst cases, this has led to patient death.[5-6]

To determine the right amount of radiation for the radiology techniques, dosage is routinely predicted by Monte Carlo simulations,[9] but methods to measure accurately and *in vivo* the delivered radiation dose are in high demand. Methods to measure radiation dose *in vivo* that have been employed primarily rely on measuring radiation externally using diodes,[10-11] metal-oxide semi-conductor field effect transistors (MOSFET),[12-13] and thermoluminescent detectors (TLD).[14-16] To increase the accuracy of delivered dose detection at the tumor location, methods have been suggested to develop sensors that can

measure internally radiation, but these rely on implementation of a wired dosimeter at the tumor location, either by placement inside an orifice of the patient or *via* invasive implementation inside the tissue of interest.[10]

In this chapter, materials are proposed and demonstrated that can potentially be used to measure radiation inside tissue *in vivo*, at the location of the tissue of interest, and *non-invasively*. As an analysis technique to demonstrate dose potentially *in vivo*, MRI is chosen, for its limitless depth of penetrations, as well as being non-invasive.[17] MRI routinely employs contrast agents (CAs), chemicals that enhance MRI contrast locally by enhancement of proton relaxation rate(s), T_1 (spin-lattice relaxation time) and/or T_2 (the spin-spin relaxation time), in the applied magnetic field.[18-19] The strategy relies on utilizing CAs that change their contrast based on interaction with ionizing radiation as well as having a dose-invariant signal for calibration purposes.

The materials studied here are CaF_2 NPs doped with Eu^{3+} ions, and CaF_2 NPs doped with Fe^{2+} ions. The hypothesis is that CaF_2 doped with Eu^{3+} can be activated as a T_1 MRI CA by absorption of an x-ray, leading to an excited state electron able to reduce Eu^{3+} to Eu^{2+}, which is a highly effective T_1 CA.[20-21] For the Fe^{2+}-doped material, oxidative species generated by ionizing radiation can oxidize the Fe^{2+} to Fe^{3+}, of which Fe^{3+} is a good T_1 CA.[22-23]

The materials in this study are made *via* colloidal methods, and the oxidation state of the dopant ions confirmed with Mössbauer spectroscopy. The change in T_1 and T_2 of these

materials is tested and demonstrated at the diagnostic x-ray energies of 40 keV, and at therapeutic energies of 6 MeV.

6.2 Results and discussion

6.2.1 Doped CaF_2 synthesis and characterization

CaF_2 NPs were synthesized using colloidal synthesis methods reported in literature.[24] The method was later adapted to use citrate ligands to increase NP stabilization.[25] Four types of nanocrystals were synthesized: CaF_2, CaF_2:Fe^{2+}/Fe^{3+}, CaF_2:Eu^{3+} and CaF_2:Y^{3+}. The dopant amount used in the syntheses was ca. 20%. All syntheses yielded clear dispersions, indicating good dispersability of the NPs in water. To confirm successful synthesis, transmission electron microscopy (TEM), x-ray diffraction (XRD), ICP-MS, and Mössbauer spectroscopy were performed.

Figure 6.1 shows representative TEM figures of CaF_2:Eu^{3+} NPs without (a) and with (b) citrate ligands. TEM figures of CaF_2:Fe^{2+}/Fe^{3+} NPs without (c) and with citrate ligands (d) are shown as well. The nanoparticles are observed to be near spherical and sized between 5 and 10 nm in diameter. On the TEM grids, it appears that the uncapped nanoparticles are more likely to aggregate upon drying, as a result of the lack of steric repulsion that the organic citrate ligands provide.

ICP-MS performed on representative doped samples revealed dopant concentrations in the doped nanocrystals to be 19.7% Y^{3+} in CaF_2:Y^{3+}, 16.6% Eu^{3+} in CaF_2:Eu^{3+}, and only 0.3% Fe in CaF_2:Fe^{2+}/Fe^{3+}. The low concentration Fe can be explained by the significantly smaller ionic radii of Fe^{2+} and Fe^{3+} (78.0 and 64.5 pm, respectively) compared to Ca^{2+}

(100.0 pm). Furthermore, Fe^{2+} and Fe^{3+} have d-orbital electrons, whereas Ca^{2+} does not. The much smaller size and presence of d-orbital electrons may make the Fe^{2+} or Fe^{3+} ion a poor ion to substitute Ca^{2+} in the lattice. The ionic radii of Eu^{3+} and Y^{3+} (94.7 and 90.0 pm, respectively) match the Ca^{2+} ionic radius much more closely by comparison and their occupied d-orbitals are not expected to interact due to their small radius, so these ions are expected to fit the CaF_2 lattice better.[26]

In Figure 6.1 (e) and (f), XRD patterns are shown collected on CaF_2:Eu^{3+} NPs with and without citrate ligands, respectively. Peaks correspond closely to the CaF_2 reference diffractogram shown in black. The slight shift towards lower angles is explained by distortion that widens the crystal lattice because of the dopant ion causing strain in the crystal lattice. Also, to compensate the charge of Eu^{3+} on a Ca^{2+} position, interstitial F^- ions are present that contribute to the crystal strain, which has been observed in other work.[27] Figure 6.1 (g) and (h) show XRD patterns of CaF_2:Fe^{2+}/Fe^{3+} NPs with and without citrate ligands, respectively. Peaks correspond more closely to the CaF_2 reference pattern, as a result of the lower dopant concentration. In addition, in (g), a few very small peaks are seen between 20 and 30 ° as a possible result of a FeF_2 or FeF_3 precipitate on the XRD substrate. Using the Scherrer equation, particle sizes were calculated from the XRD peak widths.[28] Diameters were determined to be 7.2 nm for the uncapped CaF_2:Eu^{3+} NPs, 6.9 nm for the citrate-capped CaF_2:Eu^{3+} NPs, 10.8 for the uncapped CaF_2:Fe^{2+}/Fe^{3+} NPs, and 6.0 nm for the citrate-capped CaF_2:Fe^{2+}/Fe^{3+} NPs. The particle sizes correspond well with sizes observed in TEM. The trend observed is that the citrate-based synthesis yields slightly smaller NPs, possibly because of the ligands stabilizing smaller particles.

Mössbauer spectroscopy results are shown in Figure 6.2. Predicted fits of Eu^{3+}, Fe^{2+}, and Fe^{3+} to the spectra reveal that the iron-doped CaF_2 NPs were doped with a mixture of Fe^{2+} and Fe^{3+} and the europium-doped CaF_2 NPs with exclusively Eu^{3+}.

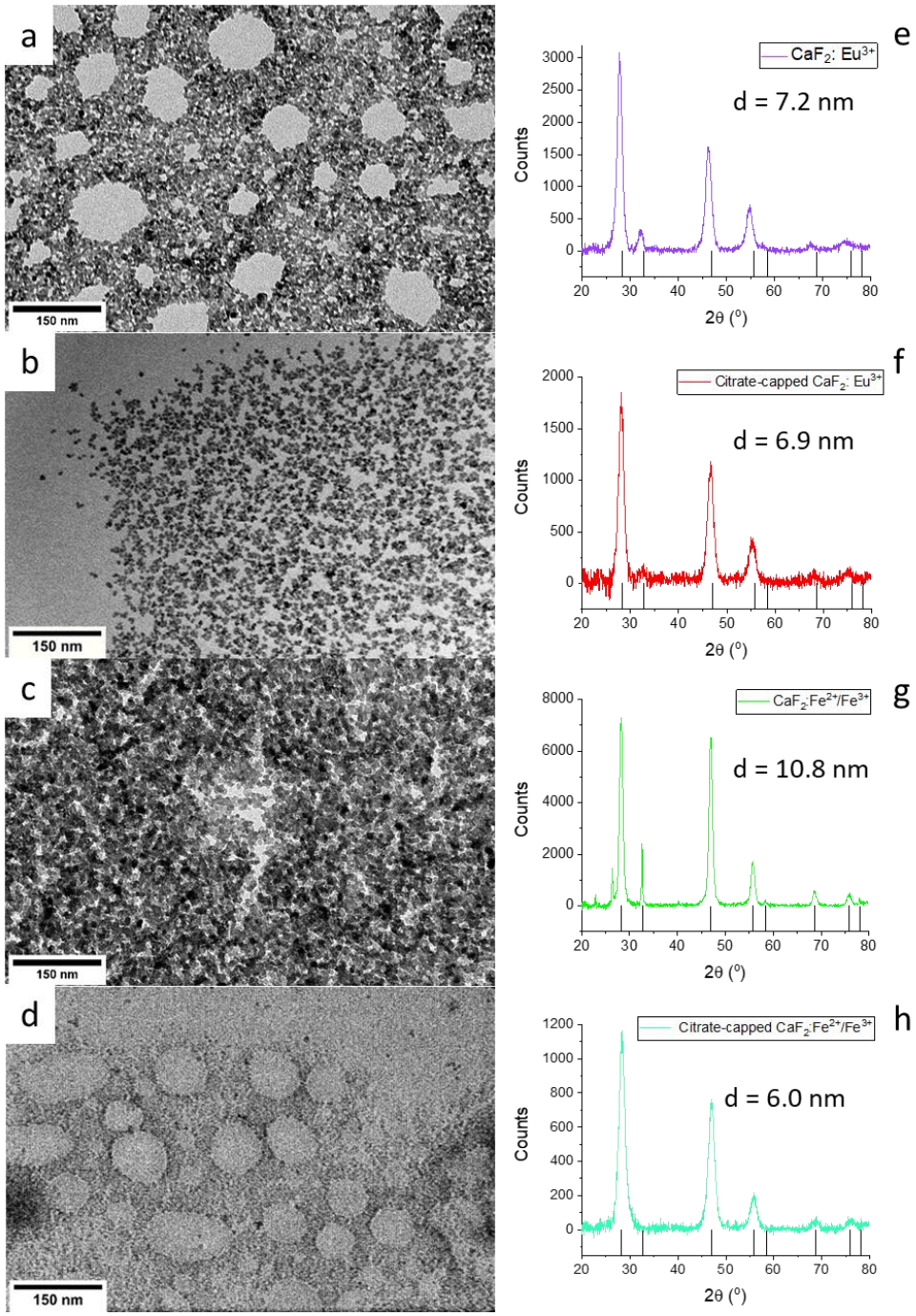

Figure 6.1: (a-d) Representative TEM images taken of NPs at 250,000x magnification. (e-h) Corresponding XRD patterns of NPs with reference pattern for cubic CaF_2 (00-035-0816) (black bars). NP materials are uncapped CaF_2:Eu^{3+} (a, e), citrate-capped CaF_2:Eu^{3+} (b, f), uncapped CaF_2:Fe^{2+}/Fe^{3+} (c, g), and citrate-capped CaF_2:Fe^{2+}/Fe^{3+} (d, h). Diameters calculated from the XRD peak width are shown near the XRD patterns.

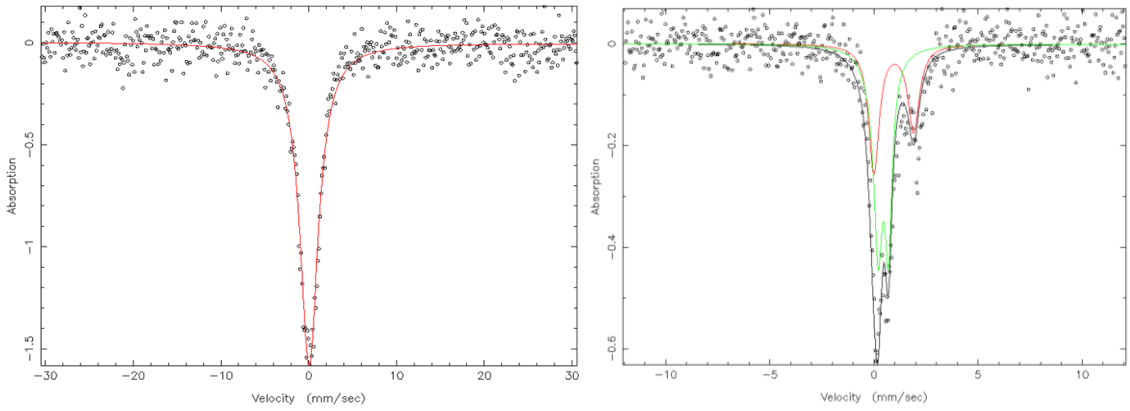

Figure 6.2: (left) Mössbauer spectrum of Eu^{3+} with Eu^{3+} fit in red, (right) Mössbauer spectrum of Fe^{2+} and Fe^{3+} with Fe^{2+} fit in red, Fe^{3+} fit in green.

6.2.2 Dosimetry experiments

Irradiation experiments were performed to test the efficacy of doped CaF_2 NPs as MRI-based dosimeters. Dosimetry demonstrations were done at 40 keV, being in the range of energies used for diagnostic x-ray techniques, and at 6 MeV, which is in the range of energies used in x-ray therapeutic treatment of tumors.

In this discussion, the effects of ionizing radiation are compared at 40 keV and 6 MeV on CaF_2 NPs doped with Eu^{3+} and CaF_2 NPs doped with a mixture of Fe^{2+} and Fe^{3+}. Finally, the effect of a dose-invariant internal standard is tested by demonstrating the effect of 40 keV radiation on a mixture of CaF_2:Eu^{3+} and $NaDyF_4$. The discussion is ordered a follows:

1. The experiments at 40 keV are described, comparing the effects of this diagnostic radiation energy on the two doped systems.
2. The effects of 6 MeV radiation on CaF_2:Eu^{3+} NPs and CaF_2:Fe^{2+}/Fe^{3+} NPs are compared.

3. Recommendations for the ideal doped system are given to measure radiation dose at low and high x-ray energies.
4. A demonstration of radiation effects on CaF_2:Eu^{3+} NPs with an internal standard ($NaDyF_4$ NPs) is given.

6.2.3 Nanoparticle dosimetry at diagnostic energies

In a typical 40 keV irradiation experiment, the T_1 and T_2 relaxation times of a ca. 20 mg/mL CaF_2 NP dispersion in water were measured. Then, the dispersion was exposed to ionizing radiation from a tungsten tube operated at a 40 keV potential, effectively delivering a radiation dose of ~200 Gy into the dispersion (as determined with Monte Carlo simulations), before measuring T_1 and T_2 again. A CaF_2 NP dispersion was used as a control to determine whether the CaF_2 material in water was responsible for the relaxivity change. CaF_2:Y^{3+} was also used as a control to determine whether a diamagnetic dopant ion would have an effect, as a result of the dopant ion distorting the lattice.

In Figure 6.3, the change in $1/T_1$ (top left; $1/T_1 = r_1$, the spin-lattice relaxation rate) and $1/T_2$ (top right; $1/T_2 = r_2$, the spin-spin relaxation rate) of Eu^{3+}-doped CaF_2 NPs is demonstrated with respect to the irradiation event, indicated with a red divider. Here, a strong rise of $1/T_1$ is observed directly after irradiation, followed by drop over time. A similar effect is observed for $1/T_2$. The change in relaxation times can be explained by the reduction of Eu^{3+} to Eu^{2+} upon generation of high-energy electrons by the incident radiation, which can directly reduce Eu^{3+}. In the 22 hours after irradiation of the sample, $1/T_1$ and $1/T_2$ were observed to drop down again, which is likely caused by oxidation of Eu^{2+} back to Eu^{3+}. These observations are in line with the expectation that 40 keV radiation

mainly induces photo-electric interactions, leading to photo-electrons. The probability of this interaction taking place at a specific atom scales with its atomic number as ~Z^4, so the likelihood of this occurrence is highest in the high Z CaF_2:Eu^{3+} dopant ions, as compared with water.[29]

The radiation dose may potentially have an effect on the CaF_2 host material as well. To verify whether there is any significant change due to irradiation on the $1/T_1$ and $1/T_2$ values from the CaF_2 crystal, a dose experiment was performed on undoped CaF_2 NPs. Furthermore, to see whether any of the observed effects were due to defects generated by dopant ions, the experiment was performed on CaF_2:Y^{3+} as well. In this, Y^{3+} is a diamagnetic ion that is not expected to have any effect on $1/T_1$ or $1/T_2$.

In the CaF_2 and CaF_2:Y^{3+} irradiation experiments, instead of a rise, a small drop in relaxivities is observed upon irradiation, see Figure 6.3 (bottom). This is attributed mainly to paramagnetic oxygen leaving the sample because of heating up during x-ray exposure, which was inferred by observation of bubble formation after irradiation in the dispersions. Correspondingly, gas bubble formation was observed inside the NMR-tubes after they had been irradiated. No significant effect of the diamagnetic lanthanide dopant ion is observed in the irradiation experiment, compared to pure CaF_2. The change in $1/T_1$ and $1/T_2$ does not recover fully after 22 hours post exposure, as a possible result of oxygen not fully dissolving back into the water. This also explains why the $1/T_2$ value measured in CaF_2:Eu^{3+} drops below its starting value in the 22 hours after irradiation, as Eu^{2+} oxidizes

back to Eu^{3+}, which leads to a drop in relaxivities that is lower than when oxygen was present.

The drop in T_1 and T_2 upon irradiation of diamagnetic particles in water inside human tissue is not expected, as O_2 is not expected to form bubbles due to blood flow and bodily temperature regulation, so the effects observed in CaF_2 NPs can be interpreted as a background T_1 and T_2 change in the experiment. In the following presented data, this background signal has been subtracted to further highlight the effect of radiation on the Eu^{3+} and Fe^{2+}/Fe^{3+} ions.

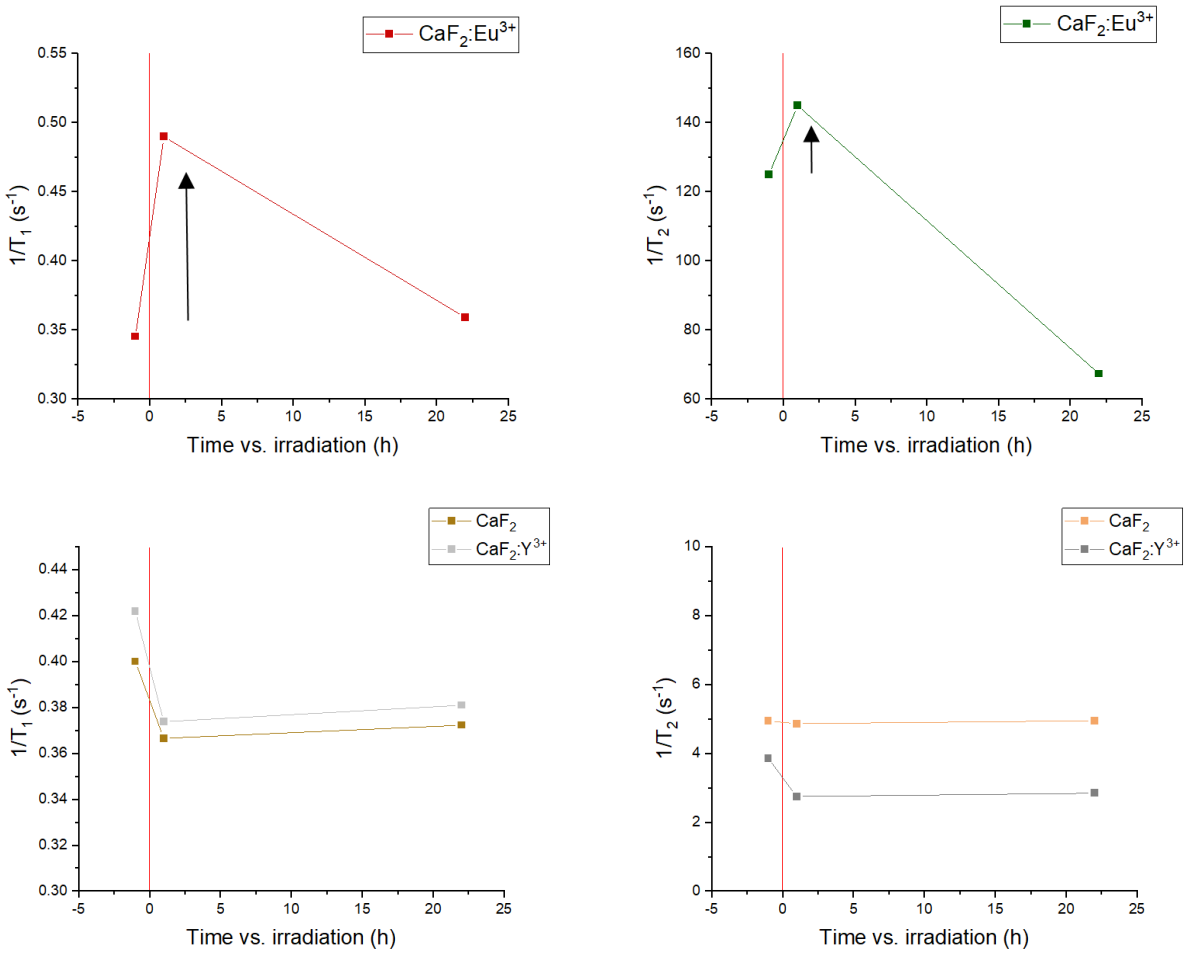

Figure 6.3: (top) Change in $1/T_1$ and $1/T_2$ of $CaF_2:Eu^{3+}$ and (bottom) CaF_2 and $CaF_2:Y^{3+}$ NPs with respect to 40 keV irradiation event (indicated with a red divider). A rise after irradiation is seen for the Eu^{3+} NPs, whereas only a drop is seen for the other NPs.

Between CaF_2 and $CaF_2:Y^{3+}$, only very small differences in $1/T_1$ and $1/T_2$ are observed. The differences are significantly smaller than the change observed in $CaF_2:Eu^{3+}$, and as expected, the diamagnetic Y^{3+} ion influences relaxivities minimally, both before and after irradiation. The differences that are observed might be attributed to small differences in NP concentration during the experiment.

Now that a significant qualitative effect of radiation on $CaF_2:Eu^{3+}$ has been demonstrated, its applied use as a dosimeter can be tested by varying the radiation dose. Three different irradiation experiments were compared, varying only the irradiation time, resulting in a difference in the delivered dose. These results are shown in the graphs in Figure 6.4. It was observed that as the radiation time increased, the increase in T_1 and T_2 increased as well. Under these graphs, the dose dependence of the change in $1/T_1$ and $1/T_2$ measured one hour after irradiation is shown. The effects are observed to be linear, with the relaxation rates showing a constant increase, scaling with the radiation dose. Linear functions were fitted to the data, and from the linear fits, the change in T_1 and T_2 can be calculated for lower doses. For example, 1 Gy (within an order of magnitude of the high end of clinical doses)[30-31] would result in a radiation induced decrease of 7 ms in T_1 of pure water, and 20 ms in T_2. In this example, the drop in T_1 is 0.25% and the drop in T_2 4.5%. Uncertainties in the determined relaxation times are typically about 1.5%,[32] arising from uncertainties in the pulse sequence, or due to flow or movement in tissue.[33] This means that in this demonstration, the T_2 effect could be used reliably to determine the radiation dose at 1 Gy. The effect is shown schematically under the graphs, illustrating that when the amount of Eu^{2+} in the NPs increases, the relaxivity rises from low to high. This result is encouraging and means that the Eu^{3+}-doped material can be used to measure quantitatively the radiation dose.

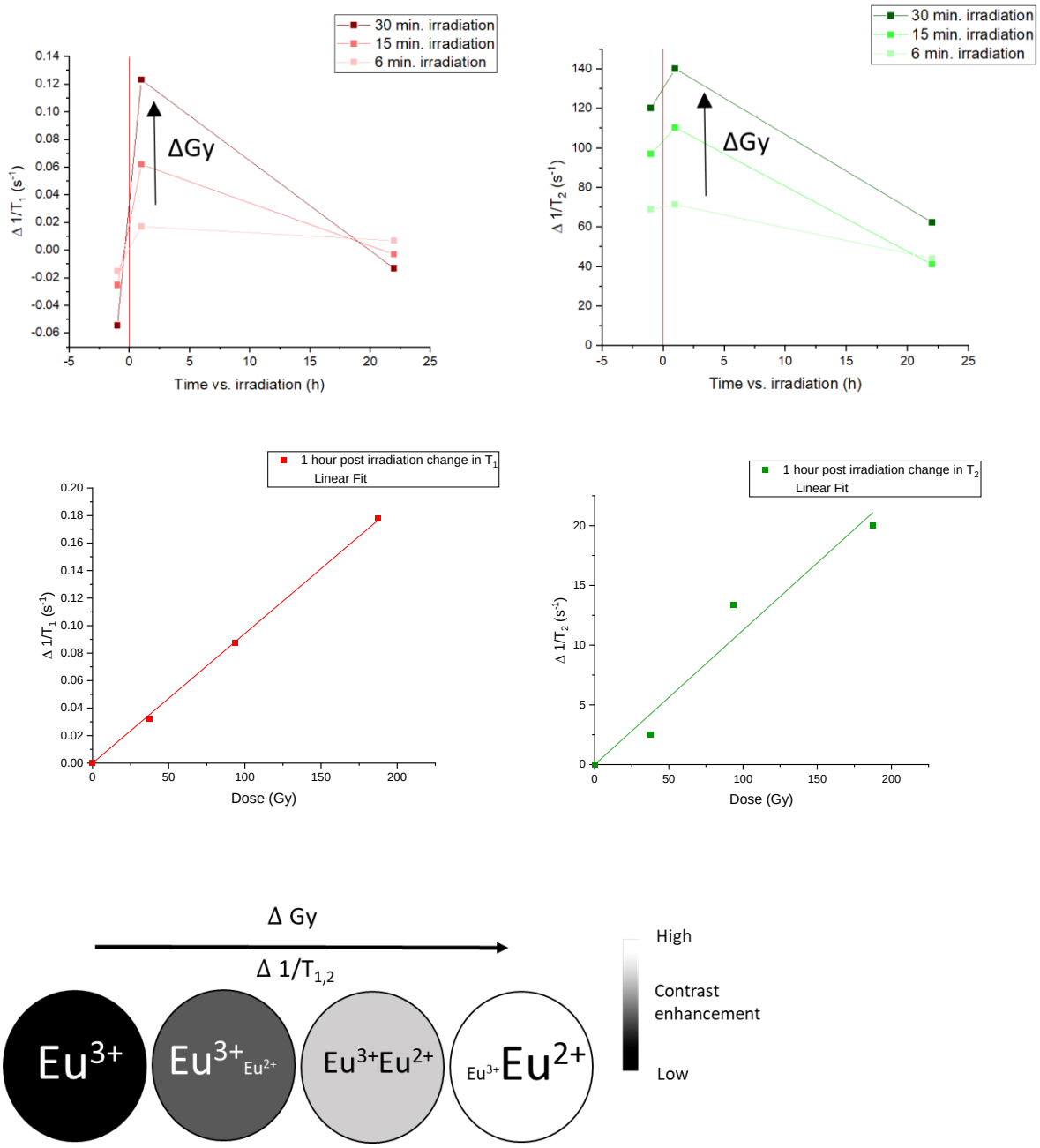

Figure 6.4: The top graphs show the change in $1/T_1$ and $1/T_2$ of CaF_2:Eu^{3+} NPs measured at different times with respect to varying irradiation times using 40 keV x-rays. A CaF_2 relaxation rate background signal was subtracted. The irradiation event is indicated with a red divider. The graphs underneath show the dose dependence on the change before and one hour after irradiation, with linear fits fixed to go through the origin. A schematic depiction of the relaxivity change with radiation dose is shown below the graphs.

It was hypothesized that the change in T_1 and T_2 occurred upon reduction of Eu^{3+} to Eu^{2+}, and that the increased electronic relaxation time and magnetic moment of Eu^{2+} contribute to the decrease in T_1 and T_2 respectively. To verify this hypothesis further, emission of Eu^{3+} upon 394 nm excitation was measured before and after irradiation as well. In Figure 6.5 (left), the characteristic emission lines of Eu^{3+} are seen. In Figure 6.5 (right), the integrated intensity of the peaks is plotted with respect to the irradiation event (red divider). A sharp drop in emission intensity occurs for all peaks after irradiation at 40 keV, which can be attributed to Eu^{3+} being reduced to Eu^{2+}, followed by a rise over time, which can be attributed to oxidation of Eu^{2+} back to Eu^{3+} under ambient conditions. This corresponds well with the observation that the relaxation times drop after radiation exposure, and provides further evidence for the reduction of Eu^{3+} after irradiation.

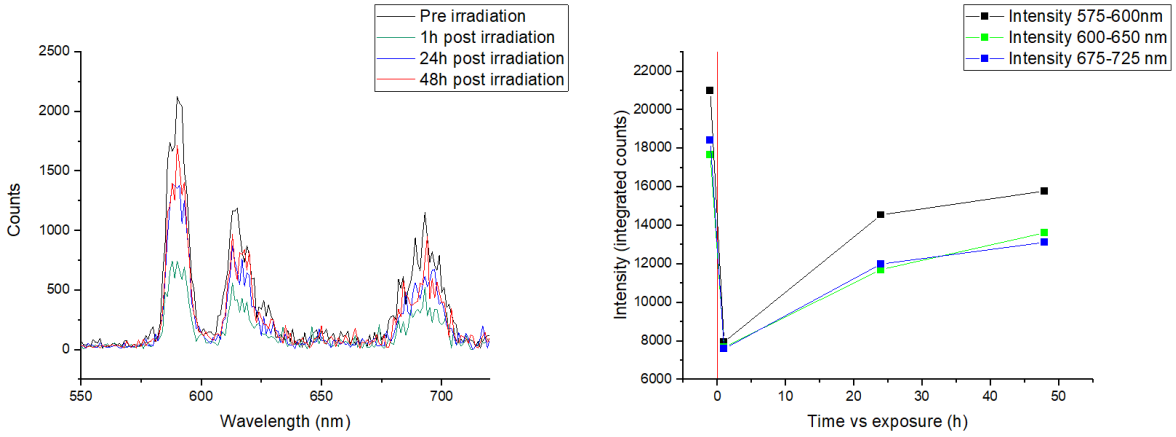

Figure 6.5: Characteristic Eu^{3+} emission measured before, and at several time points after 40 keV irradiation.

Experiments were done on charge stabilized CaF_2:Eu^{3+}, but it was suggested that capping the nanoparticles with a citrate surface molecule could help long-term colloidal stability.

Figure 6.6 shows a comparison between charge stabilized and citrate-stabilized $CaF_2:Eu^{3+}$ NPs during a typical irradiation experiment. Only relaxivity 1 hour after irradiation was measured for the citrate-stabilized sample. Qualitatively, the results are the same, and a similar rise in $1/T_1$ and $1/T_2$ can be observed after irradiation, attributed to reduction of Eu^{3+} to Eu^{2+}. This suggests that the capping with citrate does not influence the effect of radiation on the oxidation state of the dopant ion significantly. Quantitative differences in the intensity of measured relaxivities can be attributed to possible differences in concentration and particle size.

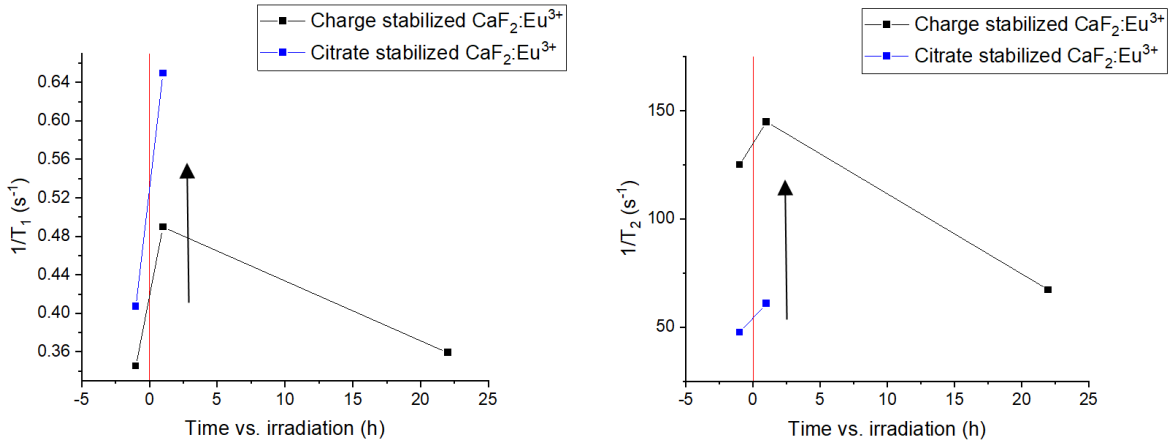

Figure 6.6: Change in relaxivities of uncapped and citrate-capped $CaF_2:Eu^{3+}$NP upon 40 keV irradiation for 30 min. (red line).

Besides $CaF_2:Eu^{3+}$, dosimetry experiments were conducted on $CaF_2:Fe^{2+}/Fe^{3+}$ as well. The same experiment was performed, where the relaxation times of a dispersion of CaF_2 NPs doped with Fe^{2+} and Fe^{3+} were measured, and irradiation was performed for 30 minutes with 40 keV x-rays. Pure CaF_2 dispersion relaxation times were subtracted as a background in the same way as for the dose series on $CaF_2:Eu^{3+}$. The results are shown in

Figure 6.7. Here, opposite to the effect observed in Eu^{3+}-doped NPs, a sharp drop in $1/T_1$ and $1/T_2$ is observed upon irradiation. In the time after this, a rise is observed again. These results can be explained by a similar irradiation effect as in CaF_2 doped with Eu^{3+}, where Fe^{3+} is reduced upon irradiation, leading to Fe^{2+}, which has a shorter electron relaxation time and smaller magnetic moment than Fe^{3+}. Over time a recovery in relaxation times could be observed, which is explained by Fe^{2+} oxidizing back to Fe^{3+}.

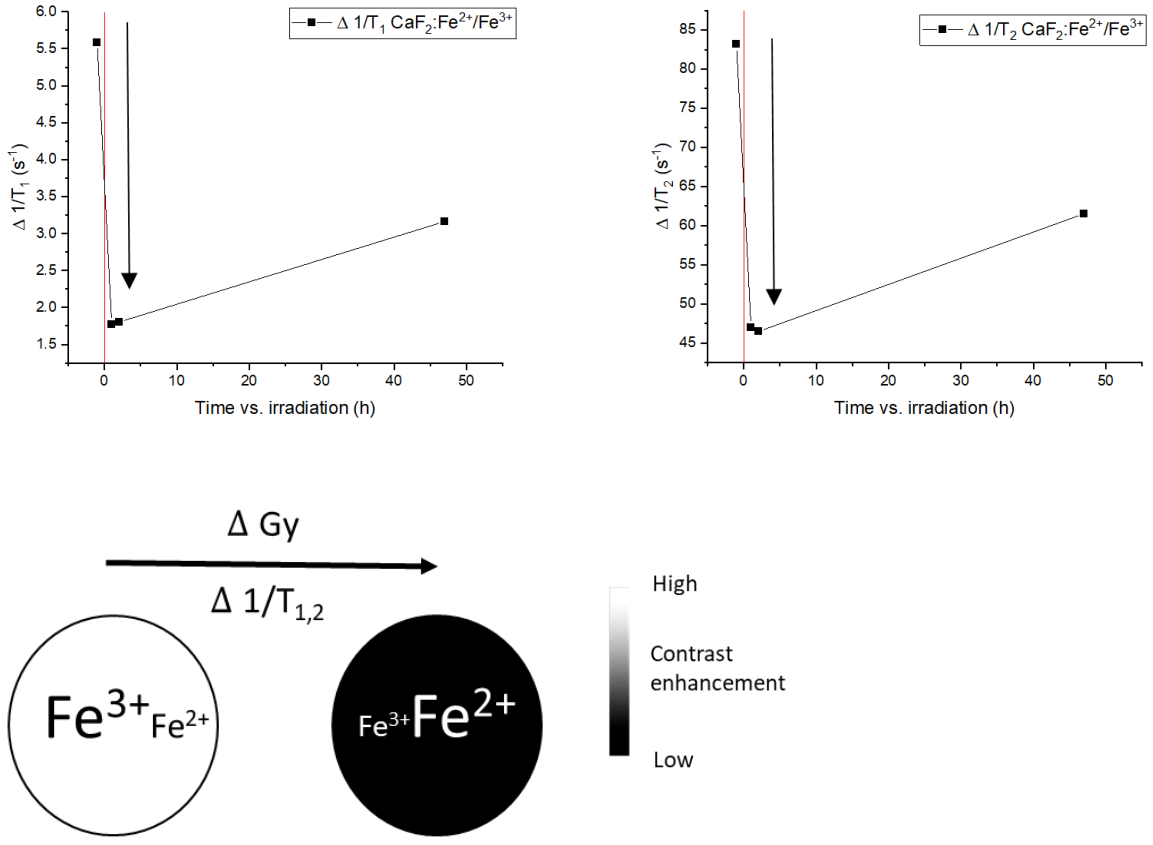

Figure 6.7: $1/T_1$ and $1/T_2$ of CaF_2:Fe^{2+}/Fe^{3+} NPs after background subtraction measured at different times with respect to 30 min. 40 keV irradiation. The irradiation event is indicated with a red divider. Bellow, a schematic figure is shown indicating the change in relaxivities upon x-ray exposure as the amount of Fe^{2+} in the particles increases.

From these experiments, it is concluded that both $CaF_2:Eu^{3+}$ NPs and $CaF_2:Fe^{2+}/Fe^{3+}$ can both be used for *in vivo* dosimetry using MRI contrast, at diagnostic x-ray energies. The Eu^{3+}-doped NPs showed a strong increase in $1/T_1$ and $1/T_2$ relaxivities and the Fe^{2+}/Fe^{3+}-doped NPs showed a strong decrease. $CaF_2:Eu^{3+}$ would be the preferred candidate due to the observed effect that it specifically activates as a contrast agent, allowing a measurement of radiation dose against a background that has a low contrast.

6.2.4 Nanoparticle dosimetry at therapeutic energies

In a similar fashion as previously described for diagnostic energies at 40 keV, dosimetry experiments were performed at 6 MeV, which lies in the therapeutic x-ray energy range. In these experiments, T_1 and T_2 values of ca. 30 mg/mL samples of (doped) citrate-capped CaF_2 NPs were measured and the samples were exposed to 6 MeV radiation, with the beam optimized to deliver 500 Gy to the sample, after attenuation by the glass ca. 490 Gy is delivered into the dispersion. Then $1/T_1$ and $1/T_2$ were measured again. The same experiments were performed on CaF_2 and the CaF_2 background was subtracted, in the same fashion as shown in the 40 keV experiments.

The results measured in T_1 and T_2 are shown for $CaF_2:Eu^{3+}$ in Figure 6.8 (red). The effect of Eu^{3+} on T_1 is very low, whereas the effect on T_2 is higher. This corresponds well to what was previously observed for Eu^{3+} relaxation times before irradiation. A drop in $1/T_1$ is observed upon irradiation and a minimal change in $1/T_2$ is seen. The observed effect in T_1 may be attributed to a heating effect on the oxygen, causing it to leave the mixture and decrease $1/T_1$.

The effect on T_1 and T_2 upon high-energy irradiation of $CaF_2:Fe^{2+}/Fe^{3+}$ is shown in Figure 6.8 (blue). Here, a rise in $1/T_1$ is observed after irradiation with 6 MeV. A small rise in $1/T_2$ is seen as well. These effects, albeit small, can be attributed to oxidation of Fe^{2+} to Fe^{3+} by oxidative species generated in the mixture by the high-energy x-rays. An explanation for the increased effect in T_1 compared to the effect in T_2 is that the oxidation takes place at the surface of the NPs. Surface species have a stronger effect on T_1, due to the shorter distances at which the relaxivity interactions take place. T_2 scales with the total magnetization of the nanoparticle, which is expected not to change as much if only the surface Fe^{2+} ions are oxidized to Fe^{3+}. The initial value of $1/T_2$ appears lower than that of the $CaF_2:Eu^{3+}$ sample, even though the magnetic moments of high spin Fe^{2+} (4.9 μ_B) and Fe^{3+} (5.9 μ_B) are both higher than that of Eu^{3+} (3.4 μ_B). This corresponds well with the ICP-MS results confirming that Fe^{2+}/Fe^{3+} is present in lower concentrations inside the CaF_2 lattice.

As a control, the same experiments were performed on $CaF_2:Y^{3+}$, the results are shown in Figure 6.8 (black). $CaF_2:Y^{3+}$ $1/T_1$ values appear in the negative at small deviations from zero, due to subtraction of the slightly more positive CaF_2 relaxivities. This effect is similar to the difference observed at 40 keV, and likely the result of a small difference in NP concentration. The initial $1/T_1$ and $1/T_2$ were minimal compared to the other samples. Any effect of the radiation on the relaxivities is minimal as well, indicating that the lattice distortion caused by the ions is not responsible for the T_1 and T_2 effects.

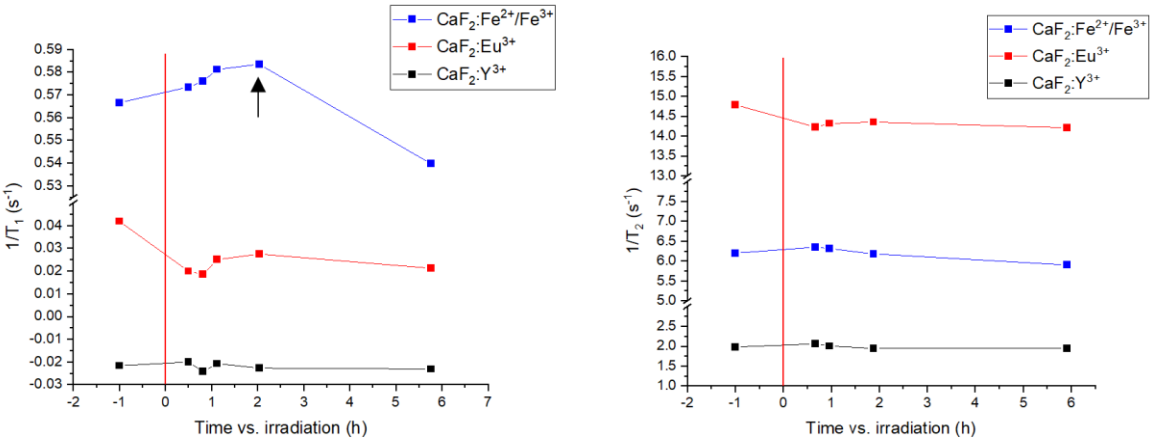

Figure 6.8: Measured and background corrected $1/T_1$ of doped CaF_2 NPs (left), and the $1/T_2$ (right). The results are shown with respect to the irradiation event at 0 (red divider), at which point samples were exposed to 6 MeV radiation. A break in the y-axis is used to show the relative changes in the data better.

The effects of high-energy radiation on the $1/T_1$ and $1/T_2$ values of CaF_2 NPs doped with Eu^{3+} and those doped with Fe^{2+}/Fe^{3+} seem different when compared to the results using 40 keV ionizing radiation. A possible explanation for this difference is that instead of being reduced from the (III) to (II) oxidation state by generation of a photo-electron, the oxidative species generated by the ionizing radiation in water leads to oxidation from the (II) to (III) oxidation state. High-energy x-rays (in the MeV range) primarily interact with matter via Compton scattering.[29] Ionization via Compton scattering leads to formation of reactive oxidative species in water, such as hydroxyl radicals and hydrogen peroxide.[34] These can oxidize Fe^{2+} to Fe^{3+}, resulting in an increase in relaxivities.

The delivered dose of 490 Gy resulted in a T_1 relaxation rate rise of ca. 0.02 s^{-1}. With respect to pure water this corresponds to a relaxation time drop of ca. 5.5%, which is above

the uncertainty in a T_1 measurement.[32] In principle, the dose could be scaled down to a level of 200 Gy and still result in a detectable effect, if the effect is linear. This is would be within an order of magnitude of the higher level of doses used in treatment, meaning that these materials are promising for quantitative use at high x-ray energies as well.[35-36]

These results, although not as pronounced as in the 40 keV experiments, appear tentatively promising for CaF_2:Fe^{2+} to measure the amount of oxidative species generated by high-energy x-rays, and as a result function as a measure for the ionizing radiation dose delivered by radiation treatment of tumors. As discussed previously, the content of CaF_2 doped with iron ions is a mixture of Fe^{2+} and Fe^{3+}, and iron is present in a much lower amount in CaF_2:Fe^{2+}/Fe^{3+} than the other dopant ions in their doped systems.

Comparing low and high x-ray energy results, strong evidence was found that at lower x-ray energies a reductive effect of the photo-electrons is predominantly observable, and at high x-ray energies the oxidative effect of oxidative species generated by the x-rays dominates. The reductive effect can be visualized with MRI contrast using a Eu^{3+}-doped CaF_2 NP, in which the reduction to Eu^{2+} leads to increased relaxivities. The oxidative effect can be visualized with Fe^{2+}-doped CaF_2 NPs, in which oxidation to Fe^{3+} leads to increased relaxivities.

Although proof has been shown that the concept works at both the low- and the high-energy range of x-rays, it is clear that these nanoparticles need to be optimized for the dosimetry effect, and ultimately, for use in the clinic. To use these NPs in the clinic, they

have to be stable after injection so they do not decompose inside the body or have unwanted interactions with proteins, and be potentially labeled with antibodies to ensure target-specificity. For optimization of the dosimetry effect for high-energy x-rays, the synthesis procedure will need to be adapted to maximize Fe^{2+} content and minimize Fe^{3+}, which will in turn maximize the effect of relaxivity change upon oxidation. CaF_2 was found not to be an ideal candidate for the Fe^{2+} host material, as only a small amount of the Fe^{2+} used in the synthesis was incorporated in the CaF_2 lattice, and part of that was converted to Fe^{3+}. At low x-ray energies, the dosimetry effect is very pronounced in CaF_2:Eu^{3+}. The material could in principle be optimized by maximizing Eu^{3+} content and localization at the NP surface to enhance the T_1 effect, while ensuring the host material generates as many photo-electrons as possible at these x-ray energies.

6.2.5 Dosimetry with dose-invariant $NaDyF_4$

In order to use the proposed dose-sensitive materials inside the human body, a signal is necessary to locate them. In particular the CaF_2:Eu^{3+} does not have a strong contrast in T_1 or T_2. For accurate location of the nanoparticles inside the body, a dose-invariant material counterpart with a strong contrast is suggested. Here, a demonstration is given of the effect of introducing $NaDyF_4$ NPs capped with DSPE-mPEG phospholipids[37] before exposing the mixture to 40 keV ionizing radiation. $NaDyF_4$ has been reported to be a strong T_2 contrast agent, with a minimal signal in T_1.[38-39] Furthermore, the oxidation state of the Dy^{3+} ion in the $NaDyF_4$ NPs is expected to be highly stable, and unlikely to reduce or oxidize in the same way as was observed for Eu^{3+} and Fe^{2+}/Fe^{3+}. This would ensure that the magnetic properties wouldn't change in the same way upon x-ray interaction.

Figure 6.9 shows in columns the $1/T_1$ and $1/T_2$ values measured before and after 40 keV irradiation of a dispersion of pure citrate-capped $CaF_2:Eu^{3+}$ NPs, and of a mixture of the Eu^{3+}-doped NPs and $NaDyF_4$ NPs. The difference in relaxivity in the presence of $NaDyF_4$ is indicated above the columns. In $1/T_2$, it is seen that the presence of $NaDyF_4$ increases strongly the measured $1/T_2$, while the $1/T_1$ is almost identical comparing the pure $CaF_2:Eu^{3+}$ NP dispersion to the mixture of NPs. The strong change in T_2 upon $NaDyF_4$ addition is expected as $NaDyF_4$ is a good T_2 contrast agent. A very strong rise in $1/T_1$ and a rise in $1/T_2$ are observed after irradiation for both samples. This effect is attributed to reduction of Eu^{3+} to Eu^{2+}, as previously discussed. The difference in $1/T_2$ in the presence of $NaDyF_4$ versus pure $CaF_2:Eu^{3+}$ is not strongly affected by the radiation dose, as expected from the very stable oxidation state of Dy^{3+}. A small difference is still observed in the relative change of $1/T_1$ and $1/T_2$ when $NaDyF_4$ NPs are present, but it is expected that this effect can be buffered out when $NaDyF_4$ is present in larger amounts, so that the T_2 effect of $CaF_2:Eu^{3+}$ becomes insignificantly small by comparison.

The observation that the change in relaxation time upon irradiation is barely effected by the presence of $NaDyF_4$, together with the strong detectable signal of $NaDyF_4$ in $1/T_2$, is highly promising for the use of $NaDyF_4$ NPs as a dose-invariant control, in conjunction with the dose-sensitive $CaF_2:Eu^{3+}$. The $NaDyF_4$ material can be co-injected with the dose-sensitive NPs, or in the nanoparticle synthesis used as a core over which the $CaF_2:Eu^{3+}$ can be grown as a shell. If $NaDyF_4$ is present as a core for the dose-sensitive core/shell NP like this, the core size can be optimized for the $NaDyF_4$ T_2 effect to be sufficiently large to buffer out the $CaF_2:Eu^{3+}$ T_2 effect.

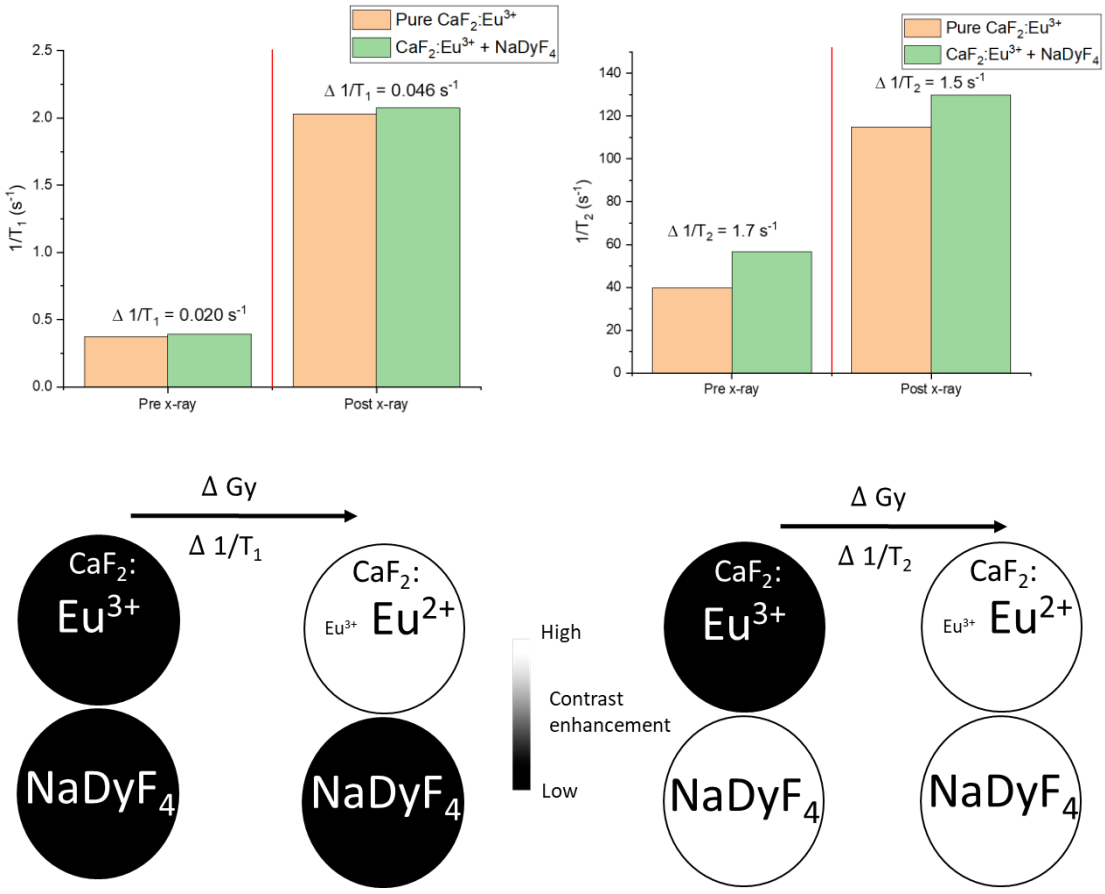

Figure 6.9: $1/T_1$ (left) and $1/T_2$ (right) of pure $CaF_2:Eu^{3+}$ in H_2O dispersion (orange column) and in the presence of $NaDyF_4$ NPs (green column). The samples were irradiated with 40 keV x-rays at h = 0 (red divider). Shown underneath are schematic representations of the change in contrast enhancement effects of the nanoparticles in dispersion.

6.3 Conclusions

The successful synthesis of CaF_2 NPs doped with a variety of dopant ions was reported, and their response to ionizing radiation at both diagnostic and therapeutic energies demonstrated using T_1 and T_2 MRI contrasts. CaF_2, $CaF_2:Fe^{2+}/Fe^{3+}$, $CaF_2:Y^{3+}$, and $CaF_2:Eu^{3+}$ NPs were synthesized, and successful synthesis was demonstrated with TEM

and XRD. The oxidation state of Fe in CaF_2 was confirmed with Mössbauer spectroscopy to be a mixture of (II) and (III), and the oxidation state of Eu was confirmed to be (III). The presence of Eu^{3+} in the NPs was further confirmed with photoluminescence emission spectroscopy. $1/T_1$ and $1/T_2$ were determined for dispersions of CaF_2, CaF_2:Fe^{2+}/Fe^{3+}, CaF_2:Y^{3+}, and CaF_2:Eu^{3+} NPs in H_2O before, and at several time-points after 40 keV radiation exposure. CaF_2 and CaF_2:Y^{3+} showed merely a small rise in $1/T_1$ and $1/T_2$, attributed to oxygen leaving the system. CaF_2:Eu^{3+} showed a strong rise in $1/T_1$ and a rise in $1/T_2$ after irradiation, that scaled with the irradiation time. CaF_2:Fe^{2+}/Fe^{3+} showed a sharp drop after irradiation. The values recovered over time after x-ray exposure. These results were explained by photo-electrons generated by ionizing radiation reducing Eu^{3+} to Eu^{2+} and Fe^{3+} to Fe^{2+}. Further evidence for this explanation is provided using emission spectroscopy of Eu^{3+}, where the Eu^{3+} emission would decrease upon x-ray exposure, followed by recovery. The observed changes in $1/T_1$ and $1/T_2$ were positive for CaF_2:Fe^{2+}/Fe^{3+} at 6 MeV radiation, which was explained by oxidation of the ions from Fe^{2+} to Fe^{3+} by oxidative species generated by the ionizing radiation. Based on these results CaF_2:Eu^{3+} is a better candidate for a dosimeter NP at low energies, due to it turning on as a MRI contrast agent upon photo-electron interaction, and CaF_2:Fe^{2+} at high x-ray energies, as it turns on upon interaction with oxidative species generated. The signal increase at high 6 MeV was low, however, indicating the need for a material optimization. The use of a dose-invariant control was demonstrated by showing that the presence of T_2 contrast agent $NaDyF_4$ NPs did not affect the relaxivity change upon radiation at 40 keV. The results seem promising for use of dose-sensitive contrast agents to measure radiation dose during diagnostics and therapy utilizing ionizing radiation.

6.4 Experimental methods

Chemicals. Iron(II) chloride tetrahydrate (>99%), dysprosium(III) chloride hexahydrate (99.99%), yttrium(III) chloride hexahydrate (99.99%), europium(III) chloride hexahydrate (99.99%), ammonium fluoride (99.99%), tech grade oleic acid (90%), tech grade 1-octadecene (ODE, 90%), dimethyl sulfoxide (DMSO), toluene, and hexanes were purchased from Sigma-Aldrich. Deionized water from a water purifier (18.2 MΩ) was used. Anhydrous ethanol from Commercial Alcohols, methanol from Caledon, and sodium hydroxide from Bio basic Canada Inc. were used. 1,2-distearoyl-*sn*-glycero-3-phosphoethanolamine-*N*-[methoxy(polyethylene glycol)-2,000 (DSPE-mPEG) was bought from Avanti.

CaF_2 NP synthesis. Charge stabilized CaF_2 nanoparticles were made by dissolving 0.290 mg NH_4F in methanol. This solution was heated to 70 °C and a solution of 0.490 mg $CaCl_2$ in 15 mL methanol was added dropwise, forming a white precipitate. The mixture was refluxed at 70 °C for two hours. After this, the mixture was allowed to cool to room temperature. It was transferred to a centrifuge tube and centrifuged for 10 min. at 8,600 g. The supernatant was discarded and the sediment redispersed in 30 mL H_2O. For the doped nanocrystals, synthesis was the same except 1 mmol $FeCl_2$, YCl_3, or $EuCl_3$ was added in methanol solution together with the $CaCl_2$.

In a typical synthesis to fabricate citrate-stabilized CaF_2 nanoparticles in H_2O, 2.0 g citric acid and 100 mg NH_4F and 1.0 g NaOH were added to 80 mL H_2O in a 100 mL round-bottom flask. The mixture was stirred at a moderate pace to allow a small dip in the surface

center. The mixture was heated to 75 °C using a heating mantle. At this temperature, a solution of 1 mmol $CaCl_2$ was added dropwise. The mixture was left to stir at 75 °C for 2 hours before removing the heating mantle, allowing it to cool to room temperature. The nanoparticles were washed by adding 120 mL EtOH and centrifuging at 8,600 g for 15 minutes. The supernatant was discarded and the white sediment dispersed in 10 mL H_2O.The synthesis of the doped nanoparticles was identical, except 0.2 mmol CaF_2 was substituted for 0.2 mmol $FeCl_2$, YCl_3, or $EuCl_3$.

$NaDyF_4$ NP synthesis. In the $NaDyF_4$ NP preparation, 1 mmol $DyCl_3$•6(H_2O) was introduced into a 100 mL three neck round-bottom flask and 17 mL 1-Octadecene and 3 mL oleic acid were added. The mixture was stirred at a moderate pace, so that the surface of the liquid remained level. This was then heated with a heating mantle to 140 °C over 30 minutes under vacuum, before keeping it at that temperature for 1 hour. The mixture turned clear. This was cooled to 60 °C over 15 minutes and a solution of 10 mL methanol with 2.5 mmol NaOH and 4 mmol NH_4F was introduced dropwise. The resulting mixture was heated at 70 °C until methanol had evaporated, which was after ca. 30 min. The mixture was then heated to 275 °C over 15 min. The temperature was kept at 275 °C for 2 hours. Then the heating mantle was removed and the mixture was allowed to cool to room temperature. To the mixture 30 mL ethanol was added in a centrifugation tube and this was centrifuged at 3,000 g for 10 min. The resulting supernatant was discarded and the white sediment at the bottom was redispersed in 20 mL hexanes.

$NaDyF_4$ NPs were transferred to H_2O *via* a dual solvent exchange method. 1 mg NPs in 1 mL of toluene was added to 10 mg DSPE-mPEG. 4 mL DMSO was added dropwise. The mixture was shaken gently on a shake-plate for 1 hour. Toluene was evaporated under a rotavap at room temperature over ca. 1 hour. The solvent was exchanged for water by filtering through 50k MWCO centrifuge filtration tube, centrifuging at 2,600 g for 30 min., then adding 15 mL H_2O. The centrifugation was step was repeated two times and the final volume of the filtrate increased to 1 mL H_2O.

Characterization. Using a JEOL JEM-1400 microscope operating at 80 kV Transmission electron microscopy images were obtained. Water dispersions of the NPs were drop-cast on a formvar carbon-coated grid (300 mesh Cu) and air-dried over 2 hours before imaging. X-ray diffractograms with a resolution of 0.0263 °(2θ) were collected using a PANalytical Empyrean X-ray System with a Cu source (Kα radiation, $\lambda = 1.54060$ Å) operating at 45 kV and 40 mA. ICP-MS elemental analysis was performed in triplicate using an Agilent 8800 operated with O_2 Reaction Cell Gas in MS/MS mode.

Fluorescence emission spectroscopy. Emission spectroscopy was performed with 394 nm light from a xenon lamp light source using a monochromator. Emission was measured and corrected for instrument response using a cooled Hamamatsu R928P PMT between 550 and 750 nm. Counts were integrated for 1 s at every 1 nm step using a 1 nm slit width. The detector was positioned at a 90-degree angle with respect to the excitation source. A 395 nm long-pass filter was placed between the sample and the detector.

Dosimetry experiments at 40 keV. In a typical dosimetry experiment a dispersion of 20 mg/mL nanoparticles was introduced into an NMR 1 mm diameter insert tube. The insert tube was placed inside a normal NMR tube with $CDCl_3$.

Proton relaxation times were determined using an NMR at 11.7 T. T_1 values were measured with an inverse recovery sequence, T_2 values were measured with a CPMG sequence. Proton NMR spectra were analyzed by integrating and plotting the H_2O peak at varying delay times. The generated plots were fitted with a mono-exponential decay function to determine T_1 and T_2.

After determining relaxation times, the insert tube with the NP dispersion was placed in front of a W x-ray source operated at 40 kV and 40 mA. The slit width of the x-ray source was about 1 cm in diameter and both the top and the bottom part of the insert tube were irradiated. Irradiation was done for a total of 6 min., 15 min., and 30 min. Corresponding radiation doses delivered inside the NMR tube were calculated using Monte Carlo simulations.

Right after irradiation T_1 and T_2 were determined again in the way described previously, as well as 22 hours later.

Dosimetry using spectroscopy with $CaF_2:Eu^{3+}$ NPs was done in exactly the same way, except the fluorescence emission spectroscopy was performed as described previously instead the relaxation time determination.

Dosimetry experiments at 6 MeV. Dosimetry at 6 MeV was performed in a similar way to 40 keV, except an MRI operated at 9.4 T was used to determine relaxation times. T_1 was determined using a RARE sequence and T_2 using a MSME sequence.

After relaxation time determination, the NP dispersion was placed under a 6 MeV x-ray source delivering a dose of 500 Gy. For this, the samples were placed in RW3 (PTW, Germany) water equivalent phantom at the depth of the maximum dose of 6MV FFF photon beam generated using True Beam (Varian, Palo Alto) linear accelerator. To maximize the dose rate and limit the number of monitor units needed to deliver the prescribed dose of 500 Gy the source-to-phantom distance was set to 60 cm. A square 30 × 30 cm^2 radiation field was directed perpendicularly to a phantom surface. Calculations of an adequate number of monitor units required to deliver the prescribed dose were based on dose rate measurements under described conditions.

Attenuation of the glass was calculated using mass attenuations of SiO_2 and H_2O and the Beer-Lambert law, to give an approximation of the delivered dose inside the phantoms.

After dose delivery, T_1 and T_2 were measured again, at several time points after radiation.

6.5 References

1. Fleischmann, D.; Boas, F. E., Computed Tomography—Old Ideas and New Technology. *Eur. Radiol.* **2011,** *21*, 510-517.
2. Kalender, W. A., X-Ray Computed Tomography. *Phys. Med. Biol.* **2006,** *51*, R29.
3. Smith-Bindman, R., Is Computed Tomography Safe. *N. Engl. J. Med.* **2010,** *363*, 1-4.
4. Baskar, R.; Dai, J.; Wenlong, N.; Yeo, R.; Yeoh, K.-W., Biological Response of Cancer Cells to Radiation Treatment. *Front. Mol. Biosci.* **2014,** *1*, 24.
5. Cox, J. D., Toxicity Criteria of the Radiation Therapy Oncology Group (RTOG) and the European Organization for Research and Treatment of Cancer (EORTC). *IJROBP* **1995,** *31*, 1341-1346.
6. Taylor, M. L.; Kron, T., Consideration of the Radiation Dose Delivered Away from the Treatment Field to Patients in Radiotherapy. *J. Med. Phys.* **2011,** *36*, 59-71.
7. Baskar, R.; Lee, K. A.; Yeo, R.; Yeoh, K.-W., Cancer and Radiation Therapy: Current Advances and Future Directions. *Int. J. Med. Sci.* **2012,** *9*, 193-199.
8. Tannock, I. F., Treatment of Cancer with Radiation and Drugs. *J. Clin. Oncol.* **1996,** *14*, 3156-3174.
9. Ahnesjö, A.; Aspradakis, M. M., Dose Calculations for External Photon Beams in Radiotherapy. *Phys. Med. Biol.* **1999,** *44*, R99-R155.
10. O'Keeffe, S.; McCarthy, D.; Woulfe, P.; Grattan, M.; Hounsell, A.; Sporea, D.; Mihai, L.; Vata, I.; Leen, G.; Lewis, E., A Review of Recent Advances in Optical Fibre Sensors for in Vivo Dosimetry During Radiotherapy. *Br. J. Radiol.* **2015,** *88*, 20140702.

11. Saini, A. S.; Zhu, T. C., Dose Rate and Sdd Dependence of Commercially Available Diode Detectors. *Med. Phys.* **2004,** *31*, 914-924.

12. Beyer, G. P.; Mann, G. G.; Pursley, J. A.; Espenhahn, E. T.; Fraisse, C.; Godfrey, D. J.; Oldham, M.; Carrea, T. B.; Bolick, N.; Scarantino, C. W., An Implantable MOSFET Dosimeter for the Measurement of Radiation Dose in Tissue During Cancer Therapy. *IEEE Sens. J.* **2008,** *8*, 38-51.

13. Mijnheer, B.; Beddar, S.; Izewska, J.; Reft, C., In Vivo Dosimetry in External Beam Radiotherapy. *Med. Phys.* **2013,** *40*, 070903.

14. Essers, M.; Mijnheer, B., In Vivo Dosimetry During External Photon Beam Radiotherapy. *Int. J. Radiat. Oncol. Biol. Phys.* **1999,** *43*, 245-259.

15. Izewska, J.; Andreo, P., The IAEA/WHO TLD Postal Programme for Radiotherapy Hospitals. *Radiother. Oncol.* **2000,** *54*, 65-72.

16. Izewska, J.; Hultqvist, M.; Bera, P., Analysis of Uncertainties in the IAEA/WHO TLD Postal Dose Audit System. *Radiat. Meas.* **2008,** *43*, 959-963.

17. Blamire, A. M., The Technology of MRI — the Next 10 Years? *Br. J. Radiol.* **2008,** *81*, 601-617.

18. Hahn, M. A.; Singh, A. K.; Sharma, P.; Brown, S. C.; Moudgil, B. M., Nanoparticles as Contrast Agents for in-Vivo Bioimaging : Current Status and Future Perspectives. *Anal. Bioanal. Chem.* **2011**, 3-27.

19. Na, H. B.; Song, I. C.; Hyeon, T., Inorganic Nanoparticles for MRI Contrast Agents. *Adv. Mater.* **2009,** *21*, 2133-2148.

20. Caravan, P.; Tóth, É.; Rockenbauer, A.; Merbach, A. E., Nuclear and Electronic Relaxation of Eu^{2+}(aq): An Extremely Labile Aqua Ion. *J. Am. Chem. Soc.* **1999,** *121*, 10403-10409.

21. Garcia, J.; Kuda-Wedagedara, A. N. W.; Allen, M. J., Physical Properties of Eu^{2+}-Containing Cryptates as Contrast Agents for Ultrahigh-Field Magnetic Resonance Imaging. *Eur. J. Inorg. Chem.* **2012,** *2012*, 2135-2140.

22. Miao, Y.; Xie, F.; Cen, J.; Zhou, F.; Tao, X.; Luo, J.; Han, G.; Kong, X.; Yang, X.; Sun, J., Fe^{3+}@ Polydopa-B-Polysarcosine, a T_1-Weighted MRI Contrast Agent Via Controlled NTA Polymerization. *ACS Macro Lett.* **2018,** *7*, 693-698.

23. Zhang, P.; Hou, Y.; Zeng, J.; Li, Y.; Wang, Z.; Zhu, R.; Ma, T.; Gao, M., Coordinatively Unsaturated Fe^{3+} Based Activatable Probes for Enhanced MRI and Therapy of Tumors. *Angew. Chem. Int. Ed.* **2019,** *58*, 11088-11096.

24. Wang, J.; Wang, Z.; Li, X.; Wang, S.; Mao, H.; Li, Z., Energy Transfer from Benzoic Acid to Lanthanide Ions in Benzoic Acid-Functionalized Lanthanide-Doped CaF_2 Nanoparticles. *Appl. Surf. Sci.* **2011,** *257*, 7145-7149.

25. Sudarsan, V.; Sivakumar, S.; van Veggel, F. C. J. M.; Raudsepp, M., General and Convenient Method for Making Highly Luminescent Sol-Gel Derived Silica and Alumina Films by Using LaF_3 Nanoparticles Doped with Lanthanide Ions (Er^{3+}, Nd^{3+}, and Ho^{3+}). *Chem. Mater.* **2005,** *17*, 4736-4742.

26. Shannon, R., Revised Effective Ionic Radii and Systematic Studies of Interatomic Distances in Halides and Chalcogenides. *Acta Crystallogr. A* **1976,** *32*, 751-767.

27. Cantelar, E.; Sanz-García, J. A.; Sanz-Martin, A.; Santiuste, J. E. M.; Cussó, F., Structural, Photoluminescent Properties and Judd-Ofelt Analysis of Eu^{3+}-Activated CaF_2 Nanocubes. *J. Alloys Compd.* **2020,** *813*, 152194.

28. Patterson, A., The Scherrer Formula for X-Ray Particle Size Determination. *Phys. Rev.* **1939,** *56*, 978-982.

29. Turner, J. E., Interaction of Ionizing Radiation with Matter. *Health Phys.* **2005,** *88*, 520-544.

30. Huang, B.; Law, M. W.-M.; Khong, P.-L., Whole-Body PET/CT Scanning: Estimation of Radiation Dose and Cancer Risk. *Radiology* **2009,** *251*, 166.

31. Alaei, P.; Spezi, E., Imaging Dose from Cone Beam Computed Tomography in Radiation Therapy. *Phys. Med.* **2015,** *31*, 647-658.

32. Polders, D. L.; Leemans, A.; Luijten, P. R.; Hoogduin, H., Uncertainty Estimations for Quantitative in Vivo MRI T_1 Mapping. *J. Magn. Reson.* **2012,** *224*, 53-60.

33. Deoni, S. C., Quantitative Relaxometry of the Brain. *Top. Magn. Reson. Imaging* **2010,** *21*, 101-113.

34. Riley, P., Free Radicals in Biology: Oxidative Stress and the Effects of Ionizing Radiation. *Int. J. Radiat. Biol.* **1994,** *65*, 27-33.

35. Osti, M.; Agolli, L.; Valeriani, M.; Reverberi, C.; Bracci, S.; Marinelli, L.; De Sanctis, V.; Cortesi, E.; Martelli, M.; De Dominicis, C., 30 Gy Single Dose Stereotactic Body Radiation Therapy (SBRT): Report on Outcome in a Large Series of Patients with Lung Oligometastatic Disease. *Lung Cancer* **2018,** *122*, 165-170.

36. Chan, S.; Dhadda, A.; Swindell, R., Single Fraction Radiotherapy for Small Superficial Carcinoma of the Skin. *Clin. Oncol.* **2007,** *19*, 256-259.

37. Tong, S.; Hou, S.; Ren, B.; Zheng, Z.; Bao, G., Self-Assembly of Phospholipid - PEG Coating on Nanoparticles through Dual Solvent Exchange. *Nano Lett.* **2011,** *11*, 3720-3726.

38. Das, G. K.; Johnson, N. J. J.; Cramen, J.; Blasiak, B.; Latta, P.; Tomanek, B.; van Veggel, F. C. J. M., $NaDyF_4$ Nanoparticles as T_2 Contrast Agents for Ultrahigh Field Magnetic Resonance Imaging. *J. Phys. Chem. Lett.* **2012,** *3*, 524-529.

39. Zhang, X.; Blasiak, B.; Marenco, A. J.; Trudel, S.; Tomanek, B.; van Veggel, F. C. J. M., Design and Regulation of $NaHoF_4$ and $NaDyF_4$ Nanoparticles for High-Field Magnetic Resonance Imaging. *Chem. Mater.* **2016,** *28*, 3060-3072.

Chapter 7: Utilizing T_1- and T_2-Specific Contrast Agents as the "Two Colors" in Correlation MRI

Based on:

Frencken, A. L.; Blasiak, B.; Kruk, D.; Tomanek, B.; van Veggel, F. C. J. M., Utilizing T_1- and T_2-Specific Contrast Agents as the "Two Colors" in Correlation MRI. *To be submitted.*

MRI measurements were performed by Barbara Blasiak (UCalgary).

Abstract

Due to its non-invasive nature, high spatial contrast, and near limitless depth of penetration, magnetic resonance imaging (MRI) has become one of the most widely used medical diagnosis techniques. Several different modalities can be used to image using MRI, most notable of which are T_1 (spin-lattice) and T_2 or T_2* (spin-spin) water proton relaxation times. For these modalities, chemical contrast agents (CAs) have been developed that enhance locally the contrasts in the image. In this chapter, a method is presented to combine T_1- and T_2- specific contrast agents in a single imaging technique, referred to as correlation MRI. This allows, for instance, multiple contrast agents to be used in conjunction to attain locally even higher sensitivity, or to use them to visualize contrast between multiple types of tissue in the same image. A major obstacle for the quantitative use of correlation MRI is that T_1 and T_2 relaxivity changes generated by the contrast agents are not fully linearly additive, and in other words, not fully independent of each other. In this chapter, the regions are mapped out where commercially used contrast agents Magnevist (based on Gd^{3+}, primarily a T_1 CA) and Feridex (based on Fe^{2+} and Fe^{3+}, primarily a T_2 CA) follow, and deviate from, theoretically predicted T_1 and T_2 values, based on their concentrations. It was found that in concentrations relevant to the clinic, T_1 and T_2 of the CA mixtures strongly deviates from linearly added values. Based on these results, a 3-dimensional calibration graph is proposed to determine quantitatively the concentration in mixtures of CAs, based on the measured T_1 and T_2 values. The calibration method is essential for the use of multiple contrast modalities in correlation MRI imaging.

7.1 Introduction

Since its first demonstration in 1977, magnetic resonance imaging (MRI) has seen wide widespread use as a medical imaging technique.[1-2] In MRI, images are typically made by spatially mapping out proton spin relaxation times in a gradient external magnetic field.[2] Advantages of MRI are a high spatial contrast and potentially limitless depth of tissue penetration, all while being non-invasive to the body. A disadvantage of MRI compared with other medical imaging techniques is its low sensitivity. Increasing the sensitivity of MRI has been an outstanding challenge in the field. Strategies to increase the sensitivity include increasing the strength of the applied magnetic field,[3-4] and utilizing chemical contrast agents (CAs) that enhance locally the MRI contrast.[5-8]

T_1 and T_2 or T_2* relaxation are common parameters to generate MRI contrast. In T_1-weighted MRI, contrast is derived from relaxation of water proton spin with respect to the external magnetic field, referred to as spin-lattice relaxation time. T_2 and T_2* are derived from relaxation times of water proton spins with respect to the surrounding water proton spins, also referred to as spin-spin relaxation. In addition, T_2* includes the relaxivity of inhomogeneities in the external magnetic field.[9]

Paramagnetic CAs that enhance the local contrast have been developed for T_1- and T_2-weighted MRI. Over the years, contrast agents have been developed that enhance T_1,[10-11] or T_2[12-13] relaxation of water protons. Using these CAs, T_1- and T_2-weighted images can be generated that map accurately the presence of such a CA, showing it contrasting against its surrounding tissue.

The contrast generated by individual CAs is described in equations (1) and (2). Here, the overall relaxation rate (i.e., $1/T_1$ or $1/T_2$) depends on the specific relaxation rate of the contrast agent r_1 or r_2, the concentration of the contrast agent [CA], and the background relaxation rate $1/T_1(0)$ and $1/T_2(0)$. Using these equations, individual CAs can be quantified based on MRI contrast.

$$\frac{1}{T_1} = \frac{1}{T_1(0)} + r_1 * [\mathrm{CA}] \quad (1)$$

$$\frac{1}{T_2} = \frac{1}{T_2(0)} + r_2 * [\mathrm{CA}] \quad (2)$$

The existence of these two modalities in MRI and the potential ability to quantify CAs based on them has served as an inspiration to us and others to develop an MRI contrast correlation technique. Image correlation analysis is applied in a variety of fields and entails the analysis of contrast in multiple images to derive a relationship between two or more parameters. It has been used to combine different modalities in medical imaging techniques,[14-15] and is used in fluorescence correlation microscopy.[16-17] In a similar way, image correlation analysis could potentially be applied to combine different modalities within MRI, leading to a way to visualize both modalities, acting like two different colors. This application has recently started to be explored.[18-21] Ideally, correlation spectroscopy utilizes two different colors that are fully independent of each other, for instance a blue color and a red color with no spectral overlap. In the same fashion, T_1 and T_2 contrast could serve as the "two colors" in MRI correlation. MRI contrast agents exist with a high effect on T_1 and a small effect on T_2 and *vice versa*, but having a pure effect on either modality is theoretically impossible.[22-23]

The imaging technique discussed here combines the imaging of high T_1 and high T_2 contrast agents into an MRI correlation image. The relationship between T_1 and T_2 contrast generated by the contrast agents in the respective T_1- and T_2-weighted images can be analyzed and their correlation imaged. Combining these imaging techniques may lead to visualize phenomena in the body that would not be demonstrable, with high fidelity, using strictly T_1 or T_2. For example, two different tissues may be labeled with T_1 or T_2 contrast agents and their interaction monitored. In this way, a tumor and its surrounding tissue may both be labeled to increase the tumor's definition, or the heterogeneous receptors at a tumor's surface may be labeled with two different contrast agents to outline the full tumor. There is also the clinical interest in the vascularity of tumors, and using two contrast agents, a tumor can be outlined with one CA, and the blood vessels inside with another CA. In addition to these applications, MRI correlation would be of interest to CAs that are used for measurement of a property inside tissue, such as pH or a biomolecule concentration, where the contrast of the CA is variable with what is being measured. Here, correlation can be used to co-introduce a control CA that is independent of the variable being measured, to verify the concentration of CAs at the location of interest. In short, there are many reasons to develop MRI correlation for clinical use, although it is fair to state that we are just at the beginning of this development.

Previous work has been conducted on the MRI correlation concept by Chris A. Flask *et al.* In an *in vivo* demonstration, Gd-BOPTA (gadobenic acid)[24] and Dy-DOTA-azide (dysprosium dodecane tetraacetic acid azide) contrast agents were injected in a mouse

glioma model tumor.[20] Using both T_1- and T_2-weighted MRI, the concentrations of the injected contrast agents in the tumor could be mapped with reasonable accuracy (standard deviations of 10 – 16% in 10 demonstrations). The authors assumed a model where the relaxivity contributions of the contrast agents could be added linearly to arrive at the final measured relaxivity, which they argue to be valid if the two contrast agents have statistically different relaxivity ratios (r_2/r_1). The r_2/r_1 values they used were 374 for Dy-DOTA-azide and 6.59 for Gd-BOPTA with no reported overlap in the uncertainties of the ratios used. The linear model they used is given by equations (3) and (4).

$$\frac{1}{T_1} = \frac{1}{T_1(0)} + r_1 * [\mathrm{CA1}] + r_1 * [\mathrm{CA2}] \quad (3)$$

$$\frac{1}{T_2} = \frac{1}{T_2(0)} + r_2 * [\mathrm{CA1}] + r_2 * [\mathrm{CA2}] \quad (4)$$

The demonstration using linear addition is valid only if all variables are independent of each other. This assumption may not be generally applicable, as the r_1 and r_2 of a specific contrast agent solute are never fully independent of each other.[22-23] Furthermore, interaction of CAs with each other may influence their respective relaxivities as well. It is also expected that deviations from linear behavior are exacerbated at higher magnetic field strengths, due to stronger increases in r_2 relative to r_1.[12, 25] Deviation from this linear model may explain the standard deviations the authors report, which are quite high for a reliable use of the MRI correlation technique.

In this chapter, the validity of this model that linearly adds r_1 and r_2 values to quantify two commercially available contrast agents based on the relaxivities of their mixtures was

tested. We build on the previous demonstration by proposing a calibration model to determine accurately concentrations of two CAs in MRI, to arrive at a reliable MRI correlation technique. The calibration method aims to verify and correct for potential concentration ranges where the respective relaxivities are not linearly additive.

Here, T_1 and T_2 contrast in concentration ranges of the T_1 CA Magnevist (based on a Gd^{3+} multidentate complex) and T_2 CA Feridex (based on iron oxide nanoparticles) are measured, and relaxivities determined. Relaxation times of mixtures of the CAs are measured as well and the validity of linearly added relaxivities was determined by comparison of the experiment with the model. Finally, a calibration curve of the two contrast agents is presented and its use to determine concentrations from T_1 and T_2 combinations is demonstrated.

7.2 Results and discussion

Relaxivities of pure CAs

The commercially available contrast agents Feridex and Magnevist were chosen for the correlation demonstration. Feridex consists of iron oxide nanoparticles stabilized with citrate in water. The iron oxide has a magnetite structure and the average chemical formula $FeO_{1.44}$. The commercially available dispersion contains 11.2 mg/mL iron (0.2 M). Magnevist comprises a solution of gadopentate dimeglumine (Gd-DTPA) at a 0.5 M concentration in water.

T_1 and T_2 of the chosen CAs were first measured individually at 9.4 T. Plotted in Figure 7.1 are the $1/T_1$ and $1/T_2$ values of various concentrations of Feridex. In Figure 7.2, these values are plotted for a concentration range of Magnevist. Using equations (1) and (2), the relaxivities r_1 and r_2 could be determined. The slope of a linear fit to the experimental data results in the respective r_1 and r_2 values. The r_1 and r_2 values for Feridex were 2.10 ± 0.13 and 238.97 ± 8.41 s^{-1} mM^{-1}, respectively. The value for the highest $1/T_2$ value (in Feridex, Figure 7.1 (right)), had a very large uncertainty as a result of being near the detection limit of the MRI in which it was measured. It was therefore not included in the fit.

For Magnevist, the respective r_1 and r_2 values were 4.10 ± 0.19 and 5.20 ± 0.20 s^{-1} mM^{-1}. The r_1 and r_2 values correspond reasonably well to literature values. The r_2 of Feridex was reported as 307 s^{-1} mM^{-1} at 9.4 T,[26] the r_1 of Magnevist as 3.2 s^{-1} mM^{-1} at 9.4 T.[27] The r_1 value of Feridex and r_2 value of Magnevist were found for 4.7 T, at 2.3 and 4.0 s^{-1} mM^{-1}, respectively.[25]

The r_2/r_1 ratios were calculated to be $r_2/r_1 = 113.8 \pm 8.3$ for Feridex, and $r_2/r_1 = 1.27 \pm 0.07$ for Magnevist. The ratio of Feridex is 89.7 times higher than that of Magnevist. This relative difference in r_2/r_1 ratios compares favorably to the difference demonstrated in the dual contrast work of Chris A. Flask *et al.*,[19] who measured $r_2/r_1 = 374$ for Dy-DOTA-azide and $r_2/r_1 = 6.59$ for Gd-BOPTA, the relative difference they report being only 56.8 times higher for the Dy-DOTA-azide. Besides the clinical relevancy, the choice of Magnevist and Feridex seems to result in a larger difference of r_2/r_1 values. The larger relative difference would mean that the linear model should be more reliable, due to a smaller

chance of overlap in r_2/r_1 errors of the CAs. However, all the CAs discussed have r_2 values higher than r_1, and even the Magnevist we measured is not a "pure" T_1 contrast agent. In this way, the observation was made that even the combination of a high T_1 and a high T_2 CA cannot be used as a pair of two pure colors that have no overlap in contrast.

The $1/T_1(0)$ and $1/T_2(0)$ values were determined from the intercept of the fit with the y-axes, resulting in values of $1/T_1(0)$: $0.67 \pm 0.17\ s^{-1}$ and $1/T_2(0)$: $19.47 \pm 4.14\ s^{-1}$ for Feridex. $1/T_1(0)$: $1.69 \pm 0.34\ s^{-1}$ and $1/T_2(0)$: $3.05 \pm 0.16\ s^{-1}$ were found for Magnevist. These values appear to vary strongly between contrast agents. A possible reason for the variation in $T_1(0)$ and $T_2(0)$ is the effect of the CA solute on the solubility of O_2 and CO_2 in the water, making the background signal not fully independent of the T_1 and T_2 measured from the CA. Averaging the values between CAs resulted in $1/T_1(0)$: $1.18 \pm 0.19\ s^{-1}$ and $1/T_2(0)$: $11.26 \pm 2.08\ s^{-1}$. As an alternative to the average of the y-intercepts, the relaxivity of pure water can be taken as well, to use as $1/T_1(0)$ and $1/T_2(0)$ in equations (3) and (4). The T_1 and T_2 of distilled water were measured, and $1/T_1$ determined to be $0.3687 \pm 0.0004\ s^{-1}$, and $1/T_2$ to be $2.3474 \pm 0.0110\ s^{-1}$. The relaxation rates of pure water are expectedly very low, due to lack of any magnetic solutes.[7] By comparison, the $1/T_1(0)$ and $1/T_2(0)$ values calculated from y-intercepts of the pure CA plots are higher than expected for pure water, and show variance between those determined for Feridex and for Magnevist, especially in $1/T_2$, resulting in a larger relative uncertainty. For the demonstration of the linear model in this chapter, both the pure water relaxivities and y-intercept averages from pure CA curves were used, as described later in this chapter.

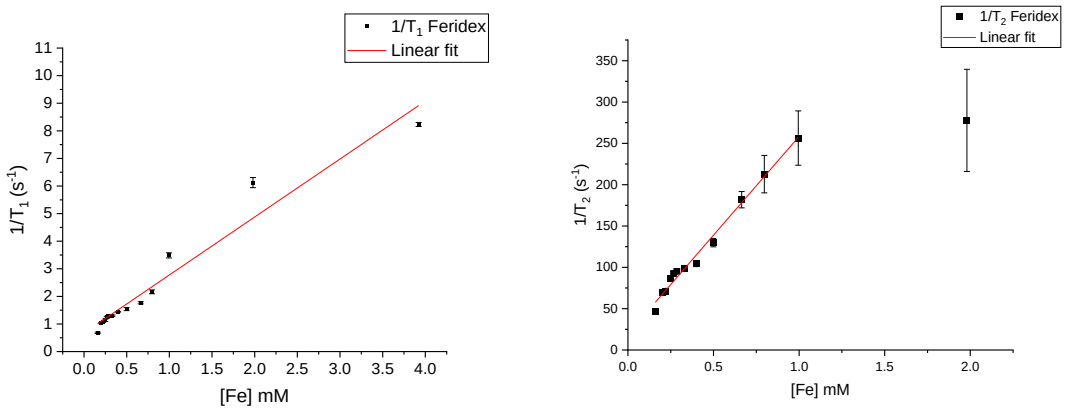

Figure 7.1: Measured $1/T_1$ (left) and $1/T_2$ (right) of Feridex at various concentrations.

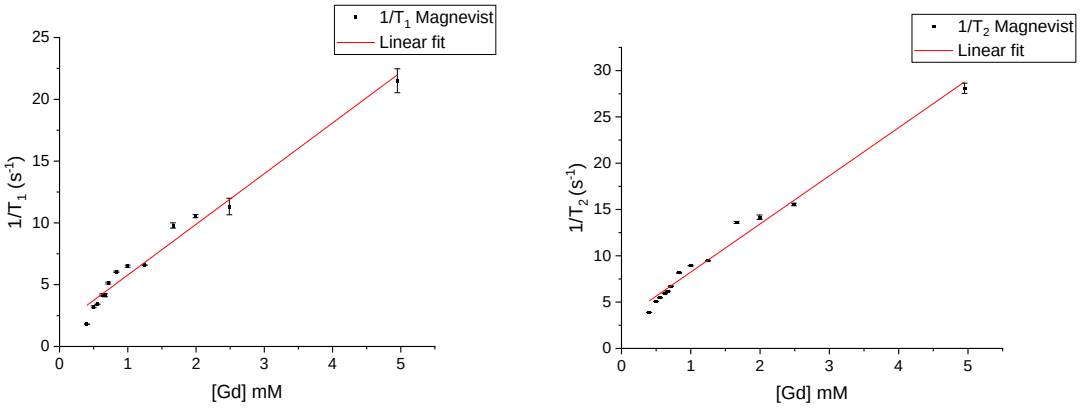

Figure 7.2: Measured $1/T_1$ (left) and $1/T_2$ (right) of Magnevist at various concentrations.

Relaxivities of mixtures of CAs

A series of mixtures of Feridex and Magnevist was prepared and T_1 and T_2 were measured of these mixtures. 3-Dimensional plots were made showing the measured $1/T_1$ (Figure 7.3) and $1/T_2$ (Figure 7.4) for the mixtures of varying concentrations Feridex and Magnevist.

Using the proposed equations (3) and (4) and thus assuming completely linear behavior, analytically predicted T_1 and T_2 values of the mixtures were calculated. For $1/T_1(0)$ and

$1/T_2(0)$, the relaxivities of distilled water were used, resulting in $1/T_1(0) = 0.3687 \pm 0.0004\ s^{-1}\ mM^{-1}$ and $1/T_2(0) = 2.3474 \pm 0.0110\ s^{-1}\ mM^{-1}$. In an alternative approach, a similar comparison was done using an average of the $1/T_1(0)$ calculated from the y-intercepts of the pure CA $1/T_1$ plots, and an average of the $1/T_2(0)$ from averaging the y-intercepts of the pure CA $1/T_2$ plots. The results of this alternative method are shown in Appendix III. The results using the $1/T_1(0)$ and $1/T_2(0)$ determined from pure water have a smaller relative error and showed a closer similarity overall, resulting in a more conservative model for relaxivities based on CA concentration.

The calculated results were compared to the experimentally determined T_1 and T_2 of mixtures at corresponding concentrations in Figures 7.3 and 7.4. In these Figures, it can be seen that the calculated values do not fully overlap with the measured ones. In particular, the higher concentrations of Feridex in the T_2 measurements correspond with a large deviation from the predicted value.

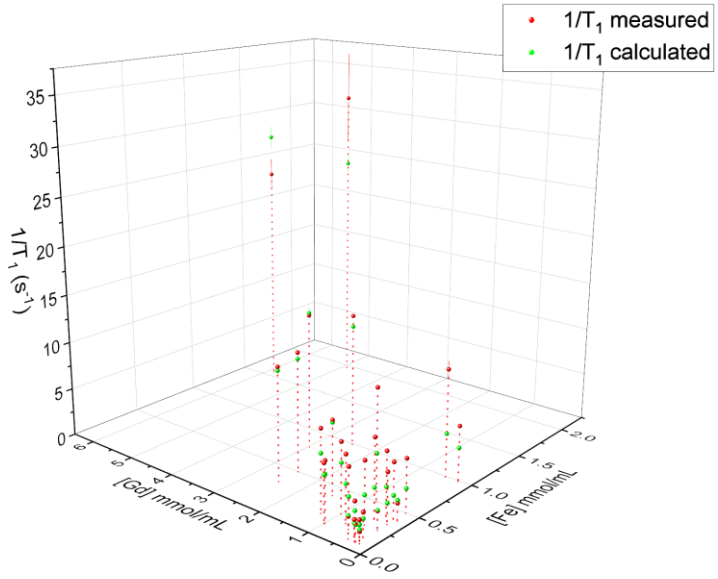

Figure 7.3: 3D plot of the measured $1/T_1$ at various concentrations of Feridex and Magnevist mixtures (red). A comparison is made with $1/T_1$ values that were calculated using equation (3) and the $1/T_1(0)$ from the $1/T_1$ of pure water (green).

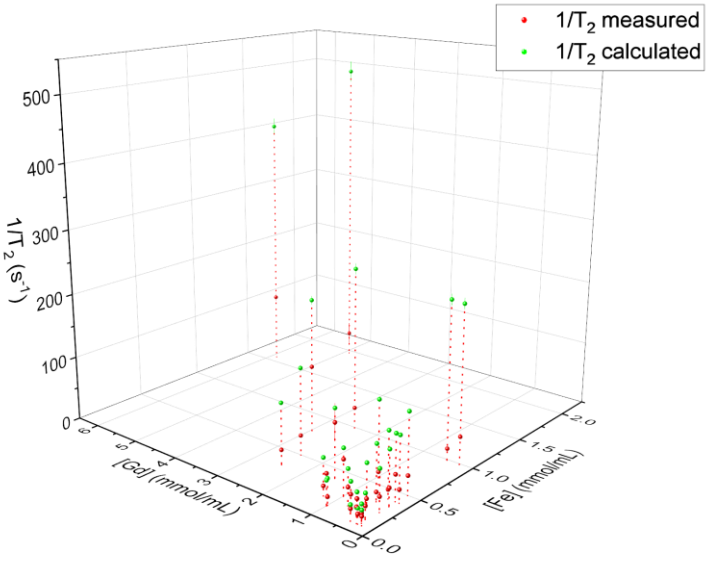

Figure 7.4: 3D plot of the measured $1/T_2$ at various concentrations of Feridex and Magnevist mixtures (red). A comparison is made with $1/T_2$ values that were calculated using equation (4) and the $1/T_2(0)$ from the $1/T_2$ of pure water (green).

To compare qualitatively the trends in the relaxivity data, contour color plots were generated of the calculated $1/T_1$ and $1/T_2$ values, see Figure 7.5, and of the measured $1/T_1$ and $1/T_2$ values, see Figure 7.6. In these plots, blue represents a low $1/T_1$ or $1/T_2$, and red represents the high value, as indicated in the color bar. The black lines correspond with the tick marks on the color bar.

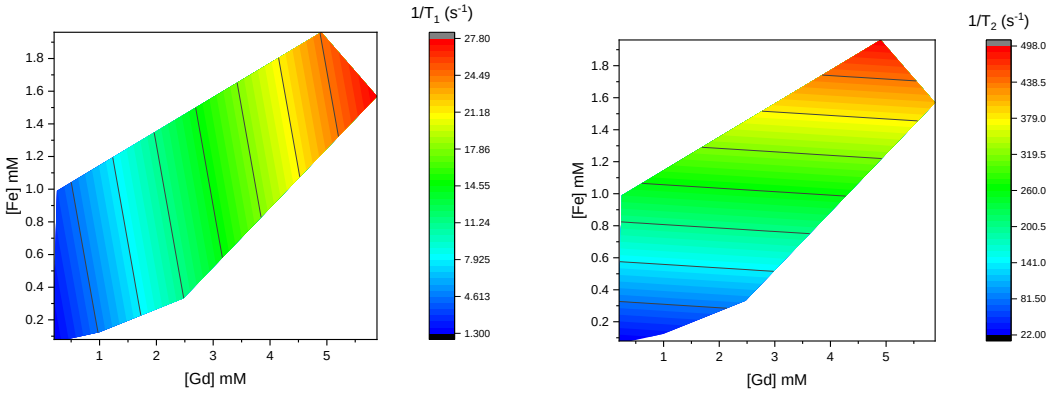

Figure 7.5: Contour color plots of calculated $1/T_1$ values (left) and $1/T_2$ values (right) of the sampled mixtures of CAs. Equations (3) and (4) were used, together 1/T(0) values of pure water.

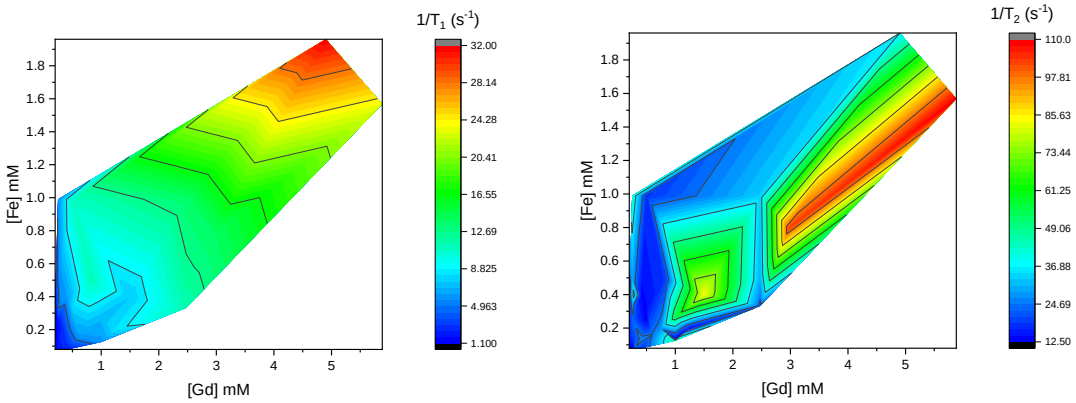

Figure 7.6: Visualization of measured $1/T_1$ and $1/T_2$ of mixtures in contour color plots.

In the calculated $1/T_1$, a gradual rise in relaxivity is observed, that seems to scale with both the concentration [Gd] and [Fe]. As expected from the calculated r_1 values, it scales more with the concentration of Magnevist. For $1/T_2$, a stronger dependence on the concentration of Feridex is observed, as a result of its higher r_2.

When the trends in the calculated relaxivities are compared qualitatively to those measured, a few differences are observed. In the measured $1/T_1$ plot, $1/T_1$ appears to depend more strongly on the concentration [Fe] than in the calculated plot. In the measured $1/T_2$ plot, the results seem more irregular for the different concentrations. Compared to the calculated values, the $1/T_2$ seems to scale a lot less strongly with the concentration [Fe].

To visualize specifically the differences between experimental and calculated results, contoured color maps of the deviations were generated. The differences $\Delta 1/T_1$ and $\Delta 1/T_2$ were calculated by subtracting the calculated relaxivity times from those measured at the same concentration. Figure 7.7 shows a color contour map of the difference $\Delta 1/T_1$ at various mixture concentrations and Figure 7.8 shows a color contour map with the ΔT_2 at these concentrations.

The calculated values are observed to deviate from the measured $1/T_1$ values in the case of low concentrations Gd^{3+}. In the low extreme, $1/T_1$ deviates by around -60% at the combination of concentrations [Gd] 0.2 mM – 1 mM and concentrations [Fe] 0.2 – 1 mM. The deviations from the calculated values appear to be the highest at the lower

concentrations of Gd^{3+}, and start to correspond more closely to the predicted value as the concentration increases.

A physical explanation for the underestimation of $1/T_1$ from the linear model lies in the influence of the magnetization of the Feridex on the r_1 of Magnevist. The Gd^{3+} ions in Magnevist have a relatively large r_1 (4.10 $mM^{-1}s^{-1}$), which is dependent on its magnetic moment and electronic relaxation time T_{1e}. Interaction with the strongly magnetizable iron oxide nanoparticles may lead to an increase in the magnetization of Gd^{3+}, and thus a larger effective r_1. This synergistic effect between CAs has been observed in $NaGdF_4$ coated $NaDyF_4$ NPs, where the highly paramagnetic Dy^{3+}-based core enhanced the r_1 of Gd^{3+} ions in the shell.[28] This simultaneous dependence of the r_1 of a single contrast agent on the concentration of both contrast agents forms a complication for use of the linear model in the clinic, where it is not known *a priori* how the contrast agents will be distributed at the location of interest.

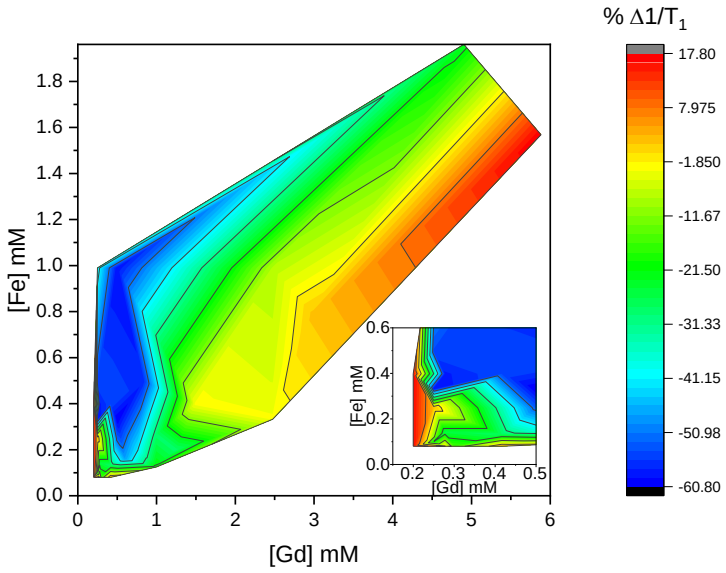

Figure 7.7: Color map plot of the difference between the calculated $1/T_1$ (using $1/T_1(0)$ from water) from linear addition of r_1 values determined from pure mixtures and the measured $1/T_1$ at the same concentration. The percent difference of the calculated values with respect to measured values is shown. The insert is a zoom-in of the region at low concentrations.

In the measured $1/T_2$ values, a much larger deviation from the corresponding calculated values can be seen. The lowest deviation is -25% at concentrations of ca. 0.1 mM [Fe]. At higher concentrations than this, the deviation $\Delta 1/T_2$ increases gradually further, reaching extreme differences of 1,250% at the highest concentrations of Feridex, where [Fe] is around 1.9 mM. At concentrations higher than ~0.2 mM [Fe], the T_2 values do not scale linearly with the concentration of the contrast agents.

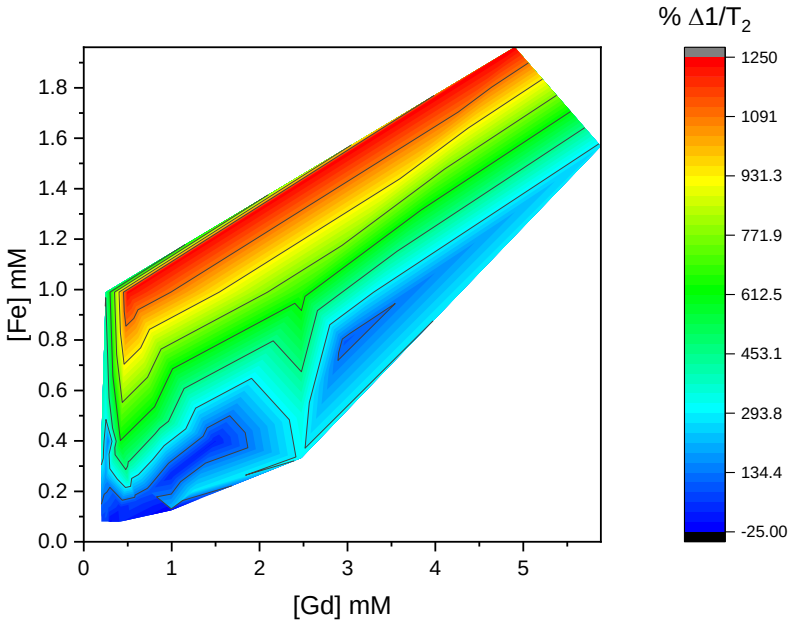

Figure 7.8: Color map plot of the difference between the calculated $1/T_2$ (using $1/T_2(0)$ from water) from linear addition of r_2 values determined from pure mixtures and the measured $1/T_2$ at the same concentration. The percent difference of the calculated values with respect to the measured values is shown.

It is speculated that this overestimation of $1/T_2$ from the linear model is due to overlap of the magnetic field perturbations generated by the paramagnetic nanoparticles that enhance the spin-spin relaxation of protons. The overlap may become higher at higher concentrations, meaning that the number of protons affected by the magnetic field does not increase linearly with the number of nanoparticles in dispersion. An alternative explanation is that the magnetic dipoles of the superparamagnetic particles interact with each other. Dipole-dipole interactions between magnetic nanoparticles have been shown to influence their magnetic properties at higher concentrations,[29-30] and have been observed to lead to

particle aggregation as well, via organization of magnetic nanoparticles in chains along their dipoles.[31]

In Appendix III, magnetic field calculations are provided that predict the magnetic field effect of an iron oxide nanoparticle on a nearby particle. A positive magnetic field is calculated for particles in line with each other, and a negative magnetic field for particles next to each other. It is shown that the magnetic field effect increases linearly with the concentration of the particles. These calculations further support the possibility that magnetic particles can aggregate in chains at higher concentrations. To further verify this effect, it would be interesting to measure $1/T_2$ values at even higher concentrations of T_2 contrast agents, to see potential diminished effects of r_2 at high concentrations. Using the presented MRI analysis, the errors in T_2 at high concentrations pure Feridex became too large for reliable use.

The aggregation effect might be further influenced by the presence of the Magnevist complexes. Magnevist could influence the aggregation, both by acting as a perturbation in the magnetic field that the iron oxide NPs experience, as well as due to its charge. The formation of chains of Feridex may be influenced by the magnetic field effect of the Magnevist complexes, resulting in a larger magnetic field in the presence of magnetized Magnevist, which could facilitate the chain formation. Furthermore, the charge of Magnevist complexes can affect the stability of the iron oxide NPs by screening the surface charge of the particles, which could result in aggregation of the colloids. The irregularity in the measured $1/T_2$ values might be the result of the variety of possible interactions

between the two CAs. Due to the complexity of these interactions, the behavior of relaxivity of mixtures of CAs might be inherently hard to predict, especially when nanocrystals are involved.

From these comparisons between calculated and experimental $1/T_1$ and $1/T_2$ data, it can be concluded that there is only a small range of concentrations in which the relaxivities are linearly additive. This is impractical for clinical use, where concentration can widely vary with the amount of contrast agent that reaches the area of interest (e.g., the tumor). These results are highly important for the proposed application of correlation MRI, where the concentration of T_1 and T_2 specific contrast agents could potentially be very low, or very high. It was calculated that from a typical (0.25 mL) nanoparticle injection before MRI, the concentration at the tumor location can typically be between 1 and 4 mM depending on tumor size, assuming a 1.5% localization of the injected contrast agent inside the tumor.[28] This suggests that the concentration range measured is clinically relevant both in the low and the high end. Especially since CAs are in development that target specifically locations of interest, higher concentrations of localized CA become increasingly clinically relevant.

It is proposed that to utilize a specific T_1 contrast agent in conjunction with a specific T_2 contrast, a 3-dimensional calibration curve needs be generated to predict the concentrations from $1/T_1$ and $1/T_2$ values outside the linear region. As an approach to generate a 3D calibration curve, polynomials (of the form shown in equation (5)) were fit to the plot of concentrations [Fe] and [Gd] vs. $1/T_1$, and to the plot of those concentrations vs. $1/T_2$. The results of these fits are shown in Figure7. 9. The fit through the $1/T_1$ data is reasonable,

with an R^2 of 0.945, whereas the fit through $1/T_2$ is less good with $R^2 = 0.557$. The poor fit in $1/T_2$ can be attributed to the larger variation in measured $1/T_2$ values, as shown previously in Figure 7.6 (left). It can be seen that outside the range of the measured samples, curves show drops down towards lower relaxivities, notably at high [Gd] in $1/T_1$ and high [Fe] in $1/T_2$. A drop in relaxivity with the increased concentration is not expected, and this is assumed to be a result of under-sampling in this range of the experimental data to which the polynomial is fitted.

$$z = p_{00} + p_{10} * x + p_{01} * y + p_{20} * x^2 + p_{11} * x * y + p_{02} * y^2 \quad (5)$$

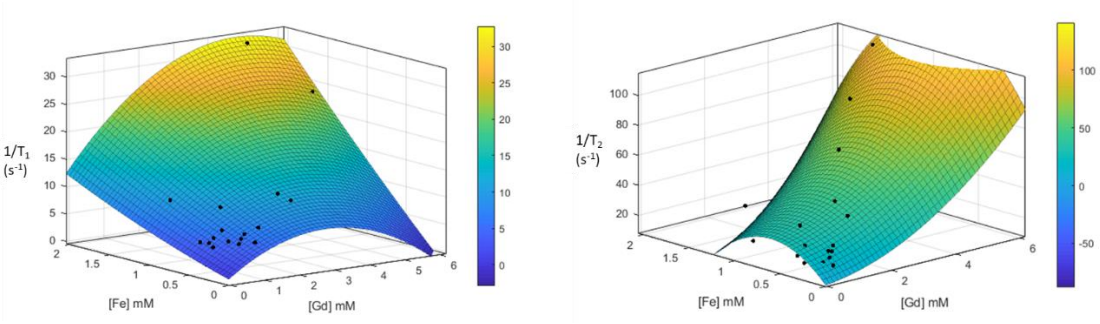

Figure 7.9: Measured $1/T_1$ values (left) and $1/T_2$ values (right) of mixtures (black dots), with corresponding fits to polynomial functions.

A demonstration of the potential use of these calibration curves to determine the concentrations in a mixture of Feridex and Magnevist of unknown composition, based on just the measured $1/T_1$ and $1/T_2$ values, is shown in Figure 7.10. Here, contour color plots are shown for the generated fits, and a red line shows the specific $1/T_1$ measured in the unknown sample, a green line shows the specific $1/T_2$. From readout of the crossing point of these lines, corresponding [Gd] and [Fe] can be determined. For the unknown sample,

the $1/T_1$ = 10.86 s^{-1}, and $1/T_2$ = 17.95 s^{-1}. [Gd]= 0.567 mM, and [Fe] = 1.173 mM were determined from the crossing point. The actual concentrations were [Gd] = 0.831 mM, and [Fe] = 0.990 mM. There is still a difference between the real and predicted concentration, the predicted [Gd] was 32% lower than the real concentration, and the [Fe] was 18% higher.

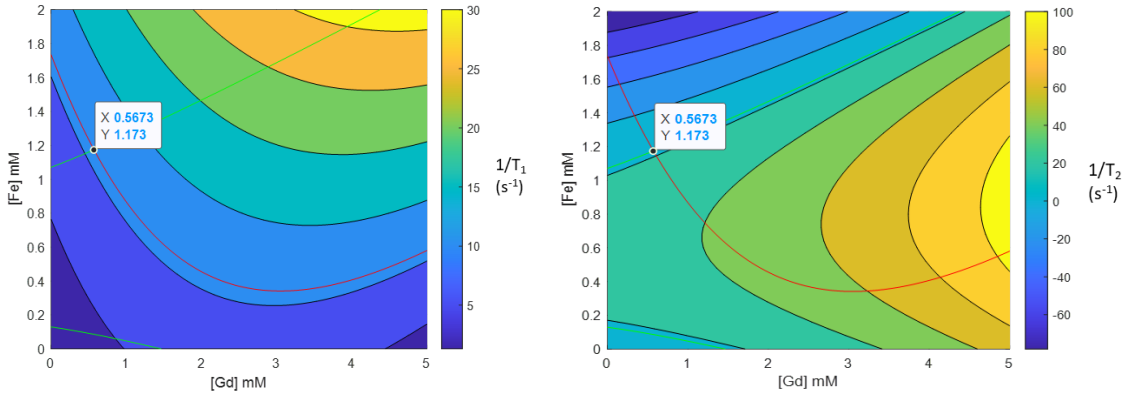

Figure 7.10: Demonstration of calibration curves based on polynomial fits to experimental data. An example determination is shown of a blind sample with $1/T_1$ = 10.86 s^{-1}, $1/T_2$ = 17.95 s^{-1}. From the crossing points, [Gd]= 0.567 mM, and [Fe] = 1.173 mM were determined. The actual concentrations were [Gd] = 0.831 mM, and [Fe] = 0.990 mM.

While a demonstration of the calibration curve could be provided, it is not yet in its optimal form. Notably, no measured sample data in the range of low [Fe] and high [Gd], and *vice versa*, was available for the generation of the polynomial fits. In these regions, the calibration curve can therefore not be used to calculate the concentration of Feridex or Magnevist based on the relaxivity of a mixture. To overcome this problem, samples need to be measured in the entire range of possible concentrations relevant for clinical use. Furthermore, it was noted that a high degree of irregularity existed for mixtures in the measured $1/T_2$. This has resulted in a fit with a low R^2, and is expected to yield a high error

in quantitative determination of concentrations. This can also be addressed by sampling a larger number of samples, potentially increasing the accuracy of $1/T_2$ determination in the concentration ranges of interest.

To summarize these observations: the results from the 3-dimensional data, showing $1/T_1$ and $1/T_2$ for mixtures of Feridex and Magnevist, demonstrate deviation from the equations (3) and (4). The deviations can be explained physically by interaction between the CAs, affecting their effective relaxivities. Here, r_1 might be underestimated due to an effective increase of r_1 by interaction of the low r_2/r_1 CA (Magnevist) with the magnetic field of the high r_2/r_1 CA (Feridex). Conversely, r_2 might be overestimated due to interactions between NPs of Feridex, and potential non-trivial effects on the colloidal behavior in the presence of Magnevist. A more general physical model to predict concentrations of two CAs needs to be developed, taking into consideration the influence CAs have on the magnetic properties of CAs in their surroundings. It should also be noted that the effective r_1 and r_2 of CAs inside tissue may deviate from those in pure water, due to differences in the chemical and magnetic environment. These deviations need to be taken into consideration for a quantitative model as well.

7.3 Conclusions

The viability of using a linear model to quantify two contrast agents simultaneously for a T_1 and T_2 MRI correlation technique was verified. T_1 and T_2 were measured of a series of commercially available Magnevist (Gd^{3+} multidentate complex) and Feridex (iron oxide nanoparticles) dispersions. From these, specific relaxivities were calculated to be r_1 =

2.10 ± 0.13 and r_2 = 238.97 ± 8.41 s^{-1} mM^{-1} for Feridex, and r_1 = 4.10 ± 0.19 and r_2 = 5.20 ± 0.20 s^{-1} mM^{-1} for Magnevist. The values were used to predict r_1 and r_2 values of mixtures of the two contrast agents. In 3D curves, the calculated values were compared to values measured at the same concentrations. It was found that the 3D curves correlated closely for T_1 values at concentrations above 1.5 mM [Gd]. Below these concentrations, the measured values started to deviate from those calculated. For T_2 values, a difference was observed at higher concentrations of Feridex. Especially above 0.2 mM [Fe], the experimental data started to deviate strongly from the calculated data. It was suggested that the T_2 does not scale linearly with the concentration of the T_2 active contrast agents. To overcome this problem in correlation MRI, it is proposed that 3D curves of relaxation times of mixtures should be used. A demonstration of concentration determination using polynomial fits to measured relaxivity data of mixtures was shown, but the accuracy should be improved by having a larger amount of samples in the experimental data. The deviation in r_1 could be explained in general by an increased effective r_1 of Magnevist due to interaction with the Feridex magnetic fields. The deviation in r_2 by interactions of overlapping magnetic fields of Feridex nanoparticles in close proximity with each other. The deviations from the linear model fall in the clinically relevant concentration range, and mean that for the practical use of correlation MRI, two contrast agents cannot be quantified using this linear addition model.

7.4 Experimental methods

Chemicals. Feridex I.V.® (ferumoxides injectable solution), Magnevist - MAGNEVIST® (brand of gadopentetate dimeglumine). Double distilled water was used for dilutions.

Relaxation time determination. T_1 and T_2 were measured of a series of Feridex and Magnevist samples using a 9.4 T MRI. For the T_1 measurement, a T_1-FISP echo sequence was used with the following parameters: 1.5 ms echo time (TE), 3 ms repetition time (TR), 15 ° flip angle (FA), a 3.00 by 3.00 cm field of view (FOV), in a 128 by 128 matrix size. T_2 was measured using a T_2-MSME sequence, with parameters: 64 echoes, variable echo time (TE), 5000 ms repetition time (TR), 180 ° flip angle (FA), a 3.00 by 3.00 cm field of view (FOV), in a 128 by 128 matrix size**.**

Data analysis and fitting. 3-Dimensional plots and contour color maps were generated with both Origin and Matlab. Linear functions to data of pure dilutions of Feridex and Magnevist were carried out in Origin. Polynomial functions were fitted to 3-dimensional experimental data using Matlab.

Blind measurement. To test the use of the calibration curve, the relaxivity of a mixture of Feridex and Magnevist was measured without disclosing the concentration. The concentration was determined using the $1/T_1$ and $1/T_2$ values with the polynomial functions fitted to the experimental data of known concentrations.

7.5 References

1. Blamire, A. M., The Technology of MRI — the Next 10 Years? *Br. J. Radiol.* **2008,** *81*, 601-617.
2. Plewes, D. B.; Kucharczyk, W., Physics of MRI: A Primer. *J. Magn. Reson. Imaging.* **2012,** *35*, 1038-1054.
3. Rutt, B. K.; Lee, D. H., The Impact of Field Strength on Image Quality in MRI. *J. Magn. Reson. Imaging.* **1996,** *6*, 57-62.
4. Vachha, B.; Huang, S. Y., MRI with Ultrahigh Field Strength and High-Performance Gradients: Challenges and Opportunities for Clinical Neuroimaging at 7 T and Beyond. *Eur. Radiol. Exp.* **2021,** *5*, 1-18.
5. Hyon, B.; Na, B.; Song, I. C.; Hyeon, T., Inorganic Nanoparticles for MRI Contrast Agents. *Adv. Mater.* **2009,** *744*, 2133-2148.
6. Xiao, Y.-D.; Paudel, R.; Liu, J.; Ma, C.; Zhang, Z.-S.; Zhou, S.-K., MRI Contrast Agents: Classification and Application. *Int. J. Mol. Med.* **2016,** *38*, 1319-1326.
7. Wahsner, J.; Gale, E. M.; Rodríguez-Rodríguez, A.; Caravan, P., Chemistry of MRI Contrast Agents: Current Challenges and New Frontiers. *Chem. Rev.* **2018,** *119*, 957-1057.
8. Strijkers, G. J.; M Mulder, W. J.; F van Tilborg, G. A.; Nicolay, K., MRI Contrast Agents: Current Status and Future Perspectives. *Anticancer Agents Med. Chem.* **2007,** *7*, 291-305.
9. McRobbie, D. W.; Moore, E. A.; Graves, M. J.; Prince, M. R., *MRI from Picture to Proton*. 2 ed.; Cambridge University Press: Cambridge, 2006.

10. Johnson, N. J.; Oakden, W.; Stanisz, G. J.; Scott Prosser, R.; van Veggel, F. C. J. M., Size-Tunable, Ultrasmall $NaGdF_4$ Nanoparticles: Insights into Their T_1 MRI Contrast Enhancement. *Chem. Mater.* **2011,** *23*, 3714-3722.

11. Dash, A.; Blasiak, B.; Tomanek, B.; van Veggel, F. C. J. M., Validation of Inner, Second, and Outer Sphere Contributions to T_1 and T_2 Relaxation in Gd^{3+}-Based Nanoparticles Using Eu^{3+} Lifetime Decay as a Probe. *J. Phys. Chem. C* **2018,** *122*, 11557-11569.

12. Das, G. K.; Johnson, N. J.; Cramen, J.; Blasiak, B.; Latta, P.; Tomanek, B.; van Veggel, F. C. J. M., $NaDyF_4$ Nanoparticles as T_2 Contrast Agents for Ultrahigh Field Magnetic Resonance Imaging. *J. Phys. Chem. Lett.* **2012,** *3*, 524-529.

13. Zhang, X.; Blasiak, B.; Marenco, A. J.; Trudel, S.; Tomanek, B.; van Veggel, F. C. J. M., Design and Regulation of $NaHoF_4$ and $NaDyF_4$ Nanoparticles for High-Field Magnetic Resonance Imaging. *Chem. Mater.* **2016,** *28*, 3060-3072.

14. Evans, A. C.; Marrett, S.; Torrescorzo, J.; Ku, S.; Collins, L., MRI-PET Correlation in Three Dimensions Using a Volume-of-Interest (Voi) Atlas. *J. Cereb. Blood Flow Metab.* **1991,** *11*, A69-A78.

15. Pace, L.; Nicolai, E.; Luongo, A.; Aiello, M.; Catalano, O. A.; Soricelli, A.; Salvatore, M., Comparison of Whole-Body PET/CT and PET/MRI in Breast Cancer Patients: Lesion Detection and Quantitation of ^{18}F-Deoxyglucose Uptake in Lesions and in Normal Organ Tissues. *Eur. J. Radiol.* **2014,** *83*, 289-296.

16. Thompson, N. L., Fluorescence Correlation Spectroscopy. In *Topics in Fluorescence Spectroscopy*, Springer: 2002; pp 337-378.

17. Weiss, S., Fluorescence Spectroscopy of Single Biomolecules. *Science* **1999,** *283*, 1676-1683.

18. Ma, D.; Gulani, V.; Seiberlich, N.; Liu, K.; Sunshine, J. L.; Duerk, J. L.; Griswold, M. A., Magnetic Resonance Fingerprinting. *Nature* **2013,** *495*, 187-192.

19. Anderson, C. E.; Donnola, S. B.; Jiang, Y.; Batesole, J.; Darrah, R.; Drumm, M. L.; Brady-Kalnay, S. M.; Steinmetz, N. F.; Yu, X.; Griswold, M. A., Dual Contrast-Magnetic Resonance Fingerprinting (DC-MRF): A Platform for Simultaneous Quantification of Multiple MRI Contrast Agents. *Sci. Rep.* **2017,** *7*, 1-10.

20. Anderson, C. E.; Johansen, M.; Erokwu, B. O.; Hu, H.; Gu, Y.; Zhang, Y.; Kavran, M.; Vincent, J.; Drumm, M. L.; Griswold, M. A., Dynamic, Simultaneous Concentration Mapping of Multiple MRI Contrast Agents with Dual Contrast-Magnetic Resonance Fingerprinting. *Sci. Rep.* **2019,** *9*, 1-11.

21. Marriott, A.; Bowen, C.; Rioux, J.; Brewer, K., Simultaneous Quantification of SPIO and Gadolinium Contrast Agents Using MR Fingerprinting. *Magn. Reson. Imaging* **2021,** *79*, 121-129.

22. Koenig, S. H., From the Relaxivity of Gd $(DTPA)^{2-}$ to Everything Else. *Magn. Reson. Med.* **1991,** *22*, 183-190.

23. Koenig, S. H.; Kellar, K. E., Theory of $1/T_1$ and $1/T_2$ NMRD Profiles of Solutions of Magnetic Nanoparticles. *Magn. Reson. Med.* **1995,** *34*, 227-233.

24. Fellner, F.; Janka, R.; Fellner, C.; Dobritz, M.; Lenz, M.; Lang, W.; Bautz, W., Gd-BOPTA:" The MRA Contrast Agent of Choice"? *Röntgenpraxis (Stuttg.)* **1999,** *52*, 51-58.

25. Rohrer, M.; Bauer, H.; Mintorovitch, J.; Requardt, M.; Weinmann, H.-J., Comparison of Magnetic Properties of MRI Contrast Media Solutions at Different Magnetic Field Strengths. *Invest. Radiol.* **2005,** *40*, 715-724.

26. Korchinski, D. J.; Taha, M.; Yang, R.; Nathoo, N.; Dunn, J. F., Iron Oxide as an MRI Contrast Agent for Cell Tracking: Supplementary Issue. *Magn. Reson. Insights* **2015,** *8*, MRI. S23557.

27. Bryson, J. M.; Chu, W.-J.; Lee, J.-H.; Reineke, T. M., A B-Cyclodextrin "Click Cluster" Decorated with Seven Paramagnetic Chelates Containing Two Water Exchange Sites. *Bioconjug. Chem.* **2008,** *19*, 1505-1509.

28. Dash, A.; Blasiak, B.; Tomanek, B.; Latta, P.; van Veggel, F. C. J. M., Target-Specific Magnetic Resonance Imaging of Human Prostate Adenocarcinoma Using $NaDyF_4$–$NaGdF_4$ Core–Shell Nanoparticles. *ACS Appl. Mater. Interfaces* **2021,** *13*, 24345-24355.

29. Wu, K.; Su, D.; Saha, R.; Liu, J.; Wang, J.-P., Investigating the Effect of Magnetic Dipole–Dipole Interaction on Magnetic Particle Spectroscopy: Implications for Magnetic Nanoparticle-Based Bioassays and Magnetic Particle Imaging. *J. Phys. D: Appl. Phys.* **2019,** *52*, 335002.

30. García-Otero, J.; Porto, M.; Rivas, J.; Bunde, A., Influence of Dipolar Interaction on Magnetic Properties of Ultrafine Ferromagnetic Particles. *Phys. Rev. Lett.* **2000,** *84*, 167.

31. Myrovali, E.; Maniotis, N.; Makridis, A.; Terzopoulou, A.; Ntomprougkidis, V.; Simeonidis, K.; Sakellari, D.; Kalogirou, O.; Samaras, T.; Salikhov, R.,

Arrangement at the Nanoscale: Effect on Magnetic Particle Hyperthermia. *Sci. Rep.* **2016,** *6,* 1-11.

Chapter 8: Summary and Outlook

The goal of this dissertation was to further the understanding of the synthesis and internal structure of lanthanide-based nanomaterials, and demonstrate novel fabrication and imaging techniques that utilize them. The experimental results are summarized in this chapter.

In chapter 3, a typical synthesis method to fabricate $NaYF_4$:18% Yb^{3+}, 2% Er^{3+} UCNPs is described. Using 2-dimensional energy dispersive x-ray spectroscopy (EDS) mapping, it was demonstrated that using colloidal synthesis methods, the Yb^{3+} and Er^{3+} dopant ions are not homogeneously distributed inside the resulting particles. A localization of the smaller sized dopant ions inside the nanoparticle center was observed. Heating the particles at temperatures that are typically used for annealing bulk up-conversion crystals resulted in a homogenous distribution of all lanthanide ions inside the particles. However, comparing up-conversion emission intensities before and after high-temperature annealing, no increase was observed. Together with the previously reported observations that surface-passivated UCNPS don't fully reach the quantum yields observed in bulk UC crystals, it is inferred that other internal defects must be present inside colloidally prepared UCNPs. IR spectroscopy offered hints that O-H was present inside the UCNPs, which may act as a quencher, thus limiting quantum yield. The results are highly relevant for optimization of UCNP quantum yields, design of UCNP based luminescent thermometers, and singly doped nanoparticles. Follow-up experiments could include shell growth over annealed NPs to optimize their quantum yield.

Chapter 4 describes a strategy to trap nanoparticles doped with a single Er^{3+} ion, in order to fabricate a source of single photons on demand. The strategy described relies on trapping selectively singly doped nanoparticles in gold nano-aperture optical tweezers. First, the efficacy of trapping doped nanoparticles inside gold aperture tweezers was demonstrated using $NaYF_4$:18% Yb^{3+}, 2% Er^{3+} UCNPs. Trapping proved successful, and furthermore a large increase of the up-conversion emission intensity was observed, owing to the increase in the electric field of the gold aperture. The largest intensity increase was observed for nano-apertures with dimensions 100 x 208 nm^2, where the emission intensity of the UCNPs was 400 times higher than in free solution. Apertures with these dimensions were used to trap $NaYF_4$ NPs with trace amounts of dopant Er^{3+} ions. It was found that the discrete up-conversion emission intensities measured in these nanoparticles closely matched the Poisson distribution of Er^{3+} ions inside the nanoparticles, which suggested that most emitting nanoparticles trapped had a single Er^{3+} dopant ion. The experiments were reproduced using double nano-hole gold apertures, where an even higher local field enhancement led to a further 50x emission intensity increase. A close following of Poisson statistics in NPs doped with trace amounts of Er^{3+} is observed as well in these apertures. Further demonstration of anti-bunching in these emitters needs to be done to verify the true single photon nature of the emission, but the results seem highly promising to access single photons on demand using NPs doped with a single Er^{3+} ion inside gold nano-apertures.

Encouraged by these results, a photo-chemical anchoring method to trap permanently single Er^{3+} doped NPs inside apertures was developed, as presented in chapter 5. The method relied on functionalization of the surface of $NaYF_4$ NPs doped with trace amounts

of Er^{3+} with thiol-terminated phospholipids. The thiol groups were protected with a photo-sensitive leaving group, i.e., through reaction with 2-bromo-4'-hydroxyacetophenone. This protecting group is removable by 340 nm light, allowing selective deprotection and reaction of the thiol with the aperture gold surface, after single Er^{3+} emission is verified. To test the efficacy of thiol protection and deprotection, functionalized nanoparticles were exposed to 340 nm light in the presence of a luminescent thiol-detection group. Light exposure led to reaction with the detection group and emission of the luminescent molecule. The method was tested in a double-hole gold nano-aperture by trapping nanoparticles followed by 340 nm light exposure, leading to permanent anchoring, as verified with scanning electron microscopy. This novel nanofabrication method seems highly promising for the large-scale production of single emitting nanoparticles, which is potentially fully automatable. Measurement of single Er^{3+} of the trapped particles needs to be done, then the procedure can be adopted for automation and upscaling.

A novel method that utilizes lanthanide and iron-doped particles to verify the actual radiation dose inside living tissue is described in chapter 6. The synthesis of CaF_2 NPs doped with Eu^{3+} and a mixture of Fe^{2+} and Fe^{3+} ions was described and successful synthesis verified with TEM, XRD, and Mössbauer spectroscopy. Dosimetry experiments were performed at 40 keV, which falls in the diagnostic energy range, and at 6 MeV, which is in the therapeutic energy range. In the dosimetry demonstrations, T_1 and T_2 of a europium or iron CaF_2 dispersion was measured, followed by irradiation at either 40 keV or 6 MeV, then measurement of T_1 and T_2 again at various points after irradiation. It was found that CaF_2:Eu^{3+} NPs raised the MRI contrast strongly upon irradiation at 40 keV, and

$CaF_2:Fe^{2+}/Fe^{3+}$ lowered it. These results were explained by photo-electrons generated by the x-rays leading to reduction of Eu^{3+} to Eu^{2+}, and reduction of Fe^{3+} to Fe^{2+}. Of these, Eu^{2+} and Fe^{3+} are good T_1 and T_2 contrast agents, owing to their long electronic relaxation times and increased paramagnetism. When 6 MeV radiation was used in the same experiment, a rise in T_1 and T_2 was seen for $CaF_2:Fe^{2+}/Fe^{3+}$, which was attributed to oxidation of Fe^{2+} to Fe^{3+} by oxidative species generated by high-energy x-rays. From the demonstrations, it was concluded that $CaF_2:Eu^{3+}$ was the best candidate for x-ray detection at diagnostic energies and $CaF_2:Fe^{2+}/Fe^{3+}$ the best candidate for x-ray detection at therapeutic energies, but the effect shown by the latter is not as high as it could be due to the low amount of Fe^{2+} ions in the CaF_2 particles. $NaDyF_4$ NPs were proposed as a dose-invariant contrast agent to help localize the dose-sensitive particles inside the human body during treatment. It was shown that presence of the $NaDyF_4$ raised T_2 strongly, as expected, without altering the change in contrast upon radiation significantly. These results were very promising to develop contrast agents that can measure *in vivo* the radiation dose during treatment and diagnosis using x-rays. Obviously, the materials need to be optimized to maximize the effect, and *in vivo* demonstrations should be performed. Furthermore, the development and use of a core-shell particle that has an inert $NaDyF_4$ core and an x-ray sensitive $CaF_2:Eu^{3+}$ or $CaF_2:Fe^{2+}$ shell should be demonstrated.

In chapter 7, an MRI technique is described that relies on simultaneous imaging of T_1 and T_2 contrast agents. In this MRI correlation technique, higher sensitivity could potentially be achieved by combining the contrast in T_1 and T_2. Furthermore, a variety of tissue interactions could simultaneously be imaged using the MRI modalities as different

colors. To demonstrate the technique, relaxivities of the commercially available T_1 contrast agent Magnevist (Gd-DTPA), and T_2 contrast agent Feridex (superparamagnetic iron oxide) were determined. In measuring T_1 and T_2 of a series of mixtures of these two contrast agents, it was found that the relaxivities of the mixtures did not correspond with the sum of the relaxivities of the contrast agent constituents. Especially T_2 varied strongly, with its deviation from the predicted value increasing with the contrast agent concentration. It was concluded that at higher concentrations, relaxivities change non-linearly with the concentrations. Deviations from the linear change are attributed to CAs affecting each others relaxivity in mixtures. It was proposed that for combined T_1 and T_2 imaging, a 3-dimensional calibration curve needs to be used to quantify the concentrations based on measured relaxation time values. The demonstration of the calibration curve needs to be followed up by showing how it can be used to quantify the concentrations of a contrast agent mixture. If this can be shown, *in vivo* experiments can be done to show the validity of the correlation technique.

Appendix I: Supplementary information to chapter 3

TEM overview images

Supplementary to the TEM figure shown in the main chapter (Figure 3.1 (left)), Figure I.1 shows more TEM images from the same batch of nanoparticles, demonstrating the homogeneity in size and shape of the nanoparticles in dispersion.

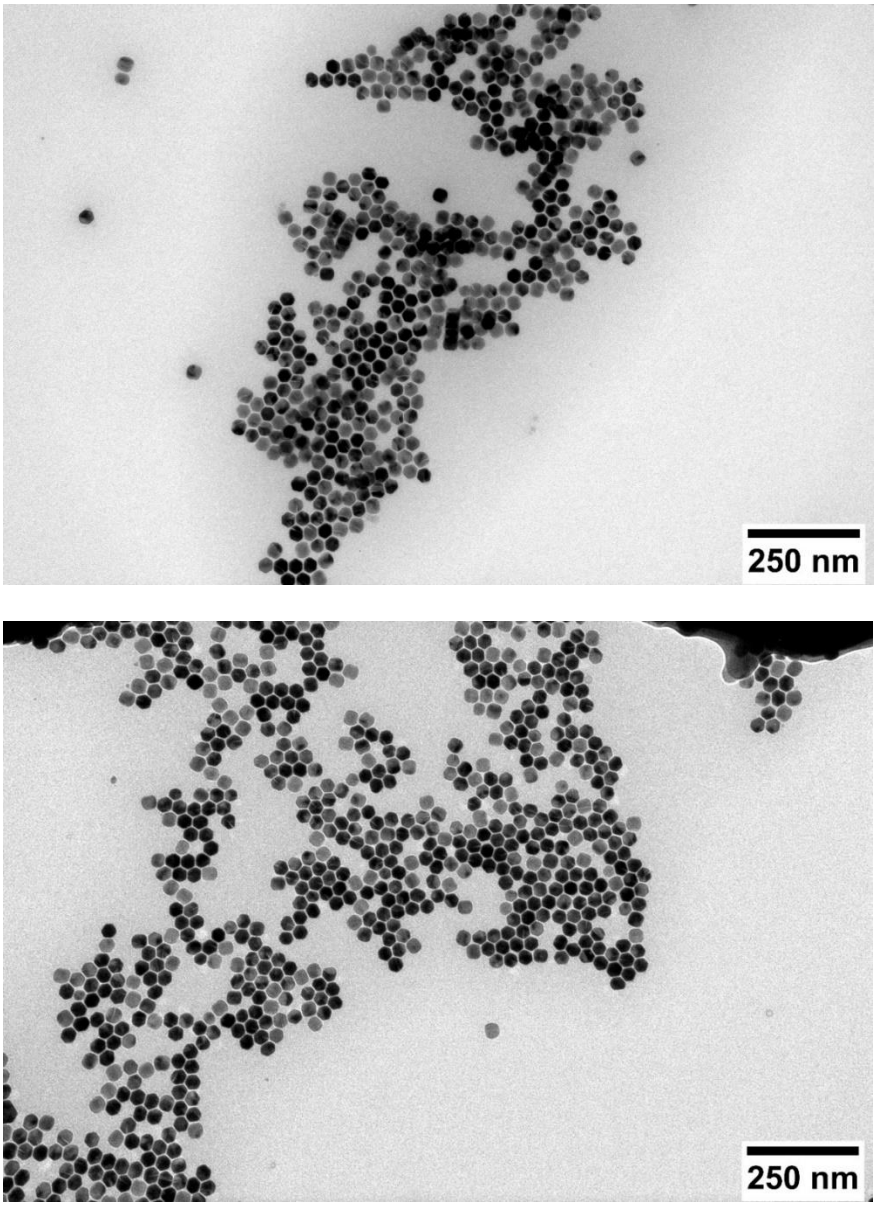

Figure I.1: Representative bright field TEM (operated at 80 kV) images of UCNPs.

Integrated ring vs. line comparisons

SI Figure I.2 (top) shows elemental maps acquired from UCNPs. The number of counts of the characteristic x-rays for Y, Yb, and Er are shown mapped in two dimensions. Shown under this are bright field TEM images with areas of interest outlined in yellow. A comparison was made between five concentric rings around the nanoparticle (left) and 6 successive circles through the nanoparticle (right). The relative ratios Yb/Y, Er/Yb, and Er/Y are plotted in the bottom left for the concentric ring comparison and the bottom right for the successive circle comparison. Similar trends were observed between the methods, where the ratio Yb/Y and Er/Y are seen to be the highest in the center of the nanoparticles. Figure I.3 shows the same comparison for a second nanoparticle.

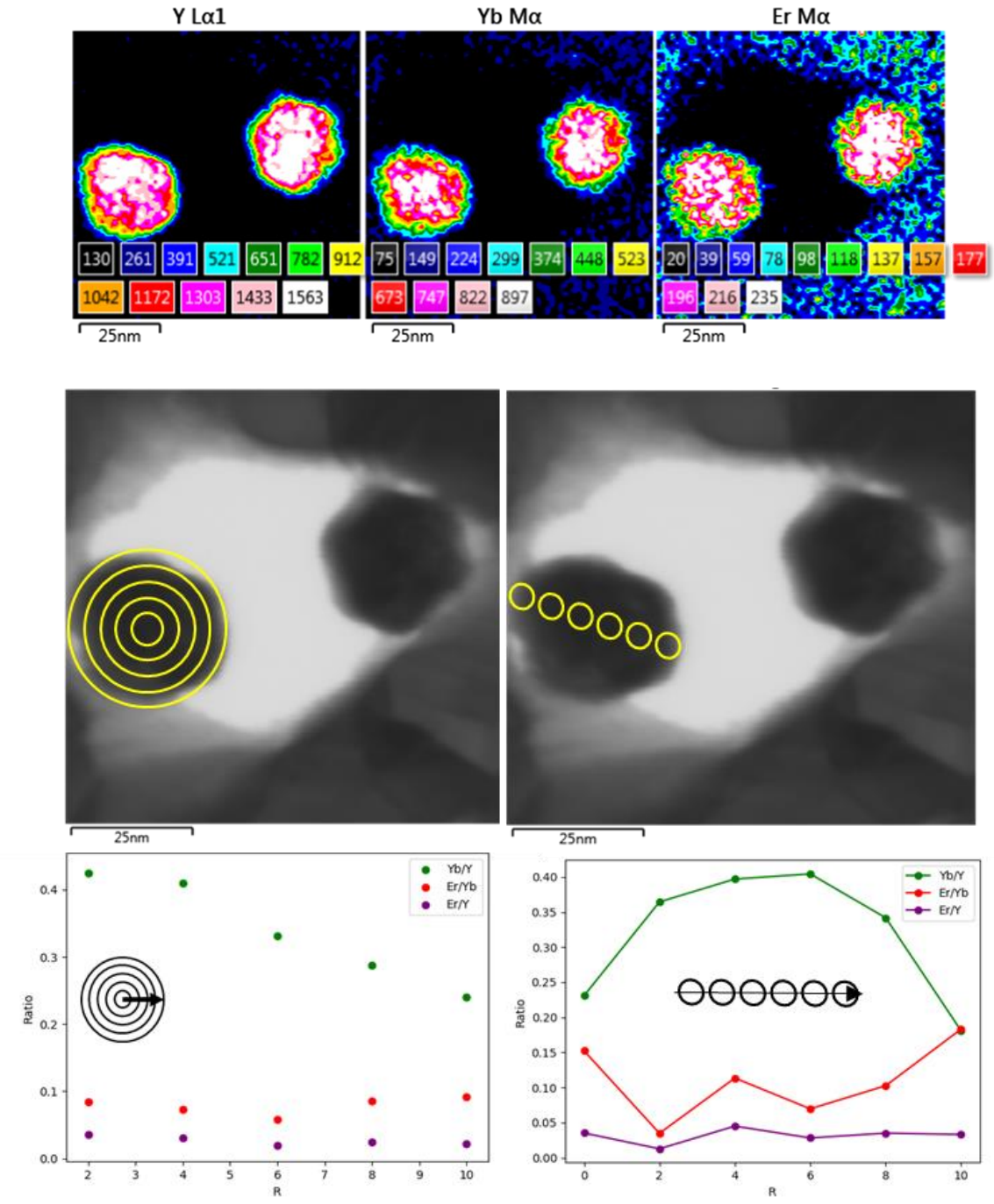

Figure I.2: EDS maps and comparison of emanating circle integration versus integration of circles over a line.

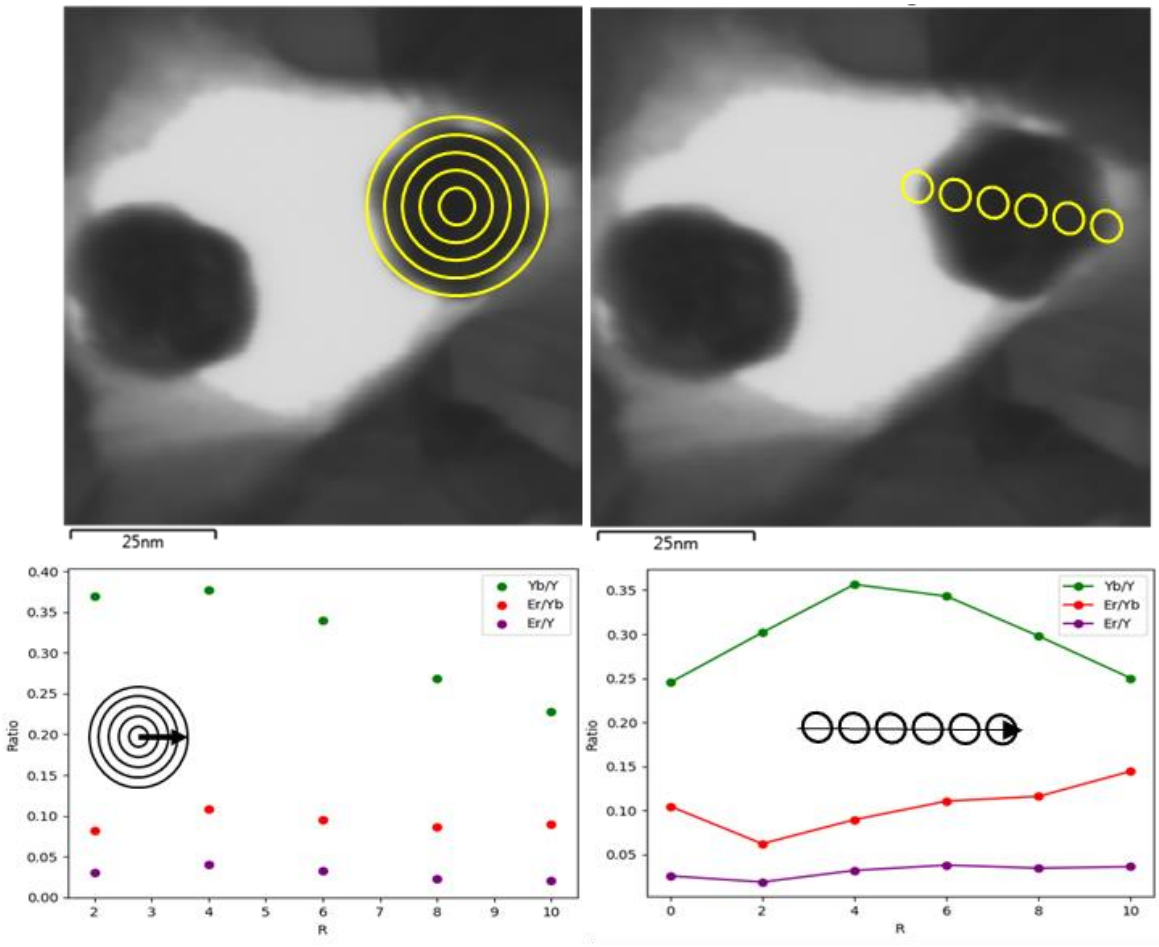

Figure I.3: Comparison of emanating circle integration versus integration of circles over a line.

Elemental maps pre-heating

Figures I.4 and I.5 show more representative EDS maps collected of particles before heating at 590 °C, collected from the same TEM grid as shown in Figure 3.4 of the main chapter. The maps were generated using intensity counts of the characteristic x-ray lines of Y, Yb, and Er, with the number of counts corresponding to the colors as indicated in the bottom of the images. The bottom image of Figure I.4 is shown in the main chapter Figure 3.4 as an elemental map, and its corresponding EM image is shown in the main text Figure 3.3.

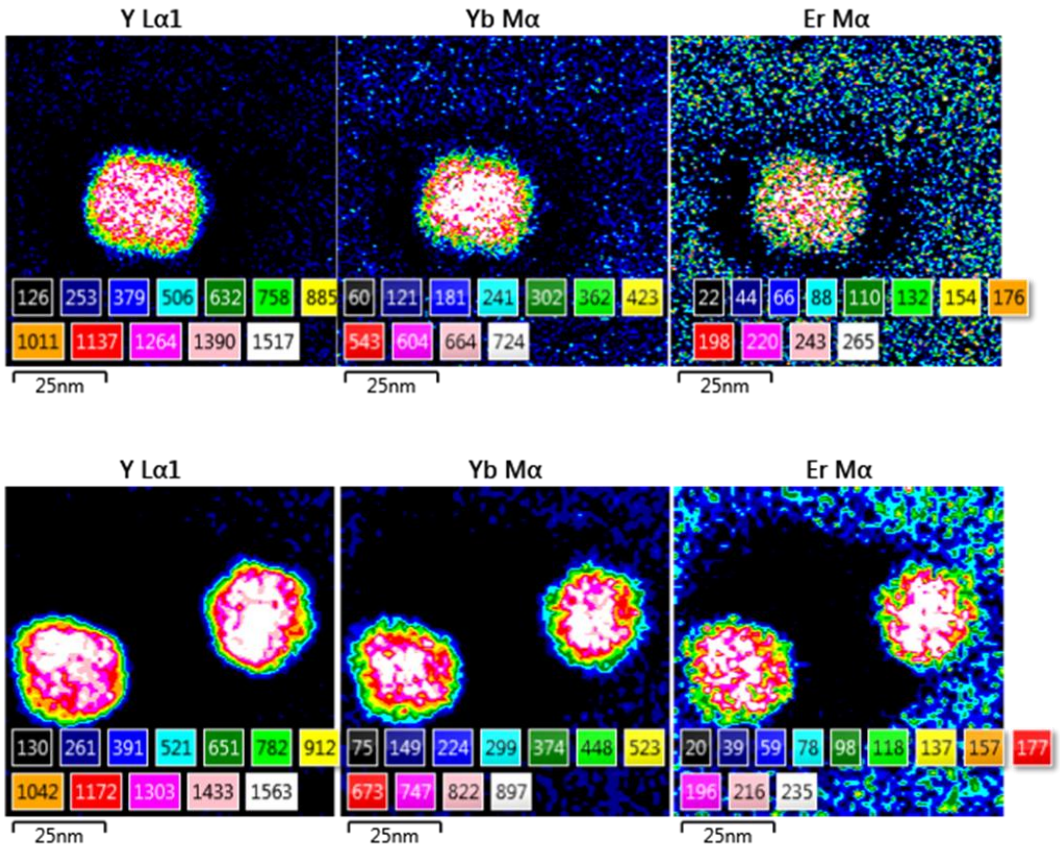

Figure I.4: EDS maps collected before heating at 590 °C.

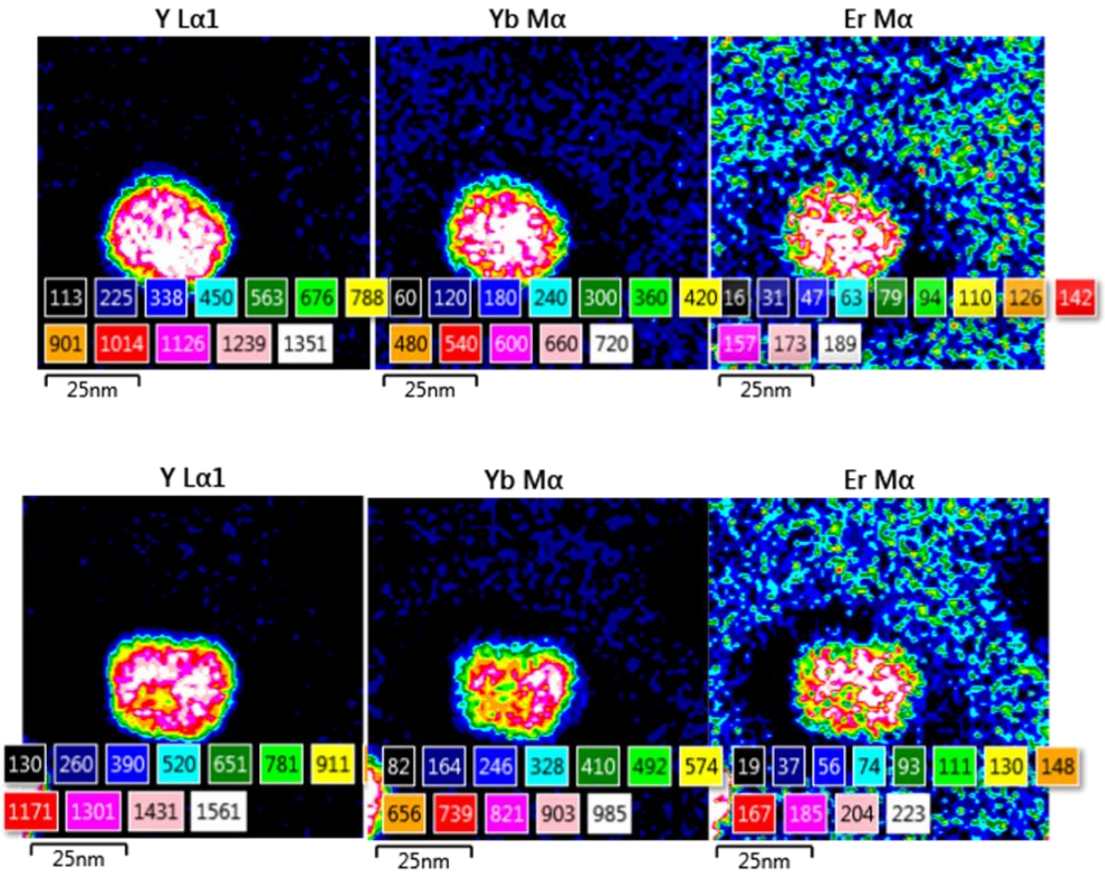

Figure I.5: EDS maps collected before heating at 590 °C.

Elemental maps post-heating

Figure I.6 shows more representative EDS maps collected of particles after heating at 590 °C, collected from the same TEM grid as Figure 3.7 shown in the main chapter. The maps were generated using intensity counts of the characteristic x-ray lines of Y, Yb, and Er. The number of counts corresponding to the colors is indicated in the bottom of the images. The middle image of SI Figure I.6 is shown in the main text Figure 3.7 as an elemental map, and its corresponding EM image is shown in the main chapter Figure 3.6 (left). The bottom image of SI Figure I.6 shows a cluster of nanoparticles and its corresponding EM image is shown in main text Figure 3.7.

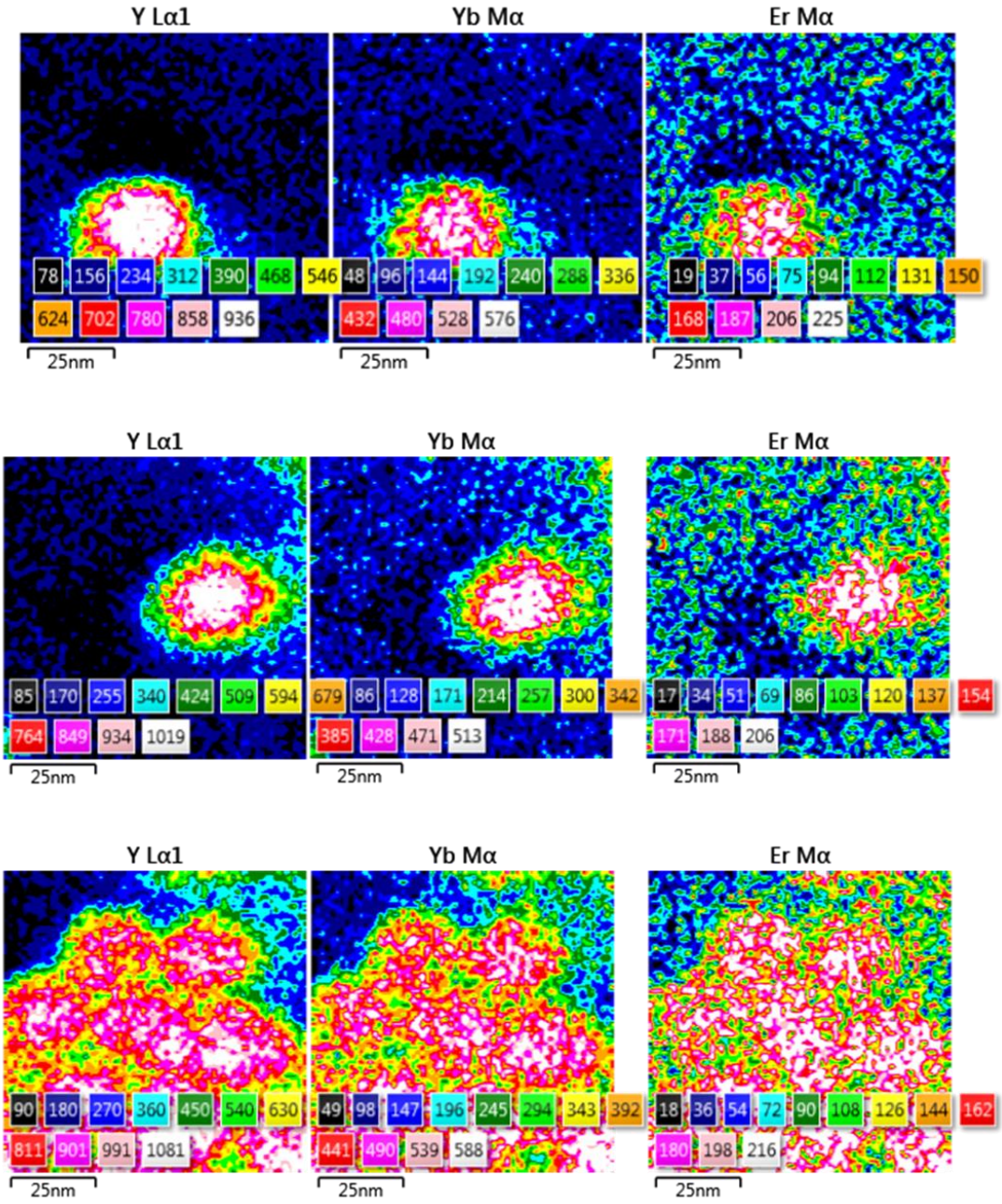

Figure I.6: EDS maps collected after heating at 590 °C.

Extended IR spectrum UCNPs

See Figure I.7 for an IR spectrum comparing UCNPs washed with D_2O to those in hexanes. The peak for the OD vibration is expected at 2500 cm^{-1}. Potentially a small peak can be observed as a weak shoulder, but it is not very distinct, possibly due to overlap with the very large CH stretch vibrational peak, as well as the reduced oscillator strength of the O-D vibration. A small peak is observed at 2300 cm^{-1} which can be attributed to CO_2. Figure I.8 shows the full IR spectrum collected of the particles.

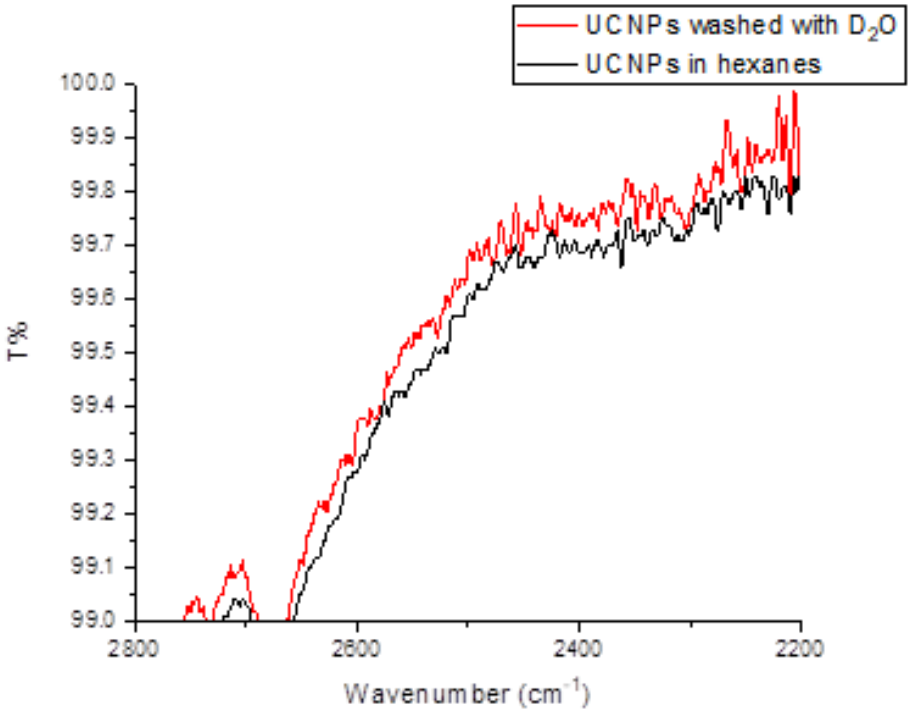

Figure I.7: IR spectra of UCNPs in hexanes, before (black) and after washing with D_2O.

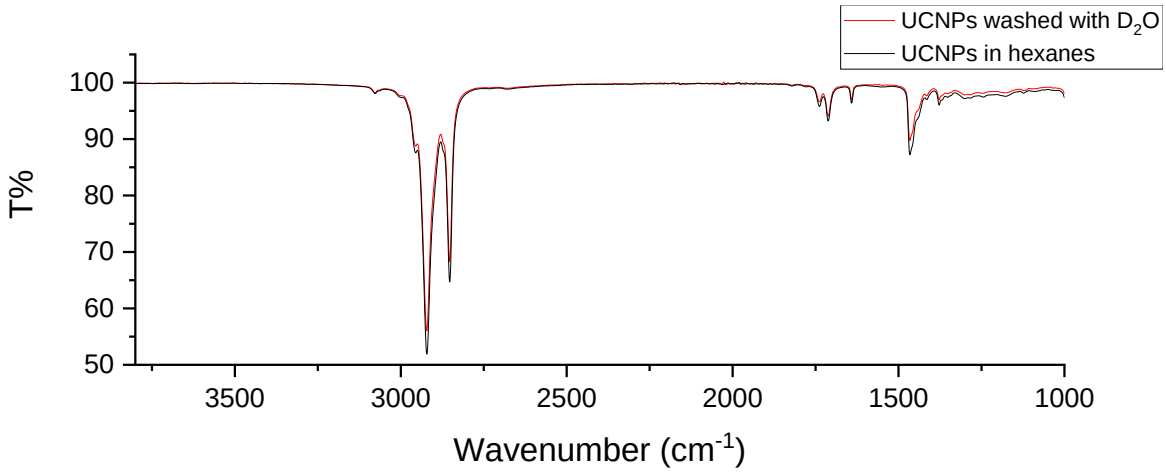

Figure I.8: Full IR spectrum UCNPs in hexanes, before (black) and after (red) washing with D_2O.

Appendix II: Supplementary information to chapter 5

Discrete Er^{3+} emission levels

Low-loss wavelength single-photon emission was inferred by measuring emission of $NaYF_4$ NPs doped with trace amounts of Er^{3+} ions. A dispersion of 22.7 nm $NaYF_4$ NPs with ca. 2.48 Er^{3+}/NP in hexanes was used for trapping experiments with a double nano-hole gold aperture. After trapping of a single NP was confirmed, emission was measured around 1,550 nm upon 980 nm excitation. The experiment was repeated for a total of 100 trapping events. Figure II.1 (top) shows the resulting emission spectra. Discrete emission levels are observed at six distinct intensities, around 100 counts apart, and a number of particles with no emission is observed as well. In Figure II.1 (bottom) the number of nanoparticles corresponding to each discrete emission level is compared to a predicted Poisson distribution of Er^{3+} ions in the NPs, assuming an average of 2.48 Er^{3+}/NP. The number of Er^{3+} ions measured from discrete emission intensities is lower than predicted from Poisson statistics, as a likely result of quenching of Er^{3+} ions close to the NP surface. This deviation is similar to what was observed in previous work for discrete emission of Er^{3+} ions measured in the visible region.[1-2] An additional possible reason for deviation from Poisson statistics may be the non-statistical distribution of Er^{3+} ions inside $NaYF_4$ NPs, as was observed in $NaYF_4$: Yb^{3+}, Er^{3+} up-converting NPs and doped $NaGdF_4$ NPs.[3-4] These results predict that ca. 34% of the NPs in this dilutely doped ensemble can act as a single-photon emitter in the low-loss wavelength regime.

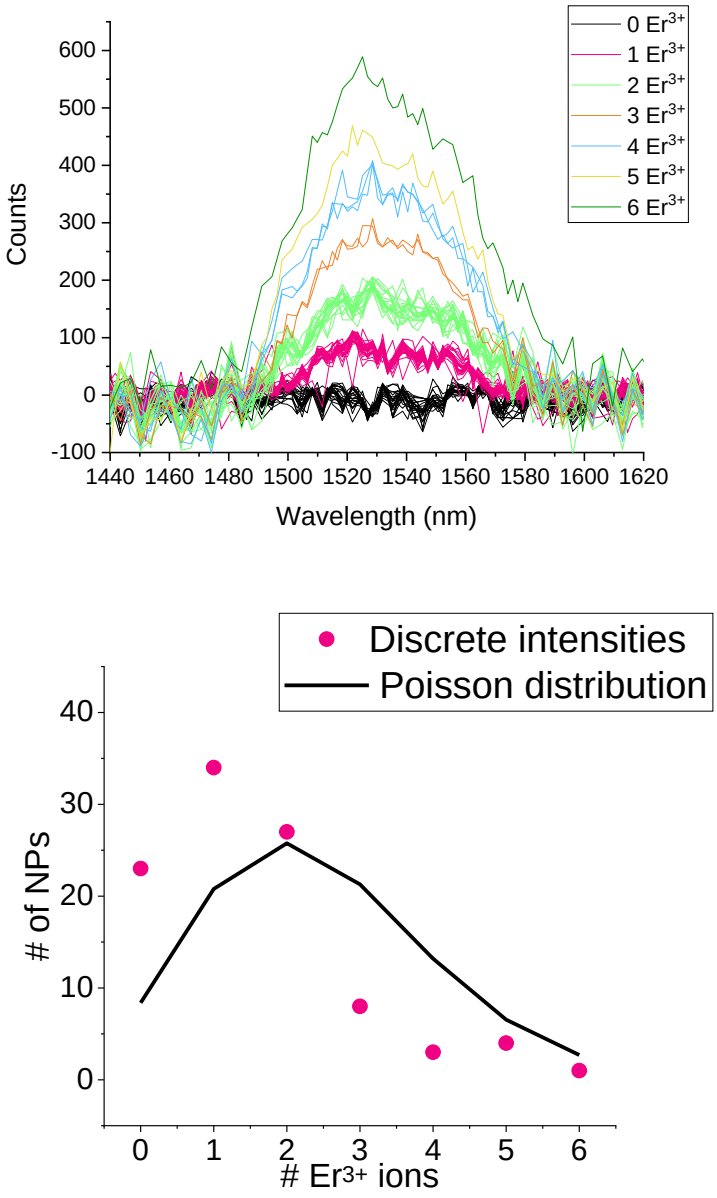

Figure II.1: (top) Emission counts from $NaYF_4$ NPs dilutely doped with Er^{3+} in hexanes showing discrete emission intensities corresponding to different amounts of active erbium emitters. Spectra were collected by a spectrometer with 10 s acquisition time. (bottom) Comparison of predicted distribution of Er^{3+} ions over the NPs from Poisson statistics with the distribution of discrete emission intensities, assuming an average of 2.48 Er^{3+} ions per NP.

Mechanism of thiol-detection agent attachment

The proposed mechanism for the thiol-detection reagent is shown in Figure II.2. Via attachment of the SR group to a carbon atom in a Michael addition, the fluorescein system shifts from a spiro-structure to its open form that is fluorescent.

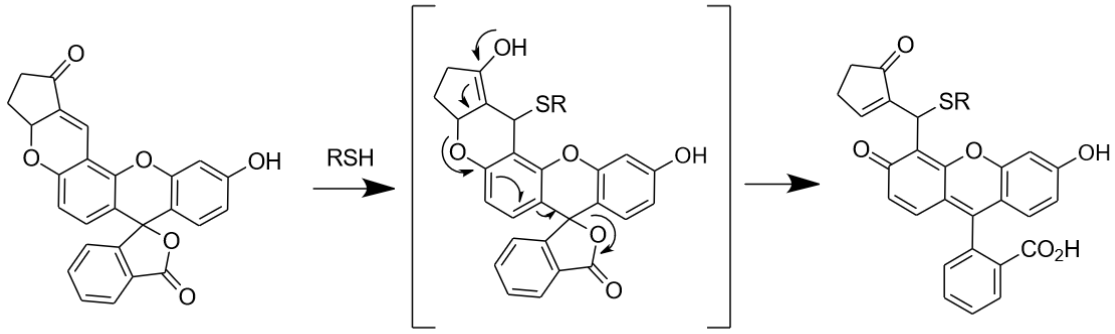

Figure II.2: Proposed mechanism where the fluorescein-like molecule opens up to its fluorescent form

To explain the background emission that was observed an equilibrium reaction is proposed where the spiro structure of the indicator molecule opens up to its fluorescent form, see Figure II.3.

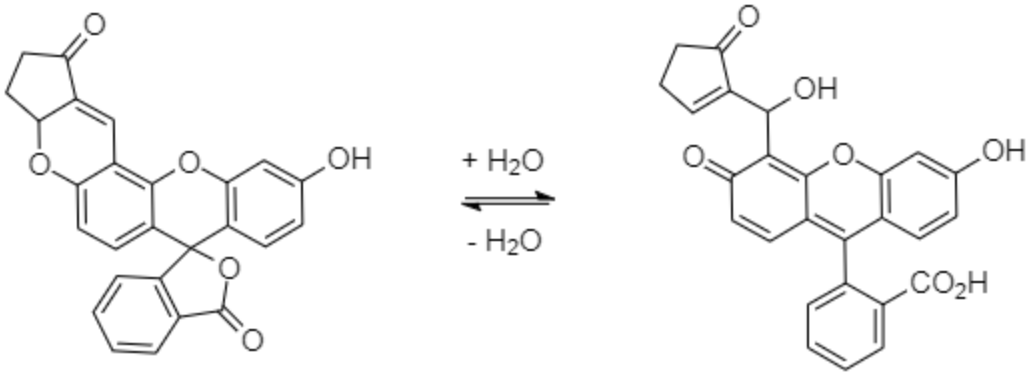

Figure II.3: Equilibrium structure proposed where the spiro group opens up to an open form that is fluorescent.

Anchoring events

Several instances of anchored nanoparticles are shown in Figure II.4, captured with scanning electron microscopy (Hitachi S-4800). Here, double nanohole apertures are presented with immobilized NPs shown encircled in yellow.

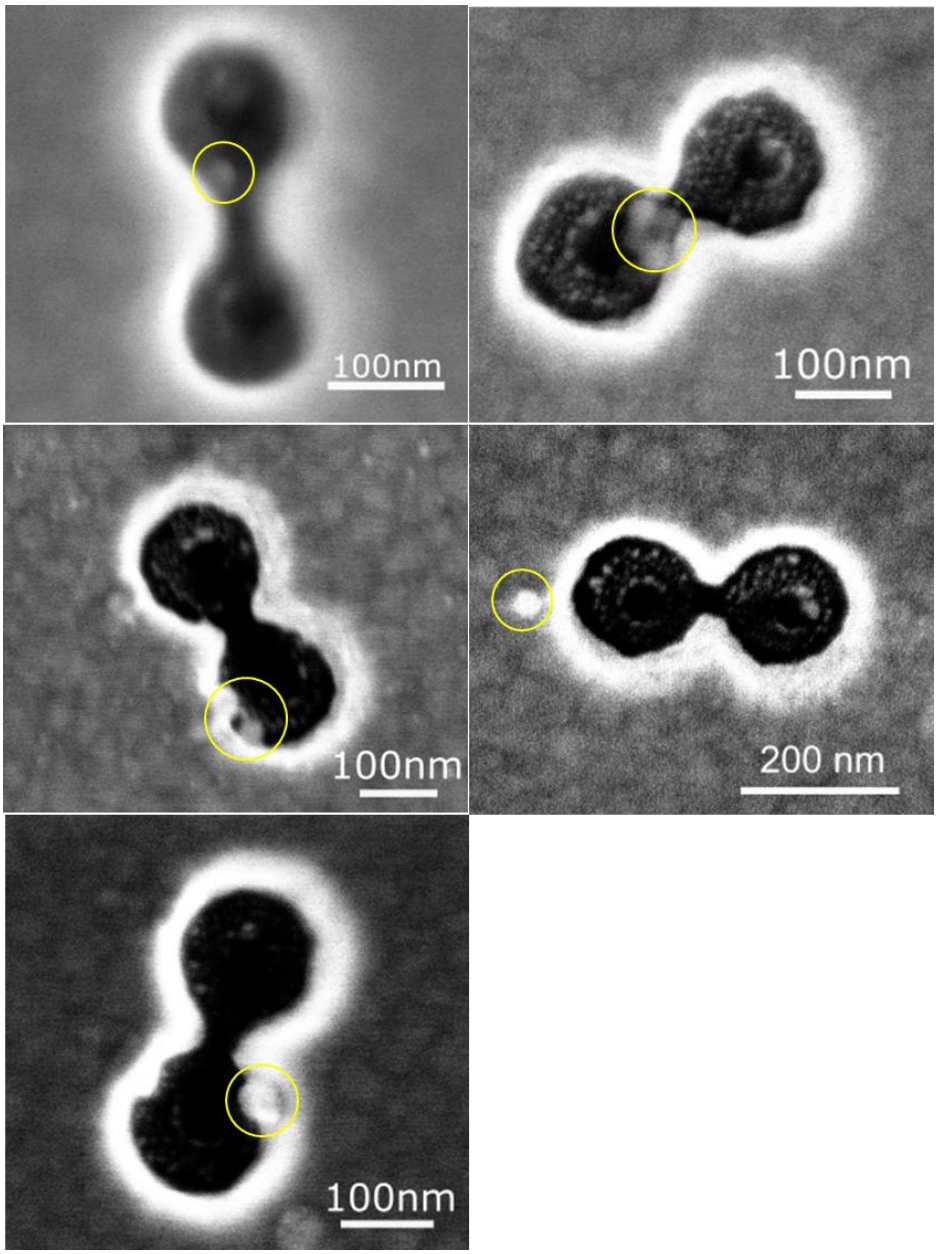

Figure II.4: Series of EM images showing immobilized nanoparticles after the anchoring procedure.

Trapping events

Trapping events were observed by monitoring the transmission of the laser through the double-nanohole aperture. The transmission was collected with a 10× microscope objective and measured with an avalanche photodiode (Thorlabs APD120A). This signal was recorded at 75 ksps using a DAQ (Advantech USB-4711A). Figure II.5 shows two characteristic instances of trapping.

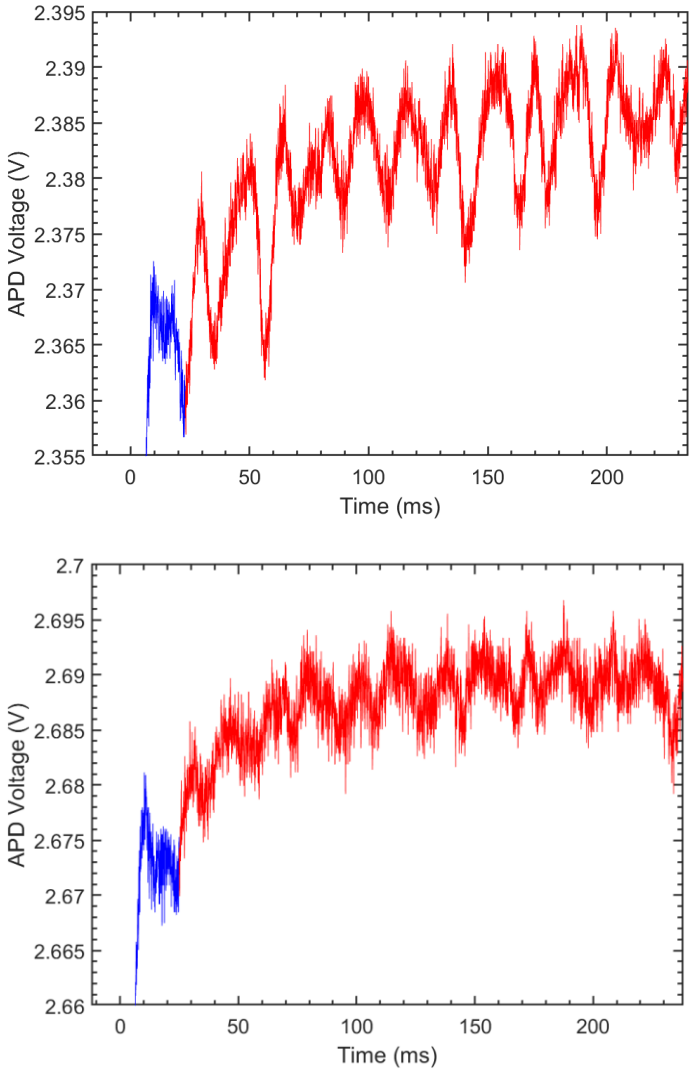

Figure II.5: Typical trapping events of functionalized $NaYF_4$ NPs showing before trapping (blue) and after trapping (red). The laser is turned on at 0 s.

References

1. Alizadehkhaledi, A.; Frencken, A. L.; van Veggel, F. C. J. M.; Gordon, R., Isolating Nanocrystals with an Individual Erbium Emitter: A Route to a Stable Single-Photon Source at 1550 nm Wavelength. *Nano Lett.* **2020,** *20,* 1018-1022.

2. Sharifi, Z.; Dobinson, M.; Hajisalem, G.; Shariatdoust, M. S.; Frencken, A. L.; van Veggel, F. C. J. M.; Gordon, R., Isolating and Enhancing Single-Photon Emitters for 1550 nm Quantum Light Sources Using Double Nanohole Optical Tweezers. *J. Chem. Phys.* **2021,** *154*, 184204.

3. Frencken, A. L.; Blackburn, A. M.; van Veggel, F. C. J. M., The Internal Structure of Lanthanide-Doped Nanoparticles and the Effect of High-Temperature Annealing on Their Luminescent Properties. *J. Phys. Chem. C* **2022,** *126*, 16341–16348.

4. Dong, C.; Pichaandi, J.; Regier, T.; van Veggel, F. C. J. M., Nonstatistical Dopant Distribution of Ln^{3+}-Doped $NaGdF_4$ Nanoparticles. *J. Phys. Chem. C* **2011,** *115*, 15950-15958.

Appendix III: Supplementary information to chapter 7

Linear model using alternative $1/T_1(0)$ and $1/T_2(0)$

A comparison between experimental and calculated $1/T_1$ and $1/T_2$ values of mixtures was done, except instead of using $1/T_1$ and $1/T_2$ of water, an average of the $1/T_1(0)$ calculated from the y-intercepts of the pure CA $1/T_1$ plots was used for $1/T_1(0)$. An average of the $1/T_2(0)$ from averaging the y-intercepts of the pure CA $1/T_2$ plots was used for $1/T_2(0)$. The results are compared in Figures III.1 and III.2. The percent difference is shown in Figures III.3 and III.4.

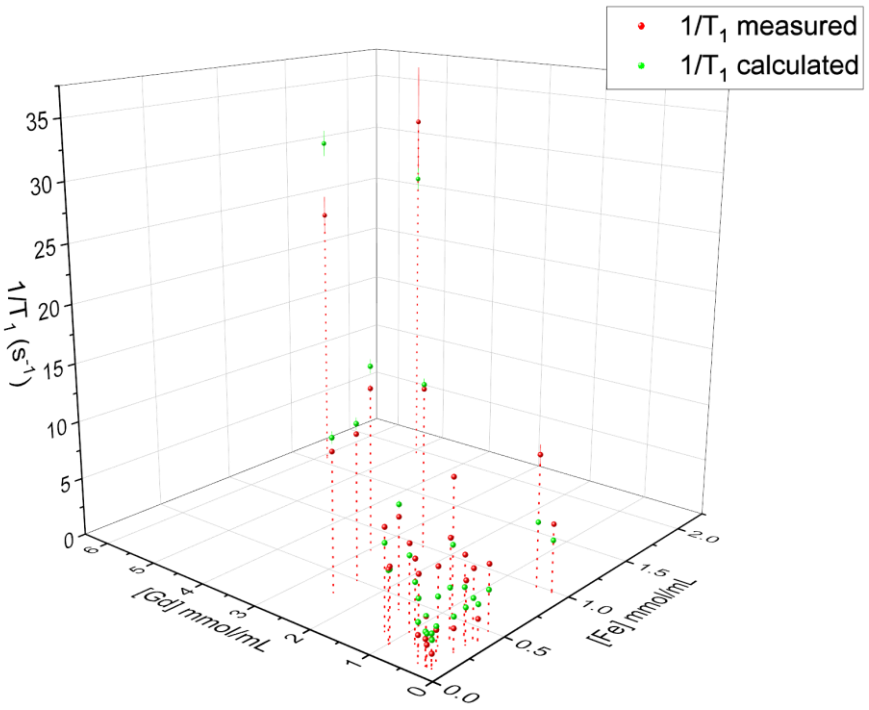

Figure III.1: 3D plot of the measured $1/T_1$ at various concentrations of Feridex and Magnevist mixtures. A comparison is made with $1/T_1$ values that were calculated using equation (3) (from chapter 7) and the $1/T_1(0)$ from the average of the y-intercepts of the pure CA dilution series (green).

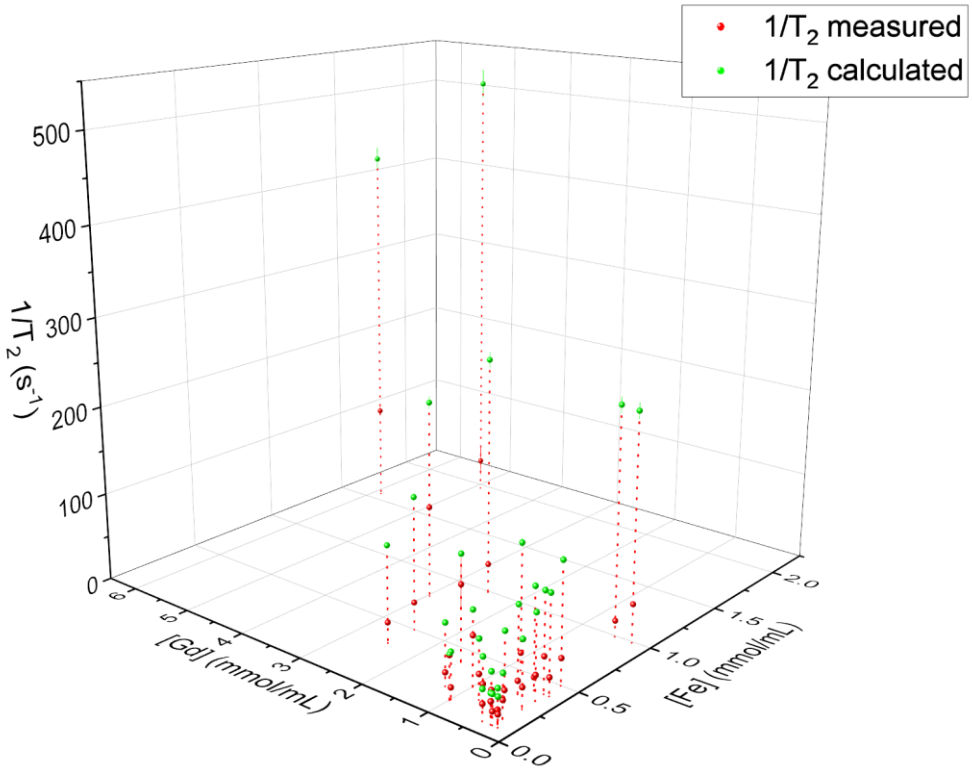

Figure III.2: 3D plot of the measured $1/T_2$ at various concentrations of Feridex and Magnevist mixtures (red). A comparison is made with $1/T_2$ values that were calculated using equation (3) (from chapter 7) and the $1/T_2(0)$ from the average of the y-intercepts of the pure CA dilution series (green).

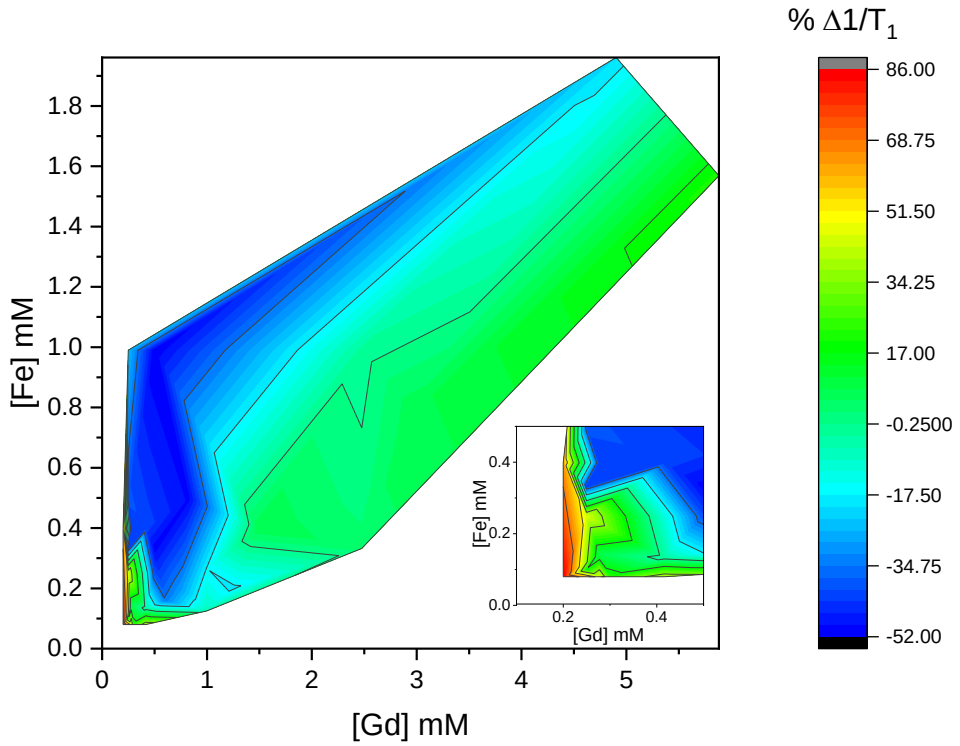

Figure III.3: Color map plot of the difference between the calculated $1/T_1$ from linear addition of r_1 values determined from pure mixtures and the measured $1/T_1$ at the same concentration. The percent difference of the calculated values with respect to measured values is shown. The insert is a zoom-in of the region at low concentrations.

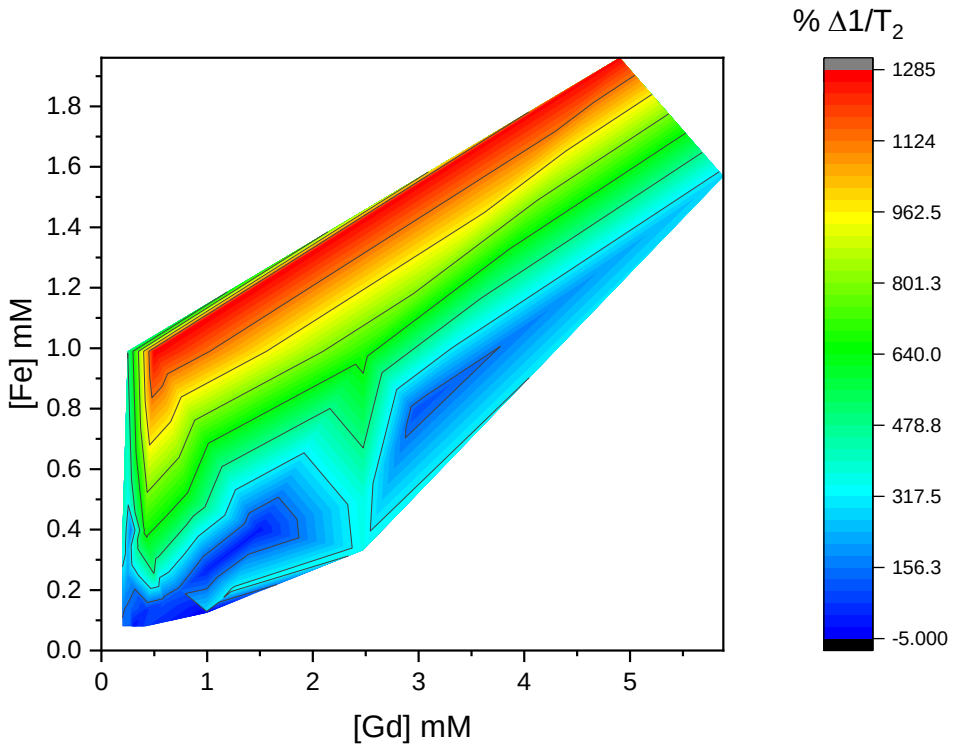

Figure III.4: Color map plot of the difference between the calculated $1/T_2$ from linear addition of r_2 values determined from pure mixtures and the measured $1/T_2$ at the same concentration. The percent difference of the calculated values with respect to the measured values is shown.

Magnetic moment calculation

Using a simple magnetic dipole model, the magnetic field effect of a magnetic nanoparticle on a nearby particle can be calculated. The magnetic field generated by a magnetic dipole is given by equations (1) and (2). Assuming orientation of a magnetic dipole along the x-axis, the magnetic field strength it generates can be calculated in the x-direction (B_x) and the y-direction (B_y), at a given distance r.[1] The model can potentially be extended into three dimensions if we assume that the effect into any direction perpendicular to the x-axis is equivalent. Here, B_x is the magnetic field in the x-direction and B_y the field in the y-direction, at any point with distance r from magnetic dipole m. μ_0 Is the permeability of vacuum, and θ is the angle of the line through the point and the dipole center with respect to the x-axis.

$$B_x(r) = \frac{\mu_0}{4\pi} m\left(\frac{3cos^2\theta - 1}{r^3}\right) \quad (1)$$

$$B_y(r) = \frac{\mu_0}{4\pi} m\left(\frac{3\cos\theta\sin\theta}{r^3}\right) \quad (2)$$

For this calculation, we assume a Feridex NP to consist mostly of γ-Fe_2O_3, with the magnetic moment of a Feridex NP of 11,500 μ_B and diameter of 8 nm, as determined by Johnson *et al.* at applied fields between 3.8 T and 20 T.[2] The average distance between two NPs in a commercially available Feridex dispersion (0.2 M), is calculated to be around 40 nm, and the average distance between two NPs in the most concentrated mixture (1.9 mM [Fe]) in Figure 6 to be around 200 nm, and in the least concentrated mixture (0.1 mM [Fe]) around 550 nm. For any two particles that are in plane with each other (θ = 90 °), the magnetic field in the direction of the applied field experienced from its neighbor at the average distance is -6.42 * 10^{-8} T in the most dilute sample at 0.1 mM [Fe]. For the average distance at 1.9 mM [Fe], the field strength effect increases by 19 times, to -1.22 * 10^{-6} T.

For 0.2 M [Fe], the calculated field strength is $-1.28 * 10^{-4}$. If particles are oriented along the same axis in the direction of the applied field ($\theta = 0°$), the magnetic field in the direction of the applied field they experience from a nearby NP is positive, resulting in $1.28 * 10^{-7}$ T at 0.1 mM [Fe], $2.44 * 10^{-6}$ at 1.9 mM [Fe], and $2.57 * 10^{-4}$ T at 0.2 mM [Fe]. The negative field strength a NP exerts on a neighboring NP with parallel magnetic moment in the same plane, and the positive field strength a NP exerts on a neighboring NP along the dipole axis, both seem to linearly scale with the concentration. While these magnetic field strengths are small compared to the externally applied magnetic field (9.4 T), they may still affect the organization of the NPs in the direction of the applied field. These results support the hypothesis that at increased concentrations particles may repel each other perpendicular to the applied field and attract along the direction of the applied field. This may lead to aggregation of the NPs in chains along the direction of the applied field and thus reduce the effective relaxivities.

References

1. Schill, R. A., General Relation for the Vector Magnetic Field of a Circular Current Loop: A Closer Look. *IEEE Trans. Magn.* **2003,** *39*, 961-967.

2. Hah, H.; Williams, A.; Pham, W.; Johnson, C.; Johnson, J., Magnetic Properties of the MRI Enhancement Agent Feridex from Mössbauer Spectra. *Hyperfine Interact.* **2021,** *242*, 1-5.